In vivo ultrasonic tissue characterization of liver metastases

In vivo ultrasonic tissue characterization of liver metastases

een wetenschappelijke proeve op het gebied van de Medische Wetenschappen

Proefschrift ter verkrijging van de graad van doctor aan de Katholieke Universiteit Nijmegen, volgens besluit van het College van Decanen in het openbaar te verdedigen op 19 februari 1998 om 15.30 uur precies door

Hendrikus Johannes Huisman

geboren op 10 augustus 1966 te Rotterdam.

Promotor	Prof.dr. A. van Oosterom
Co-promotor	Dr.ir. J.M. Thijssen
Manuscriptcommissie	Prof.dr. D.J.Th. Wagener Prof.dr. G.J.E. Rosenbusch dr. Th.E. Schouten

ISBN	90 9011320 7
Cover design	Rick van Koert, Rotterdam
Type setting	LaTeX2e
Reproduction	DTQP, Schiedam

To my father

Contents

Chapter 1

Introduction

Ultrasonic imaging is a commonly used, powerful diagnostic technique in medicine. The images allow a physician to visualize anatomical details **in** the human body with the intention to assess the state of the anatomy. Since the introduction of the concept of gray-scale ultrasonic imaging in the early 70's, the number of applications has increased and the image quality is still being improved. More recently, UTC strategies are being developed to quantify information in the available image on the ultrasound machine or to visualize new information in additional images. The quantification of existing visual information may help physicians to enhance the robustness and reproducibility of their assessments. This thesis describes improved and/or new UTC strategies.

This research was motivated by developments in related research areas. Continuing fundamental research in medical ultrasound has led to an increase in the understanding of the physical mechanisms that govern the image formation process. The resulting theoretical insights may enhance the amount of information that can be retrieved from ultrasonic images. Recent techniques in signal processing, image processing and pattern recognition facilitate the extraction and quantification of this information. More specific, artificial neural networks have shown promising results in related problems. Finally, actual application of these techniques seems realistic as contemporary computer speed- and memory has reached a sufficient level.

This chapter starts with a demarcation of the ultrasonic tissue characterization (UTC) field of research. The subsequent section then briefly summarizes previous research on UTC. Finally, the problem definitions for the subsequent chapters in this thesis are formulated.

1.1 Ultrasonic tissue characterization

An accurate diagnosis is an important step to help a physician to define a correct treatment of a patient. Contemporary medical ultrasonic scanners are well-known, non-invasive, diagnostic tools to image various features in the human body in real-time (Wells, 1977; McDicken, 1991). One of the most important applications is the imaging of soft-tissue structures, and the abdomen is a particular area of application. The central column in Fig. 1.1 shows the elements of the common ultrasonic diagnostic chain. An ultrasound imaging system produces a B-mode image

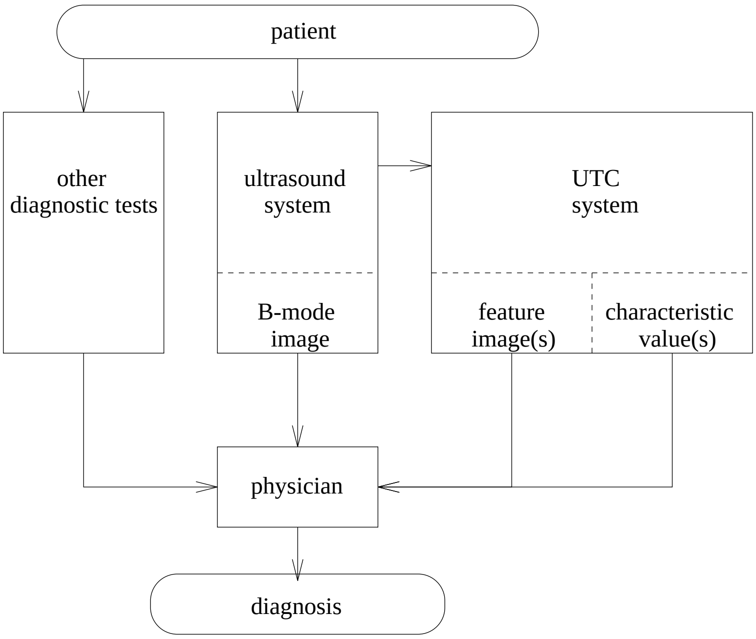

Figure 1.1 Ultrasound is one of the diagnostic tools. Ultrasonic tissue characterization is an extension to customary, ultrasonic B-mode imaging aimed at better supporting the physician.

of a section of the human body. The image is interpreted by a physician who then tries to add information to the diagnosis.

The UTC methods in this thesis are a means of quantifying, or visualizing information regarding the investigated tissue, not readily available from the ultrasonic image to the human observer. The right side of Fig. 1.1 shows two types of information that can be produced by the UTC methods: a new feature image, or a characteristic value of the investigated tissue. For example, if the UTC method is designed to produce an image with improved lesion contrast, then it helps the physician to detect lesions. On the other hand, a characteristic value that is correlated to relevant tissue histology may give support to characterize the tissue pathology or to follow-up the effect of treatment.

Fig. 1.2 shows three applications of the UTC system. Each of these applications is designated with a specific term that will be used throughout this thesis. In both ‘focal’ and ‘diffuse’ analysis the UTC system produces characteristic values. 1) In focal analysis the features are extracted from a restricted region of interest within the image. An example of this is when the tissue inside the region represents a previously detected lesion. The feature(s) calculated from this region can then be used to differentiate or follow-up that lesion. 2) In diffuse analysis the whole organ is imaged in a set of acquisitions. Within each image the parenchyma is segmented and one or more average characteristic values are extracted. Recent *in vivo* examples are the analysis of: diffuse liver diseases (Kuc, 1980; Garra et al., 1987; Parker et al., 1988a; Hartman et al., 1993); and

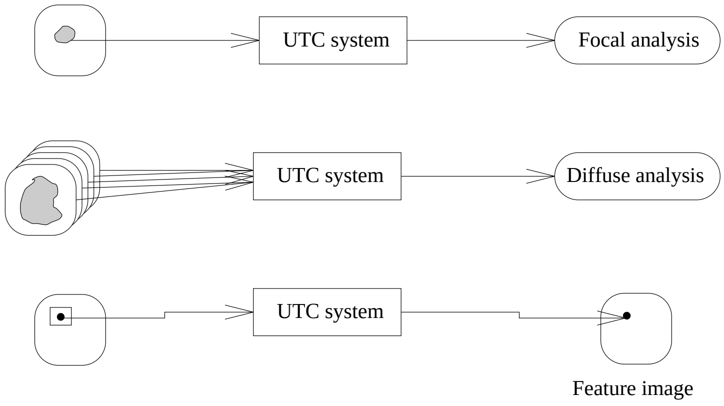

Figure 1.2 Three application areas of an UTC system.

tumors in the eye (Coleman et al., 1985; Thijssen et al., 1991). 3) In feature imaging a feature is estimated in a small window at different locations in the original image, where the window is scanned by the software over the whole image. By imaging the feature value at the central location of the scanning window a new image results. Each UTC feature can produce its own image, but images may also be combined into one color image, and/or shown in color overlay at the original image produced by the ultrasound scanner (Feleppa et al., 1986; Insana and Hall, 1990; Romijn et al., 1991; Momenan et al., 1994; Valckx et al., 1997).

1.2 Previous work

This section briefly reviews research in UTC as defined in the previous section. The intention is to highlight some of the possibilities and limitations of UTC, such that it may serve as a basis for the subsequent problem definition section.

The structure of this section follows the signal generation and processing path as shown in Fig. 1.3. It starts with the tissue model that describes the (measurable) effects of the tissue on the received ultrasonic signal. The ultrasonic scanner transmits ultrasound into and receives ultrasound from the tissue, but also affects the signal as it 'passes through' the scanner step. A scanner model allows to quantify these effects on the signal. At this point the signal can be thought of as being available from common ultrasonic scanners. The scheme continues with the elements within an UTC system. The acquisition system digitizes the signals. The calibration step tries to remove the effects due to the scanner from the signal before it is passed on to the feature extractor. Obviously, good calibration requires a good scanner model. Several features can be extracted from the calibrated signal and these feature values are combined and/or transformed in the analysis step to result in the required output. The diagram ends here, however, a subsection on artificial neural networks is also included, because some of the research described in this thesis concerned the application of neural networks to the feature extraction and analysis stages, as is also shown in Fig. 1.3.

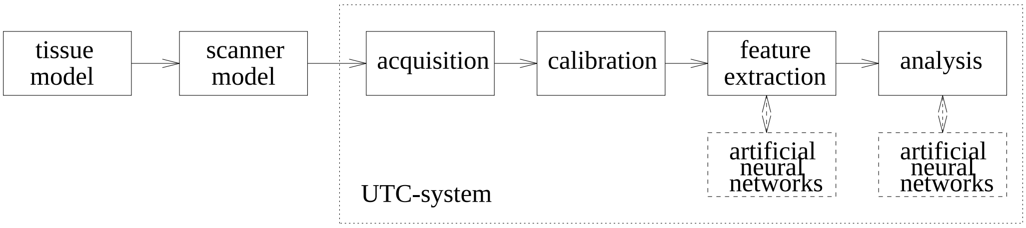

Figure 1.3 A schematic diagram that decomposes the signal generation and processing path from tissue to analysis into different blocks. The blocks within the area delineated by a dotted line are part of an UTC system.

1.2.1 Ultrasonic tissue model

An ultrasonic tissue model relates the tissue- to the signal properties. In conventional pulse-echo ultrasonic imaging a short acoustic pulse is emitted into the tissue. Subsequently, the resulting echoes are received by a transducer that converts them into an electrical signal. This signal is partly the result of interactions of ultrasound with the tissue and, in general, two types of echo generating structures in the tissue can be distinguished. Strong reflections are mostly due to highly reflective organ boundaries (see the liver contour in Fig. 1.4), and as such they can be used to study, for example, organ deformation. The echoes from within the organ are usually less intense and are the result of backscattering from small-scale structures, or scatterers (e.g. parenchyma cells, small vasculature). This thesis will focus on the analysis of these soft echoes (or presumably the parenchyma tissue) from scatterers, while the strong reflections are excluded.

Three components of the ultrasonic parenchymal tissue model are considered. The first component is *the amount of energy that is reflected by the tissue,* or backscatter. The backscatter intensity is proportional to the individual reflectivity of a scatterer and to the number of scatterers in a unit volume (Oosterveld et al., 1985). The B-mode image on the monitor of the ultrasonic scanner mainly visualizes the average reflectivity of the tissue (Fig. 1.4). The backscatter also has an intricate, frequency-dependent relation with the size and shape of the scatterer (Lizzi et al., 1987; Romijn et al., 1989; Insana et al., 1990). Estimates of the backscatter at different frequencies would enable to characterize the tissue even further. However, accurate scatterer characteristics (e.g. number density, size) may be difficult to estimate, as it is likely that multiple types of scatterers are present within the tissue, e.g. individual liver cells and vascular structures at lobular level (Bamber, 1979; Nicholas et al., 1982), or Bowman's capsule and glomerular arterioles in the kidney (Insana et al., 1992).

The second effect of the tissue is *the decay of the ultrasonic pulse intensity* when the pulse travels through the tissue. In the frequency range commonly used for abdominal work (1–6MHz), absorption is the dominant feature of attenuation in the liver (Pauly and Schwan, 1971; Parker, 1983). The absorption is due to macro-molecular relaxation processes, which result in a frequency dependent attenuation coefficient (Jongen et al., 1986; Parker et al., 1988b; Berkhoff et al., 1996). The attenuation coefficient can be approximated with a linear model (Pauly and Schwan, 1971) in a limited (but realistic) frequency range. A power model may be used, however, the precision of the power law fit in a small frequency range is low (Jongen et al., 1986). The

Figure 1.4 Example B-mode image of a section in the liver.

combined estimation of attenuation and backscatter is also referred to as acousto-spectroscopy.
The third component of the ultrasonic tissue model is *the spatial correlation* within the tissue, which can be present at different levels. At the visible level it describes the inhomogeneous nature of some disease processes. For example, the ultrasonic appearance of the parenchyma area of a cirrhotic liver is often coarser than normal (Rettenmaier, 1990).

1.2.2 Ultrasonic scanner model

The backscattered pressure waves are received by a transducer which produces a so-called radio-frequency (rf) signal which is the basis for further processing in the scanner. The rf signal is the result of a characteristic interaction with the tissue, but will also show characteristics of the ultrasonic system. The latter characteristics are unwanted as they will decrease the precision and accuracy of the UTC features.
One of the main problems in ultrasonic images, which is also clearly visible (Fig. 1.4), is the noisy character of the available signal as a result of the phase-sensitivity of common, piezo-electric transducers. The transducer output signal is the result of a phase-sensitive summation at

the transducer surface of backscattered echoes from many scatterers. The summation results in an amplitude that will be different for every realization of a scatterer distribution, even though the bulk tissue characteristics are the same (Burckhardt, 1978). The probability density function (pdf) of the received amplitudes (e.g. the envelope of the rf signal) is commonly assumed to be a Rayleigh function which has an amplitude signal-to-noise ratio of approximately 2. Due to this, a single sample UTC feature has very low discriminative power, and a larger estimation window is required to get a more accurate estimate. The Rayleigh condition is true only in case of a large number of scatterers. If this is not true, then the pdf shape will depend on the number of scatterers and is generally described by a k-distribution (Jakeman, 1984). Estimating this dependency may reveal additional information about the tissue, and as such it has been topic of many research papers.

The dependence of ultrasonic signals on the frequency-dependent beam diffraction pattern of the ultrasonic transducer has been recognized quite early (Kossoff, 1979). This diffraction effect results in a dependence of the estimated feature with the depth of the estimation window (Cloostermans and Thijssen, 1983; Fink and Cardoso, 1983; O'Donnell, 1983; Robinson et al., 1984). If uncorrected, a feature estimated at two depths in the same tissue will generally result in two different estimates. This would not be a problem if the scanner and the transducer were always the same and the investigated tissue volume was always positioned at the same depth. In practice, to compare features within the same image, between patients, or between different scanners, a calibration is required. This calibration should also entail a second frequency-dependence of the received spectrum on the scanner characteristic due to the process of converting acoustical energy into an electrical signal, and vice versa, by the transducer.

The final scanner related characteristic considered here is speckle. Speckle manifests itself as correlation between pixels in the ultrasonic image (see also Fig. 1.4), where the intended correlation is due to overlapping sampling volumes and not due to the tissue. To explain speckle formation, consider a transmitted ultrasound pulse that travels through the medium. At any moment the pulse insonifies a volume of scatterers. A pixel value is determined by the reception of the backscatter from the scatterers in this volume. Nearby pixels generally have overlapping sample volumes, and as a result the pixel values are correlated. In the focal zone and farfield of a transducer, the speckle size expressed in millimeters is almost identical to the lateral and axial size of the sample volume (beam width and pulse length) (Wagner et al., 1983; Thijssen et al., 1991). In the near field this is not the case, because there the phase changes due to sample volume translations are much larger and intricate, which tends to decorrelate the pixel values. Therefore, small speckles are produced near to the transducer. Speckle reduces the spatial resolution and reduces the precision of the UTC features because it is the number of speckles rather than the number of pixels in the feature estimation window that determines the amount of noise reduction (Verhoeven and Thijssen, 1993).

1.2.3 Acquisition and preprocessing

The UTC methods discussed in this thesis operate on unprocessed rf signals, preferably after only linear amplification of the electrical signal from the transducer. The idea is to avoid any information loss due to signal processing steps within the scanner. These rf signals are high-frequency signals (2–4MHz) and show a decreasing amplitude with depth due to attenuation.

Figure 1.5 The echographic workstation (used to acquire and store the signals from the ultrasonic scanner).

Digitizers capable of operating at sufficiently high sampling frequencies were only available with 8 bits precision during conception of the system used in this thesis. Without further hardware, the rf signals can only be acquired in a limited depth-range, because due to the attenuation, the level of the signals originating from deeper parts in the body, becomes too low to adequately digitize.

A special workstation has been developed for UTC by Verhoeven and co-workers (Verhoeven, 1994, ch. 3) and is shown in Fig. 1.5. The workstation can digitize rf signals at a maximum sampling frequency of 40MHz. A special component is the so called time-gain-compensator (TGC) (Verhoeven and Thijssen, 1992). The TGC amplifies the rf signals before digitization with a software adjustable gain at each depth. A proper TGC curve results in a signal (rf') that can be digitized with an adequate number of digitization levels throughout the whole depth-range. The digitized rf' signals were stored in files on optical disk for later use. Also stored in each file was the TGC curve, which enabled reproduction of the original rf signal. An operational version of the acquisition software has been developed by the author and distributed to partners in an EC-project (Claque, 1994) and includes a database to retrieve patient related information and acquisitions on a multiple disk set. Furthermore, software has been developed for fast, linear interpolation scan-conversion of the polar format rf acquisitions to the rectangular format video image (Berkhoff et al., 1994).

1.2.4 Calibration

As discussed in the subsection on the scanner model, the signal available from the transducer is corrupted by transducer dependencies. A wide range of methods have been proposed that estimate the frequency-dependent beam diffraction effect by assessing the characteristics of the received signals (e.g. average amplitude, or power spectrum) at varying depths from the reflections of: phantoms (Cloostermans and Thijssen, 1983; Fink and Cardoso, 1983), plane reflectors (Lizzi et al., 1983; Madsen et al., 1984; O'Donnell, 1983). However, the signals corrected using the previous procedures still show a remaining depth-dependence (Robinson et al., 1984). Only theoretical, or very elaborate methods have been proposed to deal with this aspect (Laugier et al., 1987; Céspedes and Ophir, 1990).

Diffraction correction is indispensable for depth-independent attenuation, as well as backscatter coefficient estimates. After a proper correction, the attenuation can be estimates on an absolute scale and be compared between patients even on different scanners. To estimate the absolute backscatter coefficient, additional corrections are necessary. Firstly, the received signal spectrum is partly determined by the acousto-electrical transfer function of the transducer. Secondly, the backscatter is estimated from the spectrum in a small time window. The length of this time window and the shape of the transducer beam determine the volume of scatterers, and thus the backscatter is proportional to this volume. Analytical expressions for this volume have been derived for single element transducers (Bamber and Hill, 1981; Ueda and Ozawa, 1985) and array transducers (Insana et al., 1994) under strict conditions (e.g. in the focal zone, weak scattering). This type of 'direct' absolute backscatter measurement is well suited for *in vitro* conditions (van der Steen, 1990). Another, 'indirect' approach is to compare the received spectra from the tissue and a tissue-mimicking (TM) phantom with the same transducer (Yao et al., 1991). Thus the indirect backscatter is relative to the phantom material. The properties of the TM phantom can be estimated *in vitro* using the 'direct' method. These known properties can then be used to convert the indirect backscatter estimate into an absolute estimate. The 'indirect' method is capable of operating under *in vivo* conditions.

1.2.5 Feature extraction

The extraction of the features is discussed separately from the calibration. In many papers on UTC feature extraction methods, the calibration is an integral part of the design. For example, some of the features that will be discussed use local estimates of the frequency spectra in the ultrasonic signal. Consequently, such method will require a frequency-dependent calibration. Furthermore, a fast implementation results if the calibration and feature extraction methods can be combined. However, a separate discussion allows to introduce aspects general to all features extraction methods and enables the incorporation of knowledge from pattern recognition theory.

A main property of all UTC features is that they require the use of adequately sized windows to reduce the effect of the (Rayleigh) noise. This implies that the tissue within the analysis window should be of a single homogeneous tissue type. The expected size of, for example, metastases to be analyzed will impose a maximum limit to the window size and thus a minimum to the achievable precision. The relation between the precision of a feature and window size due to Rayleigh noise has been analyzed for some UTC features, e.g. attenuation (Kuc and Taylor, 1982; Berger et al., 1987; Parker, 1986), backscatter, (Romijn et al., 1989; Yao et al., 1991), and signal-to-noise ratio (Verhoeven and Thijssen, 1991; Dutt and Greenleaf, 1995).

Some of the main UTC features considered in this thesis are the acousto-spectrographic features: attenuation and backscatter. Historically, the attenuation was one of the first parameters of the tissue model to be estimated from backscattered signals (Kuc, 1976; Lizzi et al., 1976), because it is a relative measure and is not affected by intervening tissue layers. The frequency-dependent attenuation coefficient can be measured from the spectral decay of the received spectra at each depth (so called spectrogram) (Cloostermans and Thijssen, 1983). This spectrogram can be measured using the Short-Time-Fourier-Transform (Oppenheim and Schafer, 1975). After correction for the attenuation in the tissue, the average spectrum in the spectrogram is an estimate of the backscatter coefficient. The frequency dependent attenuation- and backscatter coefficients are often further approximated by a two-parameter linear model.

The amount of UTC features in ultrasonic literature can be huge (Raeth et al., 1985; Nicholas et al., 1986). If the tissue model allows the probability density function of the received echo amplitudes to change due to variations in scatterer density, e.g. (Jakeman, 1984), then various histogram features need to be estimated, such as: mean value (which is correlated to the average backscatter), variance, mean over standard deviation (SNR), skewness, and kurtosis. The tissue model might also predict spatial correlation lengths to be characteristic of the tissue (Jacobs and Thijssen, 1991). This can occur at a low (sub-)resolution level and the features of interest then are various types of features estimated from the auto-covariance matrix. General correlation features are obtained from the cooccurrence matrix such as: angular second moment, correlation, and entropy (Haralick et al., 1973; Conners and Harlow, 1980; Valckx and Thijssen, 1997). Actually, a full overview of features ever used in UTC would require a summary of a large set of features used in image processing, which is outside the scope of this thesis, but indicates that the amount of features can be large.

Selecting features from the large, initial feature set may be necessary because too many features can harm the performance of the subsequent analysis stage (McLachlan, 1992), as will be discussed in the next subsection. There is reason to discard some features, as it is very likely that quite a number of general image processing features contain no tissue discriminatory information. Furthermore, different features may partly contain the same discriminatory information, and an indication might be that they are highly correlated (Oosterveld et al., 1993; Thijssen et al., 1993). Thus, the effective number of features might already be quite low. If the aim is to have an optimal performance of the subsequent analysis stage, then all possible feature subsets should be tested, or a sub-optimal search strategy can be applied if the number of features is high (Kittler, 1986). However, given a finite data set, the estimated performance can be positively biased by an automated selection procedure (McLachlan, 1992), and the situation is exacerbated if the number of features is very large relative to the amount of training data. If prior knowledge is available, it should be used to select a reasonably sized set of features with known discriminatory capabilities in the application domain.

1.2.6 Analysis

The analysis succeeds the feature extraction (see Fig. 1.3) and completes the UTC system. The aim of this final step is to produce an analysis of the tissue region under investigation based on the observed feature values. In case of diffuse or focal disease, the result of the analysis should be a judgment of the pathology. This judgment can be either a discrete classification or a continuous value that expresses the deviation from the reference (e.g. normal parenchyma tissue). In case of feature imaging, the result of the analysis should be one, or a few images that, in addition to the available B-mode image at the scanner, help to improve detection of pathology. In all three cases the analysis should compress the relevant information from the previously extracted features in a few discriminating features.

In general an analysis method comprises several discriminant functions, one each tissue class. A discriminant function estimates the probability that the observed features belong to that class. The output of the discriminant functions directly results in discriminant features, or the input features can be classified by allocating the discriminant function with maximum output. At this stage it is possible to evaluate the performance of the UTC system by using a test set of data with known classification. If the discriminant function is a good estimator, then in case of (too) low performance the extracted features did not contain enough information and the existing features have to be improved and/or new features have to be found.

The previous setup of the analysis method simply assumed that the discriminating functions generate the true estimate of the probability that the observed features belong to a certain class. In practice, these functions have to be estimated using training data. The relative number of occurrences of a feature value in training is an estimate of its probability. A problem occurs if the size of the training set is small, because in that case, the number of occurrences can be low or even zero, which will affect the estimate of the probability. In general this problem is solved by assuming an *a priori* model of the discriminating function. For example, a Gaussian model can be used if the features have a Gaussian distribution. The choice of model is important, because a simple model may not fit the training data very well, and a complex model may overfit the data. Many models and their accompanying estimators have been used in UTC, such as: discriminant analysis, non-parametric discriminant methods, decision trees, k-nearest neighbor (k-NN), and, although not always recognized as such, artificial neural networks (ANN).

A conflict arises because the carefully collected, but limited data set has to be used both for estimating the performance of the UTC method, as well as the estimation of the discriminating function. The performance should be estimated from an unseen part of the same dataset, because otherwise the estimated performance will be positively biased (Foley, 1972; Fukunaga, 1989). This well-known phenomenon in pattern recognition literature is not always acknowledged in ultrasonic literature. As an illustration, Edmonds et al. (1991) stated: ”The CART [a decision tree] approach appears to be more robust in its classification [than conventional discriminant analysis]; however, results break down when it attempts to classify previously unseen cases”. Many methods are available to deal with this phenomenon (Raudys and Jain, 1991).

1.2.7 Artificial neural networks

A topic of interest for this thesis was the use of artificial neural networks (ANN) in UTC. ANNs have been applied to various signal processing and pattern recognition problems since the perceptron was established by Rosenblatt (Hertz et al., 1991). The perceptron, however, was limited to linearly separable datasets (Bishop, 1995). A resurgence of ANNs occurred by the discovery of backpropagation learning of multilayer perceptrons by Rummelhart et al. (Hertz et al., 1991).

This development has enabled neural networks to learn complex relations as well. As a result a number of references appeared in literature in which ANNs were applied to UTC (Silverman and Noetzel, 1990; klein Gebbink et al., 1993).

1.3 Problem definition

The main subject of this thesis is the development of UTC methods in their application to the diagnosis of metastases in the liver. The motivation has been the success of UTC in analyzing diffuse liver diseases. The problem is that metastases are relatively small, therefore the UTC window size has to be small, and consequently the precision of the estimated features will be low. Furthermore, to be applicable in a clinical setting, the UTC methods obviously have to operate under *in vivo* conditions. Therefore, the general objective is to find accurate, precise and discriminative feature estimation methods that can operate under *in vivo* conditions.

A first problem encountered was the calibration, and more specific, the beam diffraction correction. When adapting methods to operate in small windows it was possible to estimate the UTC features at various depths in the image. Implementation of a well-known calibration method using a foam phantom still resulted in the estimated UTC features being dependent on the depth. If this was not solved, then comparing the metastases from different depths would result in an extra noise component due to incorrect calibration. As the features are already not precise due to the small acquisition window it was considered important to find better calibration methods. Part of chapter 2 is devoted to a new method for accurately calibrating *in vivo* images.

Throughout this thesis good segmentation of the parenchyma-only region is emphasized, because the estimated features in the normal parenchyma constitute a reference database. The reference can be contaminated by non-parenchyma estimates such as blood-vessels. In that case the reference range can become wider than necessary, which would affect the discriminability.

The main noise component (Rayleigh noise) of ultrasonic signals is due to the phase-sensitive reception of scattered pressure waves at the transducer surface. This noise component determines to a large extent the precision of some of the features. To know whether or not an estimated feature value is within the normal range of observations, or is significantly different, is of direct interest to the analysis of the features. A significant deviation can be indicative of the presence of an abnormality in the tissue. In normal tissue, the variations may be due to histological variations within or between organs. A deviation may also be due to an incorrectly functioning diffraction correction algorithm, or it may even indicate other noise components. Thus, it is important to have operational knowledge about the expected precision of a feature vis-à-vis the window size used to estimate this feature. This was already investigated in other literature for some of the UTC features, but not for all features, and the level of approximation varied. Chapter 2 gives an accurate derivation of the standard deviation of the acousto-spectrographic UTC features used in this thesis and gives estimates of the inter- and intra-organ variations in liver.

To assess the discriminative power of five UTC features, they have been estimated in a large number of liver metastases. A problem was that the simple assumption of a single metastasis model appeared to be unrealistic. An extended metastasis model and the results of the estimated features are presented in chapter 3.

The results from the previous chapter also indicate that the predicted and estimated standard deviations of some of the UTC features still did not agree. Furthermore, another feature showed a significant dependence on the window size. These problems are dealt with in chapter 4 and as a result an extension to the commonly used ultrasonic tissue model is proposed.

As a prerequisite for successful analysis, the number of extracted features should be low, and the features should be discriminative. This can only be achieved when each feature carries distinct information about the metastasis. Most of the UTC features discussed in literature estimate a parameter in the assumed ultrasonic model, or estimate a general feature that has been useful in other image processing areas. Features are selected afterwards on the basis of their estimated discriminative properties. Another method is to use adaptive feature extractors that are are tuned to the problem at hand. In chapter 5 an adaptive feature extraction method is discussed that uses artificial neural networks.

The thesis ends with the general conclusions in Chapter 6 and the summary in Chapter 7.

Bibliography

Bamber JC. Theoretical modelling of the acoustic scattering structure of human liver. Acoust. Lett. 1979;3:114–119.

Bamber JC, Hill CR. Acoustic properties of normal and cancerous human liver – I dependence on pathological condition. Ultrasound Med Biol 1981;7:121–133.

Berger G, Laugier P, Fink M, Perrin J. Optimal precision in ultrasound attenuation estimation and application to the detection of duchenne muscular dystrophy carriers. Ultrason Imag 1987;9:1–17.

Berkhoff AP, Huisman HJ, Thijssen JM, Jacobs EMPG, Homan RJF. Fast scan conversion algorithms for displaying ultrasound sector images. Ultrason Imag 1994;16:87–108.

Berkhoff AP, Thijssen JM, Homan RJF. Simulation of ultrasonic imaging with linear arrays in causal absorptive media. Ultrasound Med Biol 1996;22:245–259.

Bishop CM. Neural networks for pattern recognition. Oxford, UK: Clarendon press, 1995.

Burckhardt CB. Speckle in ultrasound B-mode scans. IEEE Trans Sonics Ultras 1978;25:1–6.

Céspedes I, Ophir J. Diffraction correction methods for pulse-echo acoustic attenuation estimation. Ultrasound Med Biol 1990;16:707–717.

Claque. Clinical assessment of quantitative echography – technical report 1 januari - 30 juni. University Nijmegen, 1994.

Cloostermans MJTM, Thijssen JM. A beam corrected estimation of the frequency dependent attenuation of biological tissues from backscattered ultrasound. Ultrason Imag 1983;5:136–147.

Coleman DJ, Lizzi FL, Silverman RH, et al. Regression of uveal malignant melanomas following cobalt-60 plaque. Retina 1985;5:73–78.

Conners RW, Harlow CA. A theoretical comparison of texture algorithms. IEEE Trans PAMI 1980;2:204–222.

Dutt V, Greenleaf JF. Speckle analysis using signal to noise ratios based on fractional order moments. Ultrason Imag 1995;17:251–268.

Edmonds PD, Mortensen CL, Hill JR, et al. Ultrasound tissue characterization of breast biopsy specimens. Ultrason Imag 1991;13:162–185.

Feleppa EJ, Lizzi FL, Coleman DJ, Yaremko MM. Diagnostic spectrum analysis in opthalmology: a physical perspective. Ultrasound Med Biol 1986;12:623–631.

Fink M, Cardoso JF. Diffraction effects in tissue characterization. In: AIUM Congress. 1983: 180–180.

Foley DH. Considerations of sample and feature size. IEEE Trans Inform Theory 1972;18:618–626.

Fukunaga K. Effect of sample size in classifier design. IEEE Trans PAMI 1989;11:873–885.

Garra BS, Insana MF, Shawker TH, Russell MA. Quantitative estimation of liver attenuation and echogenicity: normal state versus diffuse liver disease. Radiology 1987;162:61–67.

Haralick RM, Shammugan K, Dinstein I. Texture parameters for image classification. IEEE Trans Syst Man Cybern 1973;6:610–621.

Hartman PC, Oosterveld BJ, Thijssen JM, Rosenbusch GJ, van den Berg J. Detection and differentiation of diffuse liver disease by quantitative echography: a retrospective assesment. Inv Radiology 1993;28:1–6.

Hertz JA, Palmer RG, Krogh AS. Introduction to the theory of neural computation. Reading, Massachusetts: Addison-Wesley, 1991.

Insana MF, Hall TJ. Parametric ultrasound imaging from backscatter coefficient measurements: image formation and interpretation. Ultrason Imag 1990;12:245–267.

Insana MF, Hall TJ, Cook LT. Backscatter coefficient estimation using array transducers. IEEE Trans Ultrason Ferroelectr Freq Control 1994;41:714–723.

Insana MF, Wagner RF, Brown DG, Hall TJ. Describing small-scale structure in random media using pulse-echo ultrasound. J Acoust Soc Am 1990;87:179–192.

Insana MF, Wood JG, Hall TJ. Identifying acoustic scattering sources in normal renal parenchyma *in vivo* by varying arterial and ureteral pressures. Ultrasound Med Biol 1992;18:587–599.

Jacobs EMGP, Thijssen JM. A simulation study of echographic imaging of diffuse and structurally scattering media. Ultrason Imag 1991;13:316–333.

Jakeman E. Speckle statistics with a small number of scatterers. Optical Engineering 1984;23:453–461.

Jongen HAH, Thijssen JM, Aarssen M, Verhoef WA. A general model for the absorption of ultrasound by biological tissues and experimental verification. J Acoust Soc Am 1986;79:535–540.

Kittler J. Feature selection and extraction. Chapter 3 in: Young TY and Ku KS, eds. Handbook of pattern recognition and image processing. Orlando, FL, USA: Academic Press, 1986: 59–83.

klein Gebbink MS, Verhoeven JTM, Thijssen JM, Schouten TE. Application of neural networks for the classification of diffuse liver disease. Ultrason Imag 1993;15:205–217.

Kossoff G. Analysis of focusing action of spherically curved transducers. Ultrasound Med Biol 1979;5:359–365.

Kuc R. Parameteric estimation of the acoustic attenuation coefficient slope for soft tissue. In: IEEE Ultras. Symp. Proc.. 1976: 44–47.

Kuc R. Clinical application of an ultrasound attenuation coefficient estimation technique for liver pathology characterization. IEEE Trans Biomed Eng 1980;27:312–319.

Kuc R, Taylor KJW. Variation of acoustic attenuation coefficient slope estimates for *in-vivo* liver. Ultrasound Med Biol 1982;8:403–412.

Laugier P, Berger G, Fink M, Perrin J. Diffraction correction for focussed transducers in attenuation measurements *in-vivo*. Ultrason Imag 1987;9:248–259.

Lizzi FL, Greenebaum M, Feleppa EJ, Elbaum M. Theoretical framework for spectrum analysis in ultrasonic tissue characterization. J Acoust Soc Am 1983;73:1366–1373.

Lizzi FL, Katz L, Coleman DJ. Applications of spectral analysis in medical ultrasonography. Ultrasonics 1976;pp. 77–80.

Lizzi FL, Ostromogilsky M, Feleppa EJ, Rorke MC, Yaremko MM. Relationship of ultrasonic spectral parameters to features of tissue microstructure. IEEE Trans Ultrason Ferroelectr Freq Control 1987;33:319–329.

Madsen EL, Insana MF, Zagzebski JA. Method of data reduction for accurate determination of acoustic backscatter coefficients. J Acoust Soc Am 1984;76:913–923.

McDicken WN. Diagnostic ultrasonics. Edinburgh: Churchill Livingstone, 1991.

McLachlan GJ. Discriminant analysis and statistical pattern recognition. New York: John Wiley & Sons, Inc., 1992.

Momenan R, Wagner RF, Garra BS, Loew H, Insana MF. Image staining and differential diagnosis of ultrasound scans based on the mahalanobis distance. IEEE Trans Med Imag 1994;13:37–47.

Nicholas D, Hill CR, Nassiri DK. Evaluation of backscattering coefficients for excised human tissues: principles and techniques. Ultrasound Med Biol 1982;8:7–15.

Nicholas D, Nassiri D, Garbutt P, Hill CR. Tissue characterization from ultrasound b-scan data. Ultrasound Med Biol 1986;12:135–143.

O'Donnell M. Effects of diffraction on measurements of the frequency-dependent ultrasonic attenuation. IEEE Trans Biomed Eng 1983;30:320–325.

Oosterveld BJ, Thijssen JM, Hartman PC, Rosenbusch GJE. Detection of diffuse liver disease by quantitative echography: dependence on a priori choice of parameters. Ultrasound Med Biol 1993;19:21–25.

Oosterveld BJ, Thijssen JM, Verhoef WA. Texture of B-mode echograms: 3D simulations and experiments of the effect of diffraction and scatterer density. Ultrason Imag 1985;7:142–160.

Oppenheim AV, Schafer RW. Digital signal processing. Englewood Cliffs, NJ, USA: Prentice-Hall, 1975.

Parker KJ. Ultrasonic attenuation and absorption in liver tissue. Ultrasound Med Biol 1983;9:363–369.

Parker KJ. Attenuation measurement uncertainties caused by speckle statistics. J Acoust Soc Am 1986;80:727–734.

Parker KJ, Asztely MS, Lerner RM, Schenk EA, Waag RC. *In vivo* measurements of ultrasound attenuation in normal or diseased liver. Ultrasound Med Biol 1988a;14:127–136.

Parker KJ, Tuthill TA, Baggs RB. The role of glycogen and phosphate in ultrasonic attenuation of liver. J Acoust Soc Am 1988b;83:374–378.

Pauly H, Schwan P. Mechanism of absorption of ultrasound in liver tissues. J Acoust Soc Am 1971;2:692–699.

Raeth U, Schlaps D, Limberg B, et al. Diagnostic accuracy of computerized B-scan texture analysis and conventional ultrasonography in diffuse parenchymal and malignant liver disease. J Clin Ultrasound 1985;13:87–99.

Raudys SJ, Jain AK. Small sample size effects in statistical pattern recognition: recommendations for practitioners. IEEE Trans PAMI 1991;13:252–264.

Rettenmaier G. Fokale leberveränderung. Chapter 3 in: Rettenmaier G and Seitz K, eds. Sonographische differentialdiagnostik. Weinheim, Germany: VCH Publishers, 1990.

Robinson DE, Wilson LS, Bianchi T. Beam pattern (diffraction) correction for ultrasonic attenuation measurements. Ultrason Imag 1984;6:292–303.

Romijn LR, Thijssen JM, Oosterveld BJ, Verbeek AM. Ultrasonic differentiation of intraocular melanomas: parameters and estimation methods. Ultrason Imag 1991;13:27–55.

Romijn RL, Thijssen JM, Beuningen GWJ. Estimation of scatterer size from backscattered ultrasound: a simulation study. IEEE Trans Ultrason Ferroelectr Freq Control 1989;36:593–606.

Silverman RH, Noetzel AS. Image processing and pattern recognition in ultrasonograms by backpropagation. Neural Networks 1990;3:593–603.

Thijssen JM, Oosterveld BJ, Hartman PC, Rosenbusch GJE. Correlation between acoustic and texture parameters from rf and B-mode liver echograms. Ultrasound Med Biol 1993;19:13–20.

Thijssen JM, Verbeek AM, Romijn RL, de Wolff-Rouendaal D, Oosterhuis JA. Echographic differentiation of histological types of intraocular melanoma. Ultrasound Med Biol 1991;17:127–138.

Ueda M, Ozawa Y. Spectral analysis of echoes for backscattering coefficient measurement. J Acoust Soc Am 1985;77:38–47.

Valckx FMJ, Thijssen JM. Characterization of echographic image texture by cooccurrence matrix parameters. Ultrasound Med Biol 1997;23:559–571.

Valckx FMJ, van Geemen AJ, Thijssen JM. Calibrated parametric ultrsound imaging. IEEE Trans Med Imag 1997;Accepted for publication.

van der Steen AFW. Acoustic biomicroscopy: an in vitro tool for development of ultrasonic tissue characterization. PhD thesis, Nijmegen University, 1990.

Verhoeven JTM. Improvement of echographic image quality by data analysis and processing. PhD thesis, Nijmegen University, 1994.

Verhoeven JTM, Thijssen JM. Improvement of lesion detection by echographic image processing: signal-to-noise-ratio imaging. Ultrason Imag 1991;13:238–251.

Verhoeven JTM, Thijssen JM. A software controllable time-gain compensation amplifier board for VMEbus systems. Ultrasonics 1992;40:407–408.

Verhoeven JTM, Thijssen JM. Improvement of lesion detectability by speckle reduction filtering. Ultrason Imag 1993;15:181–204.

Wagner RF, Smith SW, Sandrik JM, Lopez H. Statistics of speckle in ultrasound B-scans. IEEE Trans Sonics Ultras 1983;30:156–163.

Wells PNT. Biomedical ultrasonics. London: Academic Press, 1977.

Yao LX, Zagzebski JA, Madsen EL. Statistical uncertainty in ultrasonic backscatter and attenuation coefficients determined with a reference phantom. Ultrasound Med Biol 1991;17:187–194.

Chapter 2

Precision and accuracy of acousto-spectrographic features

2.1 Introduction

The[1] radio frequency (RF) echo spectrum has been used extensively in medical ultrasound research to interrogate non-invasively the structural properties of biological media. One approach is to use the frequency dependence of the RF backscatter spectrum. Many strategies exist for attenuation and backscatter measurements (Mountford and Wells, 1972; Lizzi et al., 1976; Kuc, 1976; Kuc and Schwartz, 1979; Nicholas et al., 1982; Cloostermans and Thijssen, 1983; Insana et al., 1983; Lizzi et al., 1983; Ueda and Ozawa, 1985). In this chapter attention is focused on the precision (described by the standard deviation, sd), and the accuracy (described by the bias) of four acousto-spectrographic features: the intercept at the central frequency and the slopes of the attenuation and backscatter coefficients.

A detailed understanding of the precision and accuracy of the features is important for three reasons. Firstly, the required precision gives a theoretical minimum of the scanned volume required for differentiation between normal and malignant tissue. Secondly, in theory bias is zero and the sd can be estimated very well, but in practice various factors affect accuracy as well as precision. Insight is gained into the relative importance of each of these factors, which can be used for focusing research on improvement of methods.

Various sources of error complicate the feature extraction process. A trivial source is the effect of the overall gain and the time gain control (TGC) settings on the echographic equipment when using the output video signal. These dependencies were ruled out by acquiring the internal, unprocessed RF signal from within the equipment (custom-built RF interface) using a custom-designed RF acquisition workstation (Verhoeven and Thijssen, 1992). The most important source of error is the speckle noise inherent to the backscattering process found in many biological media. The effect of the speckle noise can be estimated theoretically. The following sources

---

[1] This chapter is based on the publication: Huisman H.J., Thijssen J.M., *Precision and accuracy of acousto-spectrographic parameters* Ultras.Med.Biol. 1996;22:855–871.

of error cannot be estimated theoretically, but it is possible to obtain practical estimates. The depth-dependent sound field and the electro-acoustical pulse spectrum introduce errors in the estimation process which increase the sd of the estimates. A method is shown in this chapter that enables adequate correction and quantify the increase in sd due to the correction. The acousto-spectrographic features measure local medium features assuming homogeneity conditions. In practice this appears not to be realistic, and thus a local inhomogeneity factor is introduced which measures the variation of medium parameters. When measuring liver tissue, a global inhomogeneity in addition to the local inhomogeneity is also observed, which is due to inter-individual spread of feature values.

An expression for the sd of the attenuation slope (one of the four features studied in this paper) has been the topic in a number of articles (Kuc and Taylor, 1982; Kuc, 1985; Parker, 1986; Berger et al., 1987; Romijn et al., 1989). Yao (1991) also analyzed the sd of the backscatter features. The formulas only describe sd under theoretical conditions and vary due to different levels of approximations and feature extraction methods. Formulas for the sd of all four features will be derived, using as few approximations as possible. With simulated RF data it will be shown that they accurately predict the sd of each feature over a wide range of measurement conditions. Finally, a set of *in vivo* normal liver measurements is analyzed and used to estimate the local and global inhomogeneity in the liver.

This chapter is organized as follows. First, the theoretical signal model is described which is subsequently used in the second section to present the feature extraction method. The third section uses both the model and the method to derive the sd of the features. In the following section attention is focussed on the transducer-dependent deviations: measurement of transducer characteristics (TC) is described, as well as the effect of correction on the feature deviations. The results section presents sd's observed in phantom and normal *in vivo* liver data. Finally, conclusions are summarized and future work is discussed.

2.2 Theory

Assuming a homogeneous tissue model, the *amplitude* spectrum of the backscattered echo signal received in pulse-echo mode $\boldsymbol{E}(f,z)$ is a random variable (indicated by a bold symbol) with Rayleigh-distributed amplitudes, and an average value $\mu(f,z)$ that can be described by a linear model (Oosterveld et al., 1991):

$$\begin{aligned} Pr\left\{\boldsymbol{E}(f,z)=E(f,z)\right\} &= \frac{\pi E(f,z)}{2\mu^2(f,z)}\exp\left(-\frac{\pi E^2(f,z)}{4\mu^2(f,z)}\right) & (2.1)\\ \mu(f,z) &= P^2(f)D^2(f,z)T^2(f,z)S(f), & (2.2)\end{aligned}$$

where $E(f,z)$ is the received amplitude at temporal frequency f of the backscattered echoes of a small tissue volume at depth z, $P^2(f)$ is the acousto-electrical transfer function of the transducer, $D^2(f,z)$ is the diffraction spectrogram of the transducer, $T(f,z)$ is the tissue transfer function, and $S(f)$ is the backscatter function.

The terms $P^2(f)$ as well as $D^2(f,z)$ in Eq. 2.2 jointly describe the transducer characteristics (TC). Without a proper correction procedure, they will affect the extracted features (Cloostermans and Thijssen, 1983). Section 2.5 describes TC measurement methods capable of estimating both terms. After correction, the remaining two terms in Eq. 2.2 are $T^2(f,z)$, and $S(f)$, which describe the tissue. They are developed further to show how the four tissue features are involved in the model.

A general expression for the tissue transfer function is:

$$T(f,z) = 10^{-0.05a(f)z}, \tag{2.3}$$

where $a(f)$ is the attenuation coefficient [dB/cm]. Pauly and Schwan (1971) showed that the attenuation coefficient could be approximated by a linear model. The coefficients of the linear model in a limited frequency range can be shown to produce an estimate of a causal relaxation model (Jongen et al., 1986; Berkhoff et al., 1996). The following, linear model is used:

$$a(f) = a_0 + a_1(f - f_\mathrm{c}), \tag{2.4}$$

where f_c is the central frequency in the available bandwidth, which are both fixed parameters dependent on the echographic system, a_0 is the attenuation intercept at the central frequency [dB/cm], and a_1 is the attenuation slope [dB/cm MHz].

A general expression for the backscatter function is:

$$S(f) = 10^{0.05b(f)}, \tag{2.5}$$

where $b(f)$ is the backscatter coefficient [dB]. In a limited frequency range, the backscatter coefficient exhibits quasi-linear shapes (Lizzi et al., 1987; Romijn et al., 1989), and can thus be approximately described by:

$$b(f) = b_0 + b_1(f - f_\mathrm{c}), \tag{2.6}$$

where b_0 is the backscatter intercept at the central frequency [dB], and b_1 is the backscatter slope [dB/MHz].

The Rayleigh probability density function (pdf) is due to the assumed microstructure of the medium: many, small (compared to the wavelength), and randomly positioned scatterers. The received backscattered echo signal at the surface of a piezo-electric transducer is the result of the phase-sensitive addition of randomly phased backscattered echoes from many, small scatterers from this microstructure. The amplitude of the received signal is the result of the classical random walk problem, which was shown to produce Rayleigh-distributed amplitudes in the cases of laser light (Goodman, 1975) and ultrasound (Burckhardt, 1978; Wagner et al., 1983).

2.2.1 Medium-dependent transducer characteristics

The model as presented in Eq. 2.2 assumes that the diffraction spectrogram $D(f,z)$ is separable from the medium backscatter characteristics $S(f)$. If this is true, then the diffraction spectrogram measured in an artificial medium is equal to that measured in tissue. The latter observation has been used by many researchers in measuring the diffraction spectrogram using plane reflectors (O'Donnell, 1983; Lizzi et al., 1983; Madsen et al., 1984), using foam phantoms (Cloostermans and Thijssen, 1983; Fink and Cardoso, 1983), or analytically (Insana et al., 1994). However, Robinson et al. (1984) report that: “corrections obtained from T.M. [tissue-mimicking] phantom

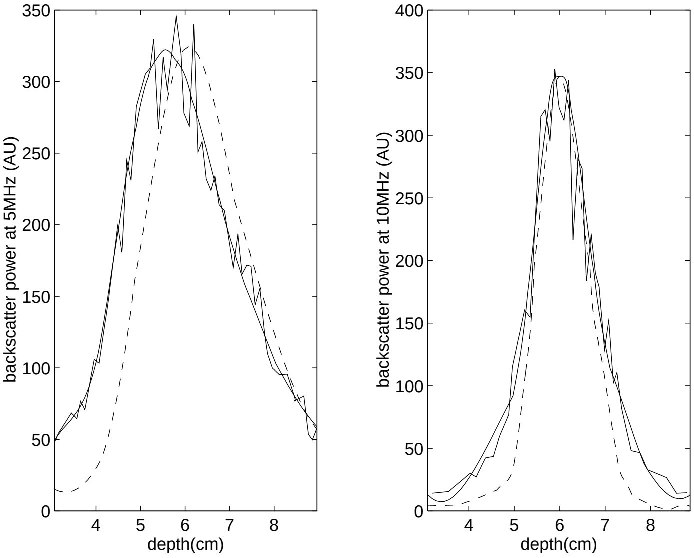

Figure 2.1 Simulated backscatter spectral power at 5 and 10 MHz of a 1.5 cm diameter, 6 cm focus single element transducer. Irregular curve: cloud of scatterers, smooth curve: single scatterer, dashed curve: plane reflector. (From Verhoef, 1985.)

material differ from those obtained using *in vivo* tissue as the reflector”. They compared flat plate, small scatterer phantoms, and *in vivo* diffraction spectrograms and found that they differed markedly. Laugier et al. (1987) conclude that: “ . . . the best accuracy is reached . . . if the transducer is calibrated *in vivo* on the organ with unknown attenuation.” Céspedes and Ophir (1990) also acknowledge the problem and use a special transducer setup to acquire simultaneously signal as well as estimating diffraction through a so called axial beam translation technique.

A good example of the dependency of measured diffraction on the medium was shown by Verhoef et al. (1985). They carried out simulations using single scatterer, multiple random scatterers, and a plane reflector. Their results are shown in Fig. 2.1. The diffraction effect measured from a single scatterer is shown to coincide very well with the average backscatter spectrum of a cloud of random scatterers. The apparent diffraction measured with a plane reflector markedly deviates from the single scatterer curve. They concluded: “it will be clear that the use of flat plate reflections for the estimation of the diffraction factor is incorrect in backscatter estimation”.

It will be shown that the diffraction spectrogram measured on foam phantoms allows for depth-independent measurements on independent foam data. The same diffraction spectrogram when used on *in vivo* liver data is shown not to provide adequate correction. Using a diffraction spectrogram obtained from *in vivo* data did result in depth-independent measurements.

2.3 Feature extraction method

An essential feature of any biomedical measurement system is that it has to tackle the *in vivo* measurement conditions. That is, clinically realistic measured echo data is affected in many areas by big and small blood vessels, ligaments, and acoustic shadowing that are not included in the homogeneous signal model. These areas drastically affect the extracted features and should thus be avoided. A strategy is incorporated throughout the feature extraction to avoid these areas. A mask matrix is used in which it is indicated for each sample to which area it belongs, and any sample not marked belongs to homogeneous tissue of the organ of interest. The mask matrix is initially filled manually by outlining: the organ boundary (samples outside the organ are marked), and unwanted structures within the organ, such as major blood-vessels. An overflow detection step then marks those samples that were out of range in the A/D conversion step. Then, an iterative detection technique automatically marks hyper or hypo echoic windows (average signal power in the window is outside a 95% reliability interval, which is estimated over all windows in the organ). Underflow areas are excluded by marking windows that have a low signal-to-noise power ratio. Finally, a small blood-vessel detection method extends the detection capabilities to detect small structures which could easily be missed during manual outlining, and are in the order of the window size, which makes them difficult to detect using a spectral window. The detection of these small structures requires one extra iteration. The attenuation is first estimated with the available mask, attenuation and diffraction are then used to correct each acquired RF line, which are then envelope-detected. The resulting envelope image is smoothed and then thresholded. This results in the required mask. The smoothing window size determines the size of the detected structures.

The estimation starts by calculating the spectrogram of each RF line in a selected region-of-interest (ROI). An average spectrogram is calculated by averaging over all lines in the ROI, excluding the windows in a spectrogram that contain any marked samples in the mask matrix. The average spectrogram is denoted by $\overline{E}(f,z)$.

The estimation then continues by removing the estimated transducer characteristics (see section 2.5) from the average spectrogram. After division of $\overline{E}(f,z)$ by the two terms comprising the estimated TC ($\hat{P}^2(f), \hat{D}^2(f,z)$), an estimated tissue transfer function and backscatter function ($\hat{T}^2(f,z)\hat{S}(f)$) remain.

The next step is to log transform the TC corrected, average spectrogram. Using Eqns. 2.2, 2.3, and 2.5, the result can be written as follows:

$$\begin{aligned} \boldsymbol{LME}(f,z) &= 20\log_{10}\left(\frac{\overline{E}(f,z)}{\hat{P}^2(f)\hat{D}^2(f,z)}\right) \\ &= 20\log_{10}\left(\hat{T}^2(f,z)\hat{S}(f)\right) = 2\hat{a}(f)z + \hat{b}(f) + \boldsymbol{\epsilon}, \end{aligned} \tag{2.7}$$

where $\boldsymbol{LME}$ is a random variable resulting from the log of the mean of the spectrogram, the operator $\hat{}$ indicates the estimated variable, and $\boldsymbol{\epsilon}$ is a zero mean, Gaussian random variable, which will be shown in the next subsection.

Attenuation is estimated using the method described by Cloostermans et al. (1983) and Fink et al. (1983). A least squares straight line is fitted with depth for each frequency of the spectrogram LME(f,z). As can be observed from Eq. 2.7, the slope is an estimate of the attenuation

coefficient, and the intercept is an estimate of the backscatter coefficient. This method will be referred to as multi narrow band (MNB). The estimated attenuation coefficient $\hat{a}(f)$ is used again in a second linear fit, which results in an estimate of both features from Eq. 2.4. The resulting backscatter coefficient $\hat{b}(f)$ is also used in a second linear fit which results in an estimate of both features from Eq. 2.6.
The frequency bandwidth in which the feature extraction methods accurately operate is limited by the digitizing system, and a noise floor from the electronic amplifiers (Kuc, 1985). The TGC amplifier was setup such that the average amplitude of the digitizer output signal at each depth was always between 50% and 100% of the maximum output value. Under these conditions, it was observed from the sd estimates of the attenuation coefficient that the estimation methods best operate within a bandwidth such that all frequency components at all depths are within -12 dB of the maximum spectral amplitude of the RF spectrogram before TGC correction.

2.4 The standard deviation of attenuation and backscatter features

The signal model and the estimation method being available, it is now possible to derive the sd's and discuss any bias of the feature estimates. First, the sd of the estimated LME spectrogram is derived. This result is then used to derive the sd's of the attenuation and backscatter coefficient. The sd of the fit to the coefficients then leads the sd of slope and intercept. This section concludes with an investigation of factors influencing sd in practice.

2.4.1 The standard deviation of log average amplitude spectrogram

The amplitude spectrum $\boldsymbol{E}(f,z)$ is modeled as a random variable with a Rayleigh pdf (see section 2.2). For Rayleigh pdf, it can easily be shown that (Papoulis, 1991):

$$\sigma_{\boldsymbol{E}(f,z)} = \mu_{\boldsymbol{E}(f,z)}\sqrt{\frac{4-\pi}{\pi}} \approx \mu_{\boldsymbol{E}(f,z)}/1.91, \tag{2.8}$$

where $\mu_{\boldsymbol{E}(f,z)}$ and $\sigma_{\boldsymbol{E}(f,z)}$ are respectively the mean and the sd of the echo amplitude at frequency f. To decrease the sd of the features, the average amplitude spectrum $\overline{E}(f)$ is used. If N independent lines are averaged, then, if N is large enough, the resulting average spectrogram is again a random variable, but with a Gaussian pdf, due to the central limit theorem (Papoulis, 1991), and mean and standard deviation:

$$\begin{aligned} \mu_{\overline{\boldsymbol{E}}(f,z)} &= \mu_{\boldsymbol{E}(f,z)} && (2.9) \\ \sigma_{\overline{\boldsymbol{E}}(f,z)} &= \sigma_{\boldsymbol{E}(f,z)}/\sqrt{N} = \mu_{\boldsymbol{E}(f,z)}/(1.91\sqrt{N}) && (2.10) \end{aligned}$$

As was shown in the previous section, the features are estimated from the log transform of $\overline{E}(f)$. If N is large enough, the sd is small compared to the mean, and the sd of the log transformed variable is estimated using the first order Taylor approximation of the log operator ($20\log_{10}(x+$

$\Delta) \approx 20\log_{10}(x) + 8.69\Delta/x)$. Thus the mean and sd of the log transformed variable become:

$$\mu_{\boldsymbol{LME}(f,z)} = 20\log_{10}(\mu_{\boldsymbol{E}(f,z)}) = 2\hat{a}(f)z + \hat{b}(f) \tag{2.11}$$

$$\sigma_{\boldsymbol{LME}(f,z)} = 8.69\sigma_{\overline{\boldsymbol{E}}(f,z)}/\mu_{\overline{\boldsymbol{E}}(f,z)} = \frac{4.54}{\sqrt{N}} \tag{2.12}$$

The sd of the log average spectrogram has become independent of the average value, and is a constant that depends on N only, $\sigma_{\boldsymbol{LME}(f,z)} = \sigma_{\boldsymbol{LME}}$! The log average transform thus results in a homoscedastic random variable with additive, Gaussian noise. Eq. 2.12 is equivalent to that by Parker (1986, Eq. 20; he used the natural logarithm).

2.4.2 Standard deviation of the attenuation and backscatter coefficient

Assume $\boldsymbol{LME}(f_k, z_l)$ contains L independent spectra $(z_l, l = 1 \ldots L)$, and K discrete, independent frequencies $(f_k, k = 1 \ldots K)$. A linear least-squares fit to $\boldsymbol{LME}(f_k, z_l)$ with depth is optimal, because (see Eq. 2.7) $\boldsymbol{\epsilon}$ is an additive Gaussian noise term. Under such conditions, it can be shown that the attenuation and backscatter coefficient features also have a Gaussian distribution (Kleinbaum et al., 1988). Assuming L large enough, the sd of the attenuation and backscatter coefficient is very well approximated by (Appendix A):

$$\sigma_{\hat{a}(f_k)} \approx \frac{\sqrt{3}\sigma_{\boldsymbol{LME}}}{D\sqrt{L}} \quad [\mathrm{dB/cm}] \tag{2.13}$$

$$\sigma_{\hat{b}(f_k)} \approx \frac{2\sigma_{\boldsymbol{LME}}}{\sqrt{L}}\sqrt{1 + 3\delta + 3\delta^2 - \frac{3+6\delta}{2L}} \quad [\mathrm{dB}], \tag{2.14}$$

where D is the ROI length ($D = \Delta z L$), and δ is the relative distance to the first spectrum ($= z_1/D$), and $\sigma_{\boldsymbol{LME}}$ is given by Eq. 2.12.

The sd of the backscatter coefficient thus decreases with an increasing ROI length, and increases with an increasing delay. The latter term within the big square root is a correction term that is effective whenever the number of spectra is low and/or the relative delay is high. As is seen from Eqns. 2.13 and 2.14, the sd's are independent of frequency, thus $\sigma_{\hat{a}(f_k)} = \sigma_{\hat{a}}$, and $\sigma_{\hat{b}(f_k)} = \sigma_{\hat{b}}$.

The approximations in Eqns. 2.13 and 2.14 were verified by a straightforward simulation of the model specified in Eq. 2.7. Figure 2.2 shows the predicted (solid line) and measured (data points) sd's for the attenuation and backscatter coefficient. The theoretical predictions fit the simulated measurements very well even at a very low number of windows ($L = 3$)!

2.4.3 Standard deviation of the attenuation and backscatter slope and intercept

The four features are the two slopes and two intercepts from the attenuation and backscatter coefficients. The sd of the coefficients was shown not to depend on the frequency, again an additive Gaussian model can be used with the accompanying least-square fit. The four acousto-spectrographic features from the signal model are estimated in an optimal sense, i.e. zero bias, and minimal sd.

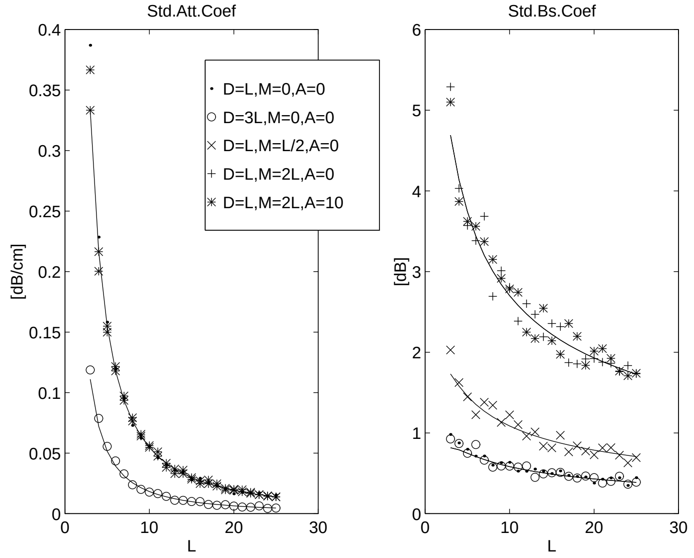

Figure 2.2 Simulated (data points) vs. predicted (solid line) sd's of the attenuation and backscatter coefficients. Each data point is estimated from 100 realizations, $\sigma_{\boldsymbol{LME}} = 1$. As expected the sd of the attenuation coefficient depends on L as well as D, but not on the delay (M is the delay expressed in number of windows). The backscatter coefficient depends on L as well as the delay, but not on D.

The estimated attenuation coefficient can be modeled as:

$$\boldsymbol{a}(f_k) = a_0 + a_1(f_k - \overline{f}) + \boldsymbol{\epsilon}_a, \tag{2.15}$$

where the central frequency is assumed to be the midpoint frequency ($\overline{f}$) in the available bandwidth, and $\boldsymbol{\epsilon}_a$ is an additive Gaussian distributed noise term ($p(\epsilon_a) = N(0, \sigma_{\hat{a}})$). If the number of frequencies is much larger than 1, and using a similar derivation as in Appendix A, the sd of the slope is given by Eq. 2.32. The intercept is at central frequency, Eq. 2.29 can directly be simplified to $\sigma_b^2 = \sigma^2/N$. Replacing depth by frequency and using Eq. 2.13 results in:

$$\sigma_{a_0} = \frac{\sigma_{\hat{a}}}{\sqrt{K}} \approx \frac{\sqrt{3}\sigma_{\boldsymbol{LME}}}{D\sqrt{KL}} \quad [\mathrm{dB/cm}] \tag{2.16}$$

$$\sigma_{a_1} \approx \frac{\sqrt{12}\sigma_{\hat{a}}}{W\sqrt{K}} \approx \frac{6\sigma_{\boldsymbol{LME}}}{DW\sqrt{KL}} \quad [\mathrm{dB/cmMHz}], \tag{2.17}$$

where W is the bandwidth in [MHz] ($W = \Delta f K$). The backscatter coefficient can be modeled as:

$$\boldsymbol{b}(f_k) = b_0 + b_1(f_k - \overline{f}) + \boldsymbol{\epsilon}_b, \tag{2.18}$$

where $\boldsymbol{\epsilon_b}$ is an additive Gaussian distributed noise term $(p(\epsilon_b) = N(0, \sigma_{\hat{b}})$. If the number of frequencies is much larger than 1, then:

$$\sigma_{b_0} = \frac{\sigma_{\hat{b}}}{\sqrt{K}} \approx \frac{2\sigma_{\boldsymbol{LME}}}{\sqrt{KL}} \sqrt{1 + 3\delta + 3\delta^2 - \frac{3+6\delta}{2L}} \quad [\mathrm{dB}] \tag{2.19}$$

$$\sigma_{b_1} \approx \frac{\sqrt{12}\sigma_{\hat{b}}}{W\sqrt{K}} \approx \frac{4\sqrt{3}\sigma_{\boldsymbol{LME}}}{W\sqrt{KL}} \sqrt{1 + 3\delta + 3\delta^2 - \frac{3+6\delta}{2L}} \quad [\mathrm{dB/MHz}] \tag{2.20}$$

The term $\sqrt{KL}$ can be developed even further. D and W are related via the window duration T. Using $\Delta f = 1/T$, and $\Delta z = cT/2$ (no overlap) the product becomes $\sqrt{KL} = \sqrt{DW}/\sqrt{c/2}$, where c is the speed of sound in the medium. The sd of the slopes and intercepts then become:

$$\sigma_{a_0} \approx \frac{0.5\sqrt{6c}\sigma_{\boldsymbol{LME}}}{D\sqrt{DW}} \quad [\mathrm{dB/cm}] \tag{2.21}$$

$$\sigma_{a_1} \approx \frac{3\sqrt{2c}\sigma_{\boldsymbol{LME}}}{DW\sqrt{DW}} \quad [\mathrm{dB/cmMHz}] \tag{2.22}$$

$$\sigma_{b_0} \approx \frac{\sqrt{2c}\sigma_{\boldsymbol{LME}}}{\sqrt{DW}} \sqrt{1 + 3\delta + 3\delta^2 - \frac{3+6\delta}{2L}} \quad [\mathrm{dB}] \tag{2.23}$$

$$\sigma_{b_1} \approx \frac{2\sqrt{6c}\sigma_{\boldsymbol{LME}}}{W\sqrt{DW}} \sqrt{1 + 3\delta + 3\delta^2 - \frac{3+6\delta}{2L}} \quad [\mathrm{dB/MHz}] \tag{2.24}$$

The above equations were verified by simulation. Figure 2.3 shows the predicted (solid line) and measured (data points) sd's for the slope and intercept of the attenuation and backscatter coefficient. The predictions fit the simulated measurements very well.

2.4.4 Standard deviation in practice

Five factors will be considered that may influence the theoretical estimates of the sd derived previously. The relevant factors will be selected and it will be shown how they are used to convert a theoretical sd estimate into a realistic estimate.

The first factor concerns the conversion of RF lines into spectrograms. In theory, the RF spectrogram, LME(f_k, z_l), is assumed to be comprised of independent components. In practice, the spectrogram is calculated from the RF time domain signal $e(t)$ using a short term Fourier transform (STFT, or periodogram (Welch, 1967)). In short, the STFT divides $e(t)$ into L windows. Window l is used to calculate the backscattered amplitude spectrum from a tissue volume at depth z_l. The window is selected from $e(t)$ by applying a window function $w(t)$ at $t_l = z_l * c/2$. The spectrogram then becomes:

$$E(f, z_l) = |\mathcal{F}\{e(t)w(t - t_l)\}|, \tag{2.25}$$

where $|\mathcal{F}|$ denotes the absolute value of the Fourier transform (or frequency amplitude). Three features need to be set: the type and length of the window function and the level of overlap between two windows. The effect of the choice and type of window on the attenuation slope

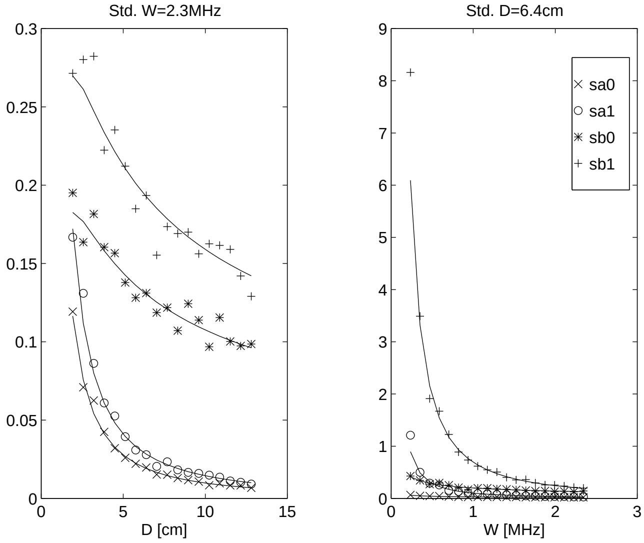

Figure 2.3 Simulated (data points) vs. predicted (solid line) sd's of slope (sa1,sb1) and the intercept (sa0, sb0) of the attenuation and backscatter coefficient. Each data point is estimated from 100 realizations, $\sigma_{LME} = 1$.

has been investigated (Kuc, 1985; Akita and Ueda, 1988); this chapter extends this research to include the backscatter features as well.

Two experiments were carried out on a dataset of simulated RF signals under plane wave conditions, without attenuation, without diffraction, and using point scatterers. A Gaussian-shaped 3.75 MHz, 1.87 MHz bandwidth (-6dB) pulse spectrum was used and the scatterer density within the pulse length was set at 10 scatterers, resulting in Rayleigh-distributed amplitudes, in which the condition defined in Eq. 2.8 was shown to be true. One hundred acquisitions with 80 RF lines were generated and the four features were calculated as previously described using either a rectangular window, or a Hanning window.

In experiment 1, the window length was varied from 32 to 256 samples, with non-overlapping windows. Figure 2.4 shows the sd and bias on the estimates. Firstly, it is observed that the rectangular window produces lower sd than the Hanning window. Secondly, the rectangular window sd ('o') coincides very well with the theoretical sd ('x'). Finally, the bias is very low for both types of windows.

It is known that using overlapping windows decreases sd compared to using non-overlapping windows in the calculation of the power spectrum (which is comparable to attenuation and backscatter coefficients). From Welch (1967), it can be concluded that using windows overlapping by 50% results in minimized sd of the attenuation and backscatter coefficients. The effect on the sd of the slope and intercept estimated from these coefficients is unclear. A second experiment was carried out to study the effect overlap has on the sd of the slopes and intercepts calculated from

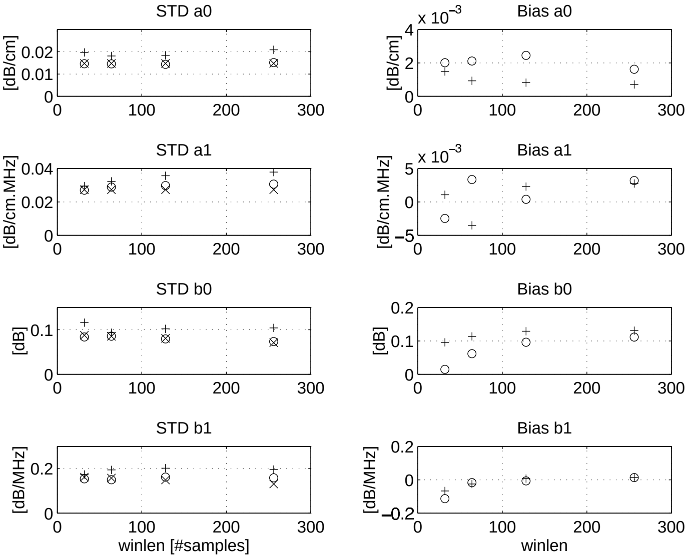

Figure 2.4 Estimated sd and bias of the four features from 100 simulated 80 line, 1024 samples RF data using rectangular (o), or Hanning (+) window. Theoretical sd (x) was calculated; theoretical bias is zero. The window length was varied while using non-overlapping windows.

the coefficients. Figure 2.5 shows that overlapping has little or no effect in case of rectangular windows. Furthermore, increased overlap decreases the sd of the Hanning windows up until an overlap of 50%, where Hanning windows sd's become comparable to rectangular window sd's. From the two experiments it is concluded that the effect of the spectrogram calculation on the sd of the features is negligible and sd is rather insensitive to the choice of windowing function, type, and overlap.

The second factor, ξ_{bo}, concerns the averaging of spectrograms into one average spectrogram. Overlapping of beams effectively decreases the effective number of rf lines (Kuc, 1985). The lateral correlation distance was estimated to be 2.5 lines. Thus the effective number of lines used in Eq. 2.12 decreases by a factor 2.5, which amounts to multiplying the predicted sd's by $\xi_{bo} = \sqrt{2.5} = 1.58$.

The third factor, ξ_{dc}, is due to imperfections in correcting for the TC. Imperfect correction demonstrates itself as a depth-dependency of the features. If the depth is ignored, the effect of the dependency is an increase in sd. The factor ξ_{dc} measures this increase.

The fourth and fifth factors, local (ξ_{li}) and global (ξ_{gi}) inhomogeneities, both reflect the physical properties of the backscattering medium. In *in vivo* liver measurements and even in phantom measurements, the measured sd was higher than expected. This effect can be the result of inhomogeneous physical properties. The factor ξ_{li} is the excess sd within one sample of a medium as compared with theory. The factor ξ_{gi} also measures excess sd, but between different samples of a medium. In other words, the expected sd within one liver is ξ_{li} times the theoretical value,

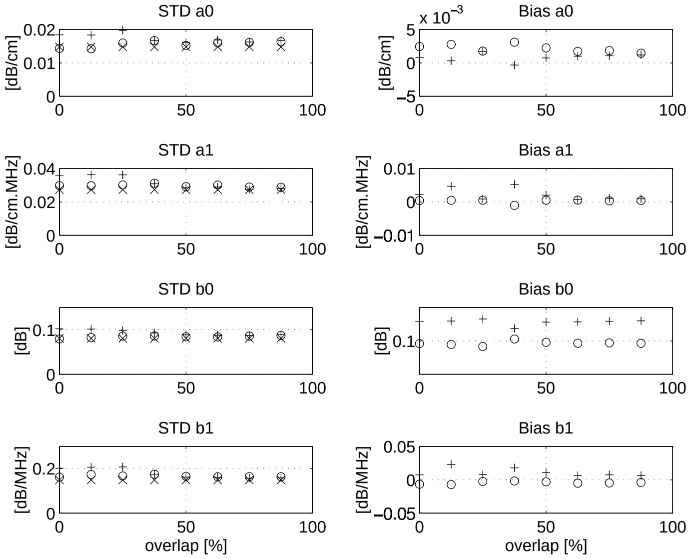

Figure 2.5 Estimated sd and bias of the four features from 100 simulated 80 line, 1024 samples RF data using rectangular (o), or Hanning (+) window. Theoretical sd (x) was calculated; theoretical bias is zero. The level of overlap was varied while using 128-point windows.

whereas the sd measured over a number of livers is $\xi_{li}\xi_{gi}$ times the theoretical value.
To conclude this section, it was shown that the first factor (spectrogram calculation) can be disregarded. The theoretical sd $\sigma_{x,th}$ of feature x, should thus be multiplied by the remaining four inhomogeneity factors to arrive at a practical estimate of the sd:

$$\sigma_{x,pract} = \xi_{x,li}\xi_{x,gi}\xi_{x,dc}\xi_{x,bo}\sigma_{x,th}, \tag{2.26}$$

where $\xi_{x,bo} = 1.58$.

2.5 Transducer characteristics estimation

Up until now the effect of the transducer on the feature has been neglected, because data were simulated under plane wave conditions. For the theory to be tested on actual data, adequate transducer characteristics (TC) estimation has to take place. A Toshiba-T270A scanner was applied using the 3.75 MHz PSF37-CT phased array transducer in single focus mode (F=7.5 cm). As explained at the introduction of this chapter, RF signals are acquired without effects of manual gain and or TGC control of the scanner. In the section 2.2, the TC was defined as the product of $P^2(f)$, the acousto-electrical transfer function of the transducer, and $D^2(f, z)$, the diffraction spectrogram of the transducer.

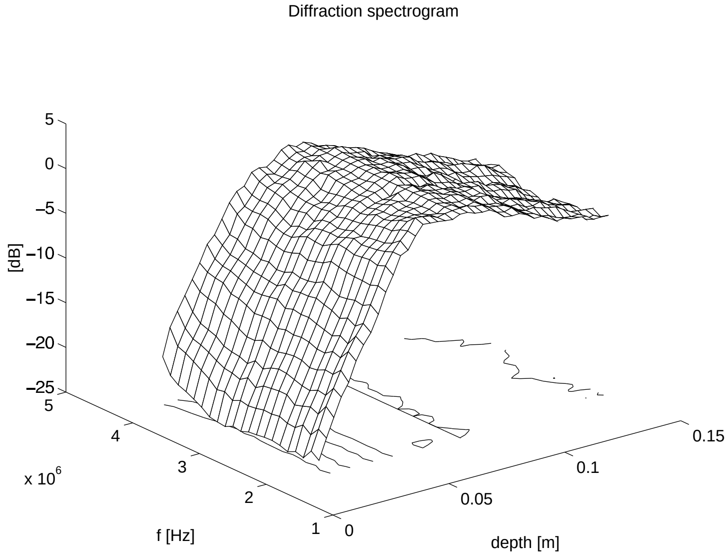

Figure 2.6 Estimated diffraction spectrogram of Toshiba PSF37-CT transducer using reticulated foam

As explained in section 2.2, the diffraction could be medium-dependent. Therefore an experiment was set out to investigate the influence of the medium on the TC estimation. Three different media were used: foam, rubber, and liver. The foam medium is a 90 ppi (90 pores per inch; 3.54 pores per millimeter) reticulated polyurethane cellular network which is entirely open (Bulpren S90, Recticel, Kesteren, The Netherlands). The foam is immersed into water and thoroughly degassed using a (0.2 mbar end pressure) vacuum pump (S1.5, Leybold AG, Köln, Germany). The rubber medium is a Model 539 Multi-purpose phantom (ATS Laboratories, 404 Knowlton St., Bridgeport, CT, 06608, USA). The rubber phantom contained test structures for quality assurance purposes. The condition defined in Eq. 2.8 was verified to hold for both phantoms. *In vivo* liver data were acquired from 7 male and 5 female normals, examined at 9.00 h. before breakfast. At least four lateral and four transverse acquisitions in the right liver lobe were made, while avoiding regions with high concentrations of blood-vessels. Two methods of TC estimation were used: absolute, and relative. The foam TC was measured using an absolute method, the rubber and liver TC were estimated using a relative method.

The absolute TC (on foam) was estimated using a method well known in literature (Insana et al., 1983; Oosterveld et al., 1991). The procedure was as follows. Place a volume of the medium in a water tank and orient its planar surface perpendicular to the beam axis. Record 1200 echo signals from adjacent, non overlapping lines of sight. In each line, calculate the amplitude spectrum of a 128 point segment just beneath the surface, and average over all 1200 lines. Repeat this over a range of transducer-foam distances. The averaged spectra are then stacked into one, average spectrogram. The estimated diffraction spectrogram $\hat{D}_{abs}(f,z)$ is obtained by dividing the average spectrogram by its focus spectrum, which is the maximum energy spectrum. Figure

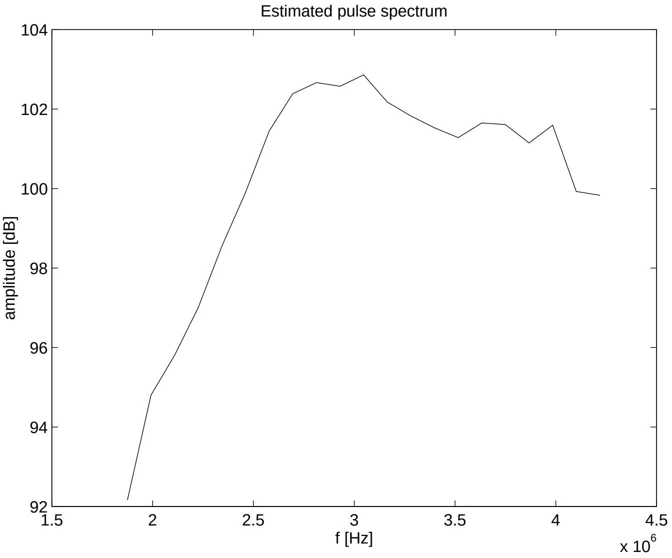

Figure 2.7 Estimated pulse spectrum of Toshiba PSF37-CT transducer using reticulated foam.

2.6 shows the diffraction spectrogram; notice that it is flat in the focus (because of the division). Next, the acousto-electric spectrum $P_{abs}(f)$ should be estimated from a flat plate reflection at the focus (Nicholas et al., 1982; Ueda and Ozawa, 1985). It was not possible to record a reliable flat plate reflection due to multiple reflections caused by previously emitted pulses, and overflow due to the high reflectivity of the flat plate. Therefore, $P_{abs}(f)$ was measured indirectly. The backscatter coefficient of the foam was measured in a laboratory setup (Ueda and Ozawa, 1985). The foam focus spectrum divided by the laboratory estimated backscatter coefficient is an indirect estimate of $P_{abs}(f)$. Figure 2.7 shows this pulse spectrum. The above method estimates TC in an absolute sense, i.e., the correction by an absolute TC results in absolute attenuation and backscatter measurements. The foam TC was measured independently from the foam acquisitions used in feature measurements.

The relative TC (on rubber and liver) was estimated using the following procedure. A maximum number of independent acquisitions was made on the medium. Next, the homogeneous STFT windows of all the lines in all acquisitions are averaged ($>$900 windows in rubber, and $>$5000 in human liver). The result is an average spectrogram of the medium. In the same manner as above, the estimated diffraction spectrogram $\hat{D}_{rel}(f,z)$ is obtained by dividing the average spectrogram by its focus spectrum, which was chosen to be the maximum energy spectrum. The acousto-electric spectrum $\hat{P}_{rel}(f)$ is estimated by the focus spectrum. It has already been assumed that the media are homogeneous, thus the average spectrogram will contain, besides the diffraction spectrogram and the acousto-electric transfer function, also the average attenuation and backscatter coefficient. It follows that the resulting feature measurements using the relative

TC will be relative to the medium used. Thus for normal liver measurements corrected with relative normal liver TC, the average estimated feature should be zero. Interestingly, if the feature is significantly (using sd) non-zero, then a ROI should be considered abnormal. Relative TC does not measure features in an absolute sense, but still has the diagnostic information at hand. Actually, the procedure to calculate the relative TC is a little more complicated, because the rubber, as well as the liver medium, contains non-homogeneous tissue regions (e.g. blood vessels, reflectors). The methods described in section 2.3 provide manually outlined organs and automatically detected non-homogeneous regions. These regions were used in estimating the relative TC, by skipping windows that contained such a region.

As can be seen from Figures 2.6 and 2.7, the TC estimates still show some noise, although each spectrum is the result of averaging 1200 spectra. TC correction not only removes the effect of the TC, but if a limited number of lines is used, the TC estimate itself is a noisy estimate (cf. Eq. 2.12) and will add noise as well, decreasing precision. To reduce the amount of noise introduced, the number of averaged RF lines in TC estimation should be high. This number depends on the amount of noise on LME expected in the ROIs when measuring features. The amount of noise in a ROI depends on the number of lines (Eq. 2.12). The maximal ROI size covers 110 lines. The number of lines in TC estimation should be much higher than the number of lines in a ROI. About 10 times the maximal number of lines in a ROI was taken and no influence was found on the precision of the estimated features.

Finally, two extra TCs are estimated. Firstly, the relative normal human liver TC was estimated using all available normal human liver acquisitions of all persons. In evaluating the efficacy of the TC correction, the same human liver material is used. Thus, a ROI in a liver being investigated is TC-corrected with data that contains information from that same liver. To avoid this so-called re-substitution effect, the leave-one-out (LOO) estimate of liver TC is also calculated. The LOO estimate is the TC estimation from all livers except the liver currently being investigated. In the experiments, it is indicated with ’liver loo’. The second extra TC is a flat TC, to present an upper bound on TC correction error. It is a diffraction spectrogram and a pulse spectrum filled with ones, and represents the case where no diffraction correction is applied. In the experiments it is indicated with ’none’.

2.6 Results

It has been shown that four factors convert the theoretical sd estimates (Eqns. 2.21 – 2.24) into practical estimates (Eq. 2.26). The effect due to beam overlap was known in advance, in this section the remaining three factors are estimated in two experiments. An explanation on how to estimate a factor is given in Appendix B.

2.6.1 Experiment 1

Features within the foam phantom were measured. Three types of materials were used for TC estimation: foam, rubber, or a flat diffraction spectrogram. The results are shown in Table 2.1. The TC type is indicated in column 1; each was explained in the previous paragraph. The type of inhomogeneity factor being measured is indicated in column 2 by mnemonics, which are

Foam inhomogeneity estimates					
TC	type	a0	a1	b0	b1
foam	li	1.15 (1.10-1.19)	0.97 (0.93- 1.00)	2.00 (1.92-2.07)	1.57 (1.51-1.63)
	dc	1.15 (1.11-1.19)	1.03 (0.99- 1.07)	1.07 (1.03-1.11)	1.02 (0.98-1.05)
	mo	1.00 (0.97-1.04)	1.00 (0.96- 1.04)	1.00 (0.97-1.04)	1.00 (0.96-1.03)
rubber	li	1.14 (1.10-1.19)	0.97 (0.93- 1.00)	1.99 (1.92-2.07)	1.57 (1.51-1.62)
	dc	1.25 (1.20-1.29)	1.73 (1.67- 1.79)	1.18 (1.13-1.22)	1.74 (1.68-1.81)
	mo	1.00 (0.96-1.04)	1.00 (0.96- 1.04)	1.00 (0.96-1.03)	1.00 (0.96-1.04)
flat	li	1.14 (1.09-1.18)	0.96 (0.93- 1.00)	1.97 (1.90-2.05)	1.58 (1.52-1.64)
	dc	17.4 (16.7-18.0)	1.29 (1.25- 1.34)	16.8 (16.2-17.5)	1.21 (1.17-1.26)
	mo	1.00 (0.96-1.04)	1.00 (0.96- 1.04)	1.00 (0.96-1.04)	1.00 (0.96-1.04)

Table 2.1 Inhomogeneity factors for foam data using various diffraction correction methods. Mnemonics: li is local inhomogeneity, dc is diffraction correction, and mo is model.

explained in the caption. The following four columns show the inhomogeneity for each feature. In between brackets, the 95% confidence interval of the point estimate is indicated.

It is observed that, for all TC types, the local inhomogeneity estimates are the same. This is to be expected as these inhomogeneities are estimated with fixed depth of the ROI. The local inhomogeneity is insignificant for the attenuation slope ($\xi_{li,a1}$), but is significant for the other features. This indicates that the underlying physical features within the foam show local fluctuations.

The inhomogeneity due to diffraction correction (ξ_{dc}) varies with the type of TC. It is clear that foam-estimated TC results in the lowest (ξ_{dc}) values: both slope inhomogeneities are not significant, and both intercept features are smaller than the other TC types. From this experiment, it can be concluded that foam data cannot be corrected with a TC estimated in 'rubber', although both media are assumed to be tissue-mimicking media.

Finally, the remaining inhomogeneity was estimated. The whole dataset was transformed by subtracting one global average value, then each feature was divided by the expected sd using Eq. 2.26. The resulting inhomogeneity describes how well the model fits, and it is found not to be significantly different from 1. Thus, the sd model comprising the theoretical estimate times the various factors describes the data very well.

2.6.2 Experiment 2

Features within *in vivo* normal livers were measured in the same manner as with the phantom. Four types of TCs were now used: foam, rubber, none, and average human liver. The results are shown in Table 2.2. The global inhomogeneity measures the increase in sd when measuring different livers, whereas the local inhomogeneity measures increase due to inhomogeneity within the liver.

It is observed that, for all TC types, the local and global inhomogeneity estimates are the same. This is to be expected, as these are estimated with fixed depth of the ROI. The local inhomogeneity is very high for both attenuation intercept ($\xi_{li,a0}$) and backscatter intercept ($\xi_{li,b0}$). The local inhomogeneity is still high with respect to the other types of inhomogeneities for both attenuation slope ($\xi_{li,a1}$) and backscatter intercept ($\xi_{li,b1}$). The global inhomogeneity (ξ_{gi}) is much lower than the local inhomogeneity, and becomes nearly negligible for the slope values (a_1,b_1).

The inhomogeneity due to diffraction correction (ξ_{dc}) varies with the type of TC. It is clear that the average liver type TC results in the lowest (ξ_{dc}) values. Both the backscatter features do not have significant inhomogeneity (1 is included in the interval), and both the attenuation features are nearly negligible. There is no difference between the leave-one-out (LOO) TC estimate and re-substitution TC estimate. This indicates that the average liver TC predicts diffraction well in unseen livers.

Finally, the remaining inhomogeneity was estimated. The whole dataset (all livers, all sizes, all depths) was normalized by subtracting the global average value, and subsequently dividing by the sd which was obtained by multiplying the theoretical values with the estimated inhomogeneity factors and the beam overlap factor. The resulting inhomogeneity observed in all measurements is not significant. Thus, again the sd model comprising the theoretical sd estimate times the various factors describes the data very well.

Instead of looking at it quantitatively, Fig. 2.8 gives a qualitative view on the depth-dependent diffraction filter effect. Five sets of average features are plotted versus depth, from five types of

Normal *in vivo* liver inhomogeneity estimates					
TC	type	a0	a1	b0	b1
foam	li	4.62 (4.41-4.83)	1.63 (1.55- 1.70)	8.01 (7.64-8.37)	2.32 (2.22-2.43)
	gi	1.31 (1.25-1.36)	1.05 (1.01- 1.10)	1.27 (1.21-1.32)	1.05 (1.01-1.10)
	dc	1.69 (1.62-1.76)	1.38 (1.32- 1.43)	1.71 (1.64-1.78)	1.46 (1.40-1.52)
	mo	1.00 (0.96-1.05)	1.01 (0.96- 1.05)	1.00 (0.96-1.04)	1.00 (0.96-1.04)
liver	li	4.61 (4.40-4.82)	1.61 (1.54- 1.69)	7.92 (7.56-8.28)	2.29 (2.18-2.39)
	gi	1.31 (1.26-1.37)	1.06 (1.01- 1.10)	1.27 (1.21-1.32)	1.06 (1.01-1.10)
	dc	1.06 (1.01-1.10)	1.06 (1.02- 1.11)	1.02 (0.97-1.06)	1.02 (0.98-1.06)
	mo	1.00 (0.96-1.04)	1.00 (0.96- 1.04)	1.00 (0.96-1.04)	1.00 (0.96-1.04)
rubber	li	4.63 (4.42-4.84)	1.63 (1.55- 1.70)	7.98 (7.61-8.34)	2.32 (2.21-2.42)
	gi	1.31 (1.25-1.36)	1.05 (1.01- 1.10)	1.26 (1.21-1.32)	1.05 (1.01-1.10)
	dc	1.63 (1.56-1.70)	1.10 (1.05- 1.14)	1.67 (1.60-1.75)	1.11 (1.06-1.16)
	mo	1.00 (0.96-1.05)	1.00 (0.96- 1.04)	1.00 (0.96-1.04)	1.00 (0.96-1.04)
none	li	4.59 (4.38-4.80)	1.61 (1.53- 1.68)	7.91 (7.55-8.28)	2.27 (2.17-2.37)
	gi	1.31 (1.26-1.37)	1.05 (1.01- 1.10)	1.27 (1.21-1.32)	1.05 (1.01-1.10)
	dc	1.78 (1.70-1.85)	1.17 (1.12- 1.22)	1.58 (1.51-1.65)	1.23 (1.17-1.28)
	mo	1.00 (0.96-1.04)	1.00 (0.96- 1.04)	1.00 (0.96-1.04)	1.00 (0.96-1.04)
liver	li	4.61 (4.40-4.82)	1.61 (1.54- 1.69)	7.92 (7.56-8.28)	2.28 (2.18-2.39)
loo	gi	1.36 (1.30-1.42)	1.06 (1.02- 1.11)	1.31 (1.25-1.36)	1.07 (1.02-1.11)
	dc	1.05 (1.01-1.10)	1.07 (1.02- 1.11)	1.02 (0.97-1.06)	1.02 (0.98-1.07)
	mo	1.00 (0.96-1.04)	1.00 (0.96- 1.04)	1.00 (0.96-1.04)	1.00 (0.96-1.04)

Table 2.2 Inhomogeneity factors for normal *in vivo* liver data using various diffraction correction methods. Mnemonics: li is local inhomogeneity, gi global inhomogeneity, dc is diffraction correction, and mo is model.

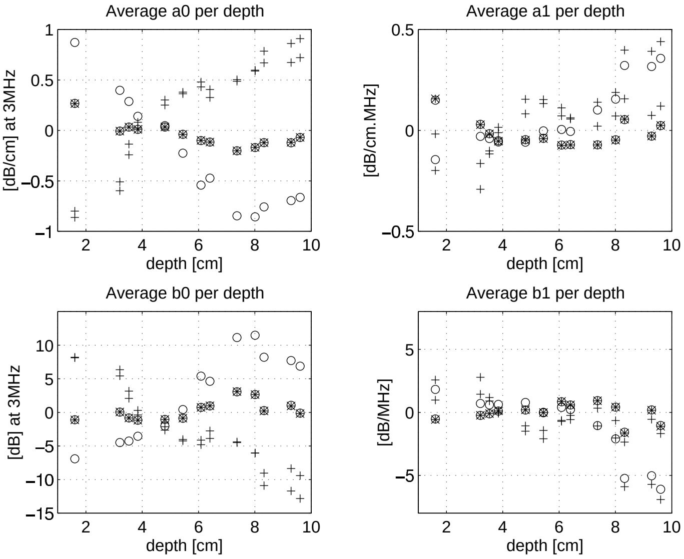

Figure 2.8 In vivo liver, average acousto-spectrographic features measured in regions-of-interest at various depths. Three TCs were used, calibrated on: foam or rubber (+), liver (⊗, resubstitution and leave one out), flat spectrogram, i.e., no diffraction correction (o).

TC corrections. To compare the sets of features, the mean values in each set were subtracted. It is clearly seen that the liver TC results in the smallest depth-dependency effect. Both rubber and foam result in the same type of errors.

2.7 Discussion

It was shown in this chapter that the sd's of four *in vivo* measured acousto-spectrographic features are predicted very well. The predicted sd comprises: a theoretical part based on a homogeneous tissue model with Rayleigh-distributed backscattered amplitudes, and a practical part with various factors that account for deviations from the model.

Throughout this study, important concepts have emerged, which will be summarized next by following the processing steps.

For the feature extraction methods to be clinically applicable, it is essential to acquire accurately radio-frequency (RF) signals from standard clinical systems. These systems should have operator-independent RF signals available. A system was used with a custom-built RF interface to avoid operator-dependent gain and or TGC settings in the RF signal. Furthermore, an acquisition workstation must be available that can acquire these high frequency signals over the wide dynamic range, related to the attenuation in the signals. The 8-bit 50 MHz acquisition system workstation with a reproducible TGC amplifier (Verhoeven and Thijssen, 1992) in combination

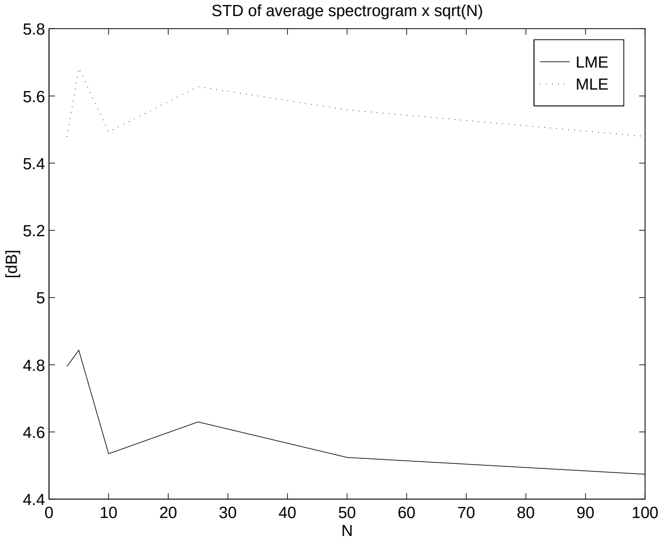

Figure 2.9 Log mean (LME) versus mean of log (MLE) spectrogram calculation. The average was taken over 5000 samples. The result was multiplied by the square root of N. N was varied from 3 to 100.

with the RF interface thus forms a firm basis for the feature extraction methods.

The next step to get robust features is to build in a strategy to account for *in vivo* measurement conditions. A mask matrix was applied that is used to store manually- and automatically-detected areas such as blood-vessels, ligaments, and over- and underflow of the digitizer. When calculating the average spectrogram, windows that contain any marked samples are left out of the analysis, as these windows could influence features. The methods were verified by visual inspection, which revealed that all visible structures were properly detected. The detection threshold was set such that it is biased towards detection, which assures that the remaining area is without these structures. Only ROIs were selected with less than 5% masked area.

The number 5.57 dB cited in literature when calculating the expected sd of the log mean average spectrogram (Kuc and Schwartz, 1979; Berger et al., 1987), pertains to calculating the mean of the logarithm of Rayleigh-distributed variables. The log of the mean was calculated and 4.54 dB (Eq. 2.12) was found. Figure 2.9 shows the results of simulations while using both calculation strategies, where sd's are multiplied by $\sqrt{N}$. The figure clearly shows that the two methods do not produce the same results. It can be concluded that the log of the mean results in better precision than the mean of the log when calculating the log average spectrogram.

A consistent combined analytic derivation of the sd of all four features (Eqns. 2.21, 2.22, 2.23, 2.24) has not yet been described in literature. The sd of the attenuation slope (fit through zero, i.e., $a(f) = a_1.f$) was analytically derived by Kuc (1985), Parker (1986), and Berger et al. (1987). A two parameter model (i.e., $a(f) = a_0 + a_1(f - f_c)$) with less approximations, and the log mean spectrogram was applied. Simulations show that the equations predict the sd of the features measured from signals generated according to the signal model very well over large depth and frequency ranges. As has been recognized by Parker (1986), longer ROIs enable to estimate attenuation more accurately than wider ROIs, because averaging adjacent scan lines reduces the sd by only the square root of the number of lines, whereas the sd reduces by a power 3/2 of the ROI length. The backscatter feature sd, however, is reduced equally by both increasing the number of lines as well as increasing the ROI depth. The equations show that the sd's are independent of the absolute attenuation value, as was also noticed by Parker (1986); this is extended by recognizing that they are also independent of the absolute backscatter value.

An intermediate step in the methods is the calculation of the spectrogram from the RF signal. These calculations require that the length, degree of overlap, and type of windowing function be chosen in advance. It was shown that the rectangular window produces near theoretical sd's, and that a Hanning and rectangular window have equal performance when overlapping the windows by 50%. Furthermore, simulated results show that sd and bias are not sensitive to modest variations in window size and overlap. For all windows, over a wide range of window sizes and overlap, the bias on the features is very low. The latter two observations thus alleviate careful tuning strategies of the three settings.

So far, results were shown on simulated data; when introducing the transducer with its typical characteristics (TC) on the received backscatter spectrum, a correction has to be performed. Two strategies were applied to measure the TC. From the results, it is concluded that TC correction varies with the type of medium as was also noticed by Robinson et al. (1984). The effect of TC correction on features measured on *in vivo* liver data is very small only when TC is calibrated with *in vivo* liver data. It is stressed that the features are measured on unseen liver data in the calibration (as observed in the leave-one-out experiment). Foam, rubber phantoms, as well as no TC correction, all show significant influence of TC on feature estimates in the liver.

Two types of inhomogeneity were measured that quantify fluctuations of underlying physical parameters: local (within an organ), and global (between organs, or inter-subject) inhomogeneity. It was surprising to know that even rather homogeneous phantom material shows significant local inhomogeneity. The results for *in vivo* data show that local inhomogeneity is the major factor in increasing sd estimates with respect to theory. The increase due to global variations is much smaller. Therefore any research in improving results on feature extraction should focus on the local inhomogeneity.

Appendix A Derivation of Eqns. 2.13 and 2.14

In this appendix, Eqns. 2.13 and 2.14 are derived. Given a set of measurements (y_i, x_i) which were generated by a linear model:

$$\boldsymbol{y} = ax + b + \boldsymbol{\epsilon} \tag{2.27}$$

If ϵ is an independent, zero mean, additive, and Gaussian-distributed stochastic variable $N(0,\sigma)$, then the variance in the estimated slope and intercept is (Kleinbaum et al., 1988):

$$\sigma_a^2 = \frac{\sigma^2}{\sum_{i=1}^{N}(x_i-\overline{x})^2} \tag{2.28}$$

$$\sigma_b^2 = \frac{\sigma^2\sum_{i=1}^{N}x_i^2}{N\sum_{i=1}^{N}(x_i-\overline{x})^2} \tag{2.29}$$

In the current application, the x_i are sampled at equidistant intervals ($x_{i+1}-x_i=\Delta x$), which enables the summations to be developed into simple expressions. Eq. 2.28 becomes:

$$\sigma_a^2 = \frac{12\sigma^2}{\Delta x^2(N^3-N)}, \tag{2.30}$$

which is equivalent to the result by Berger et al. (1987, eqn.5).
For the development of Eq. 2.29, an extra term is introduced, $M=x_1/\Delta x$, which is the number of intervals delay from 0 to x_1. Eq. 2.29 then becomes:

$$\sigma_b^2 = \frac{2\sigma^2N(2N^2+6NM+6M^2-3N-6M+1)}{N(N^3-N)} \tag{2.31}$$

It should be noticed that Eqns. 2.30, and 2.31 are exact expressions of Eqns. 2.28 and 2.29. They are more accurate than the approximations at this stage by Parker (1986, Eq. 22), and Yao (1991, Eq. 12).
Eqns. 2.30, and 2.31 can be approximated if it is assumed that $N>2$. Then ($N^3-N\approx N^3$) and $(2N^2+6NM+6M^2-3N-6M+1)\approx(2N^2+6NM+6M^2-3N-6M)$. Substituting the total length of a ROI, $D=\Delta xN$, and the relative delay $\delta=M/N$ results in the following approximations of Eqns. 2.30, and 2.31:

$$\sigma_a^2 \approx \frac{12\sigma^2}{D^2N} \tag{2.32}$$

$$\sigma_b^2 \approx \frac{4\sigma^2(1+3\delta+3\delta^2-\frac{3+6\delta}{2N})}{N} \tag{2.33}$$

Comparing Eqns. 2.7, and 2.27 it is seen that the attenuation equals $a/2$, thus Eq. 2.32 should be divided by 4. The square root then results in Eqns. 2.13 and 2.14.

Appendix B Estimating inhomogeneities

A factor, ξ, estimates the increase in estimated sd, $\hat{\sigma}$, relative to the expected sd, σ, due to variations in an accompanying setting Ξ, thus $\hat{\sigma}=\xi\sigma$. For example, the factor due to incorrect TC correction is 1 if the depth is fixed. In this single factor model, ξ is simply estimated by calculating $\hat{\sigma}$ from the whole dataset, and divide it by σ, which is calculated from theory. For

the acoustical feature sd's this is not possible, because the setting Ξ also influences the expected sd, thus: $\hat{\sigma}(\Xi) = \xi\sigma(\Xi)$. As an example, consider ROI features calculated at different depths, as shown in theory, the expected sd varies with depth.
To explain how the factor can then be calculated, let us assume that an acoustic feature $\boldsymbol{x}$ is a stochastic variable with the following probability density function (pdf) with sd dependent on factor Ξ:

$$p_1(x(\Xi)) = N(\overline{x}, \xi\sigma(\Xi)) \tag{2.34}$$

The normality assumption ($N(.,.)$) was already shown in the subsection sd of the Attenuation and Backscatter Slope and Intercept. The average of the feature is constant ($\overline{x}$) and should not depend on $|Xi$ (at least, that is the hypothesis). Transforming the feature (x') by subtracting the mean (calculated over the whole dataset) and then dividing it by the expected sd results in a new stochastic variable with the following pdf:

$$p_2(x') = p_2\left(\frac{x(\Xi) - \overline{x}}{\sigma(\Xi)}\right) = N(0, \xi) \tag{2.35}$$

The factor ξ is now simply estimated by calculating the sd from the transformed variable ($\hat{\xi} = \sigma_{x'}$).
Instead of one, three factors have to be estimated. Then, a single factor is estimated by calculating the average while keeping the other factors constant, e.g., using $\overline{x}(\Xi_1, \Xi_3)$ estimates ξ_2.

Bibliography

Akita M, Ueda M. The effect of windowing on spectral estimation of echoes scattered by random medium. J Acoust Soc Am 1988;83:1243–1248.

Berger G, Laugier P, Fink M, Perrin J. Optimal precision in ultrasound attenuation estimation and application to the detection of duchenne muscular dystrophy carriers. Ultrason Imag 1987;9:1–17.

Berkhoff AP, Thijssen JM, Homan RJF. Simulation of ultrasonic imaging with linear arrays in causal absorptive media. Ultrasound Med Biol 1996;22:245–259.

Burckhardt CB. Speckle in ultrasound B-mode scans. IEEE Trans Sonics Ultras 1978;25:1–6.

Céspedes I, Ophir J. Diffraction correction methods for pulse-echo acoustic attenuation estimation. Ultrasound Med Biol 1990;16:707–717.

Cloostermans MJTM, Thijssen JM. A beam corrected estimation of the frequency dependent attenuation of biological tissues from backscattered ultrasound. Ultrason Imag 1983;5:136–147.

Fink M, Cardoso JF. Diffraction effects in tissue characterization. In: AIUM Congress. 1983: 180–180.

Goodman JW. Statistical properties of laser speckle patterns. Berlin: Springer-Verlag, 1975: 9–75.

Insana MF, Hall TJ, Cook LT. Backscatter coefficient estimation using array transducers. IEEE Trans Ultrason Ferroelectr Freq Control 1994;41:714–723.

Insana MF, Zagzebski JA, Madsen EL. Improvements in the spectral difference method for measuring ultrasonic attenuation. Ultrason Imag 1983;5:331–345.

Jongen HAH, Thijssen JM, Aarssen M, Verhoef WA. A general model for the absorption of ultrasound by biological tissues and experimental verification. J Acoust Soc Am 1986;79:535–540.

Kleinbaum DG, Kupper LL, Muller KE. Applied regression analysis and other multivariate methods. Boston, USA: PWS-Kent, 1988.

Kuc R. Parameteric estimation of the acoustic attenuation coefficient slope for soft tissue. In: IEEE Ultras. Symp. Proc.. 1976: 44–47.

Kuc R. Bounds on estimating the acoustic attenuation of small tissue regions from reflected ultrasound. Proceeding of the IEEE 1985;73:1159–1168.

Kuc R, Schwartz M. Estimating the acoustic attenuation coefficient slope for liver from reflected ultrasound signals. IEEE Trans Sonics Ultras 1979;26:353–362.

Kuc R, Taylor KJW. Variation of acoustic attenuation coefficient slope estimates for *in-vivo* liver. Ultrasound Med Biol 1982;8:403–412.

Laugier P, Berger G, Fink M, Perrin J. Diffraction correction for focussed transducers in attenuation measurements *in-vivo*. Ultrason Imag 1987;9:248–259.

Lizzi FL, Greenebaum M, Feleppa EJ, Elbaum M. Theoretical framework for spectrum analysis in ultrasonic tissue characterization. J Acoust Soc Am 1983;73:1366–1373.

Lizzi FL, Katz L, Coleman DJ. Applications of spectral analysis in medical ultrasonography. Ultrasonics 1976;pp. 77–80.

Lizzi FL, Ostromogilsky M, Feleppa EJ, Rorke MC, Yaremko MM. Relationship of ultrasonic spectral parameters to features of tissue microstructure. IEEE Trans Ultrason Ferroelectr Freq Control 1987;33:319–329.

Madsen EL, Insana MF, Zagzebski JA. Method of data reduction for accurate determination of acoustic backscatter coefficients. J Acoust Soc Am 1984;76:913–923.

Mountford RA, Wells PNT. Ultrasonic liver scanning: the quantitative analysis of the normal a-scan. Physics Med Biol 1972;17:14–25.

Nicholas D, Hill CR, Nassiri DK. Evaluation of backscattering coefficients for excised human tissues: principles and techniques. Ultrasound Med Biol 1982;8:7–15.

O'Donnell M. Effects of diffraction on measurements of the frequency-dependent ultrasonic attenuation. IEEE Trans Biomed Eng 1983;30:320–325.

Oosterveld BJ, Thijssen JM, Hartman PC, Romijn RL, Rosenbusch GJE. Ultrasound attenuation and texture analysis of diffuse liver disease: methods and preliminary results. Physics Med Biol 1991;36:1039–1064.

Papoulis A. Probability, random variables, and stochastic processes. Singapore: McGraw-Hill, 1991.

Parker KJ. Attenuation measurement uncertainties caused by speckle statistics. J Acoust Soc Am 1986;80:727–734.

Pauly H, Schwan P. Mechanism of absorption of ultrasound in liver tissues. J Acoust Soc Am 1971;2:692–699.

Robinson DE, Wilson LS, Bianchi T. Beam pattern (diffraction) correction for ultrasonic attenuation measurements. Ultrason Imag 1984;6:292–303.

Romijn RL, Thijssen JM, Beuningen GWJ. Estimation of scatterer size from backscattered ultrasound: a simulation study. IEEE Trans Ultrason Ferroelectr Freq Control 1989;36:593–606.

Ueda M, Ozawa Y. Spectral analysis of echoes for backscattering coefficient measurement. J Acoust Soc Am 1985;77:38–47.

Verhoef WA, Cloostermans MJTM, Thijssen JM. Diffraction and dispersion effects on the estimation of ultrasound attenuation and velocity in biological tissues. IEEE Trans Biomed Eng 1985;32:521–529.

Verhoeven JTM, Thijssen JM. A software controllable time-gain compensation amplifier board for VMEbus systems. Ultrasonics 1992;40:407–408.

Wagner RF, Smith SW, Sandrik JM, Lopez H. Statistics of speckle in ultrasound B-scans. IEEE Trans Sonics Ultras 1983;30:156–163.

Welch PD. The use of fast fourier tranform for the estimation of power spectra: a method based on time averaging over short, modified periodograms. IEEE Trans Audio Electr Acoust 1967;15:70–73.

Yao LX, Zagzebski JA, Madsen EL. Statistical uncertainty in ultrasonic backscatter and attenuation coefficients determined with a reference phantom. Ultrasound Med Biol 1991;17:187–194.

Chapter 3

Quantitative ultrasonic analysis of liver metastases

3.1 Introduction

Contemporary[1] (B-mode) ultrasound (US) has various applications in the diagnosis of metastases. US can be used to screen the liver for metastases, although bolus-enhanced CT is often the imaging technique of choice (Ferrucci, 1990; Wernecke et al., 1991). However, using CT, small cysts may be mistakenly diagnosed as metastases. The true nature of these lesions can be established by ultrasound (Brick et al., 1987). US can also be used to evaluate the response to chemotherapy of metastases, but literature on this subject is marked by controversy.

US may be improved by ultrasonic tissue characterization (UTC) techniques. UTC can successfully assist in the quantification of diffuse liver pathology *in vivo* (Raeth et al., 1985; Garra et al., 1987; Parker et al., 1988; Garra et al., 1989; Oosterveld et al., 1991). With respect to follow-up, some UTC features relate to intra-ocular malignant melanoma response by cobalt-60 plaque (Coleman et al., 1985). Several UTC features can discriminate metastases from healthy liver parenchyma in *in vivo* conditions (Bamber and Hill, 1981; Cloostermans et al., 1986). Two *in vivo* studies on metastases have been reported in literature (King et al., 1985; O'Donnell and Reilly, 1985). These authors concluded from a relatively small number of metastases that UTC can be useful.

The application of UTC to the analysis of metastases remains difficult because of three reasons.

Firstly, UTC techniques have been developed assuming a single, homogeneous tissue model. Yet, the US appearance of metastases varies noticeably with the type of primary tumor (Scheible et al., 1977; Rettenmaier, 1990). Moreover, a metastasis of a given primary tumor can have different appearances related to its development stage and reaction to therapy. Initially, metastases from a primary adenocarcinoma of the colon appear mostly as small hypo-echoic lesions. Older metastases develop an increasingly echogenic core, which may become hyper-echoic in due time,

---

[1] This chapter is based on the publication: Huisman H.J., Thijssen J.M., Wagener, D.J.Th., Rosenbusch,G.J.E. *Quantitative ultrasonic analysis of liver metastases* Ultras.Med.Biol., in press.

and forms the so-called bull's eye. The hypo-echoic rim, or halo, is a typical sign of malignant, progressive metastases. An effective therapy can reduce the halo, and at the same time calcifications may develop within the core. Very large, and (presumably) old tumors may even develop a liquefied, necrotic area within the core. Lesions at various stages may occur in a single liver, because the primary tumor may have given rise to metastases at different time intervals. It is clear that a metastases model will have to be incorporated.

Secondly, the correlation between histology and echogenic appearance is unclear. No correlation was found between tumor cell type and echogenic appearance (Marchal et al., 1985b). Tumor vascularity seems to be a main cause of the echogenic appearance of liver metastases; reflectivity is probably less related to the walls of the tumoral vessels than to the abundance of blood/solid tissue interfaces (Marchal et al., 1985a). Furthermore, it is not clear in literature whether the halo is part of the tumor or not. According to Marchal et al. (1985b) the halo is extra-tumoral and caused by peritumoral liver cell compression, whereas Wernecke et al. (1992a) concluded that the halo is predominantly a zone of proliferating tumor cells in the periphery of the lesion. Sherar et al. (1987) imaged spheriods using a backscatter microscope (100MHz) and found a hypo-echoic halo that correlated with viable cell mass. They postulated that the hypo-echogenicity is probably due to small acoustic impedance variations in the halo cell mass. Whatever the nature of the halo, Wernecke et al. (1992b) showed that the halo can distinguish benign from malignant tumors.

Thirdly, *in vivo* UTC of focal lesions in the liver requires the estimation of features in small windows. Small windows result in low precision estimates, (see for example Chapter 2), and consequently UTC features estimated in such windows are less discriminative. Furthermore, accurate *in vivo* analysis requires an adequate correction for the intervening tissue between transducer and window. To cope with these problems accurate UTC feature estimation methods have been developed (see chapter 2). In this chapter these methods are applied to a large set of *in vivo* acquisitions of metastases and the aim is to find characteristic UTC features that can help: detect metastases in liver parenchyma when displayed in a new, parametric image; discriminate benign from malignant metastases; or study the follow-up of metastases.

3.2 Materials

3.2.1 Subjects

Ultrasound examinations were recorded from 103 patients of the Department of Medical Oncology of the University Hospital Nijmegen with presumed metastatic liver involvement over a period of 4 years. A selection of 12 patients was made using the following criteria:

- radiologically and histologically confirmed primary adenocarcinoma in the colon. These tumors produce metastases in the liver that are often well localized and sufficiently large to let the UTC feature estimation algorithms operate.
- metastases could be outlined unequivocally,
- several sessions of recordings of the same patient were available, to enable follow-up study.

In all cases informed consent was obtained. Patient ages ranged from 46–75 years. For verification and calibration purposes acquisitions were obtained from 12 healthy volunteers. All patients were instructed to refrain from eating and drinking several hours before the examination (all showed full gallbladders) which is standard protocol and prevents effects due to circadian rhythm (Hartman et al., 1991).

3.2.2 Acquisition

The examinations were carried out with a Toshiba-T270A scanner using a 3.75 MHz phased array transducer (PSF37-CT) in single focus mode (F=7.5 cm). A custom-built interface in the scanner gave access to radio-frequency (rf) echo lines which were digitized over the full depth-range (0-15cm) at 15 MHz and 110 line (a full sector) acquisitions were digitized and stored in an ultrasonic workstation (Verhoeven, 1994) (see also Chapter 2).

Each liver was examined at the Department of Radiology by an experienced sonographer. Several acquisitions (8–16) of different sections of the liver were made intra- or sub-costally while the subject was in the supine position. All persons were examined while having fasted for a few hours (i.e. showing filled gall bladder).

3.2.3 Manual segmentation

Scan-conversion (Berkhoff et al., 1994), to convert the polar grid sector image into a rectangular grid B-mode image, and contour drawing software on the workstation were used to outline the liver, non-parenchyma tissue (e.g. blood-vessels and artifacts) and metastases, the remaining area was labeled parenchyma. The segmentation resulted in a mask matrix that was used by the UTC methods to restrict feature estimation to selected regions.

The author manually segmented 218 metastases in the patient group and had the outline of each metastasis confirmed by an experienced sonographer from the Department of Radiology. Furthermore, the parenchyma was segmented in 128 acquisitions in the volunteer group for calibration purposes. In the acquisitions of two volunteers, 44 dummy metastases were manually outlined at random locations in the liver such that only normal liver parenchyma was present in each dummy region. The sizes of the dummy regions were comparable to that in the real metastasis group.

3.3 Methods

3.3.1 Automatic halo segmentation

Several metastases showed a distinctive halo, therefore it was decided to analyze the halo and core tissue separately. However, manual segmentation is prone to large inter-observer variations as there exists no sharp demarcation between halo and core tissue (see Fig. 3.1a and c). Thus, an objective and robust segmentation method was developed to segment the halo. The method assumed that the outline of a metastasis is available from the manual segmentation step and that it comprises either: core tissue surrounded by a hypo-echoic halo, or one single tissue type. First, using simple, binary erosion techniques (Gonzalez and Wintz, 1987) an outer rim of 1.5 speckles thickness[2] was segmented ($S_o(1.5)$). This outer rim prevented manual segmentation errors in the outline to interfere noticeably with the subsequent steps. Next, in the same manner, a set of halo pixels ($S_h(d)$) was segmented, where d is the thickness of the halo. The minimum halo thickness was 3 [speckles] and could be incremented in multiples of 1.5 [speckles]. The remaining, central area in the metastasis then represents the core set $S_c(d)$. Let S_{tot} be the total set of metastasis pixels, then $S_{\text{tot}} = S_o(1.5) \cup S_h(d) \cup S_c(d)$. The estimated halo thickness d maximizes the ratio of the average gray value of core and halo pixels:

$$\eta_{\max} = \max_d \left(\frac{\langle e(i) \rangle_{i \in S_c(d)}}{\langle e(j) \rangle_{j \in S_h(d)}} \right), \tag{3.1}$$

where i, and j are 2D pixel coordinates in the B-mode image e, and $\langle \ldots \rangle$ is the averaging operator. If $\eta_{\max} > 1.1$, the accompanying segmentation gave the halo and core areas (see Fig. 3.1b and d), else the halo and core regions were merged into one region. At this threshold a detected halo and the visually observed halo in the patient material correlated well, whereas the algorithm only detected 3 halos out of 44 dummy metastases in the two volunteers. Other algorithms were extensively tested, but none was robust enough to tackle the segmentation problem in these type of images.

3.3.2 UTC feature estimation

Acousto-spectrographic features

Four acousto-spectrographic features: a_0, a_1, b_0, b_1 were estimated. The estimation technique is briefly summarized, detailed descriptions and references can be found in Chapter 2. The received ultrasonic rf signal at a steering angle θ (the full sector is divided into 110 angles) is denoted by $e_\theta(t)$. The spectrogram or periodogram (Oppenheim and Schafer, 1975) $E_\theta(f,z)$ (128pt uniform window, 50% overlap) at each angle was calculated and the parts that were within the estimation area (using the mask matrix) were used to calculate the average spectrogram, where the average was over the steering angle $\overline{E}(f,z) = \langle E_\theta(f,z) \rangle_\theta$. A linear signal model was assumed, that allowed to remove the transducer dependencies obtained in a separate calibration step. The resulting tissue-dependent part, $\overline{E}'(f,z)$, was then used to estimate the attenuation $a(f)$ [dB/cm] by taking the derivative with respect to z of the log-transform ($d\left\{log_{10}E'(f,z)\right\}/2dz$). Attenuation correction and log-transform then left the backscatter coefficient $b(f)$ [dB]. A linear model for both coefficients was also assumed: $a(f) = a_0 + a_1(f - f_c)$, and $b(f) = b_0 + b_1(f - f_c)$, where f_c is the central frequency. Note that a_0, b_0 are intercepts at central frequency.

In a separate calibration step, the transducer dependent term was estimated by the average spectrogram of the 128 segmented parenchymal regions in the normal *in vivo* liver acquisitions. This method results in optimal removal of transducer dependencies, and for liver examinations, it automatically includes an average abdominal wall correction (see also Chapter2). Using this calibration method attenuation and backscatter features are implicitly calculated relative to average normal parenchyma (ANP). Consequently, in this chapter, the features a_0, a_1, b_0, b_1 will on average be zero when estimated in normal livers.

---

[2] Speckle thickness is defined as the correlation cell size (Wagner et al., 1983) in the lateral and axial direction

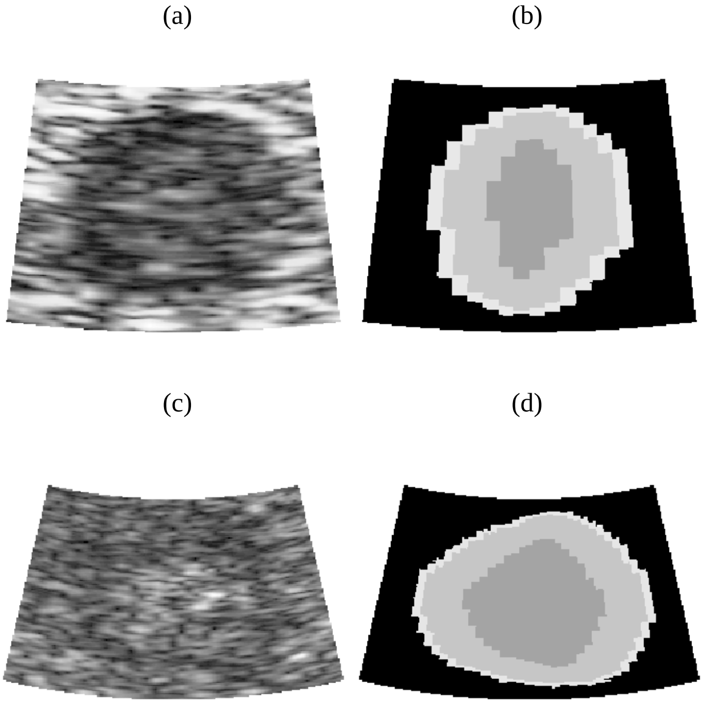

Figure 3.1 Metastasis with halo (a,c) and the result of the automatic segmentation algorithm (b,d). The black segment is outside the metastasis, the light gray outer rim is undefined edge area, the next darker gray rim is the detected halo, and the darkest gray central area is the detected core of the metastasis.

For the attenuation measurements, a metastasis was required to be on average at least 1.8cm in depth (i.e. in the axial direction) and to contain no obvious inhomogeneities. Previous experiments showed that using smaller metastases resulted in a standard deviation that exceeded a reasonable limit for acceptability (e.g. $>$ maximum attenuation deviation due to pathology). The effective size is even smaller, as metastases boundaries most often are irregular and do not coincide with the spectrogram window boundaries. Furthermore, the estimated attenuation was rather sensitive to inhomogeneities in the metastasis tissue. For example, a few calcifications in the deeper part of the metastasis could cause the method to falsely predict low attenuation.

In practice, the attenuation correction comprises two parts. The first part is the attenuation inside the metastasis, and second is the attenuation in between transducer and estimation region. However, the average attenuation in the liver of the subject was used in both parts. In doing so, a far higher precision (but only slightly lower accuracy) attenuation estimate was used, which results in an increased precision of the estimated backscatter coefficient.

metastasis type	mnemonic	$b_0 - b_{0,\mathrm{par}}$
homogeneous hypo-echoic	hypo	$\leq$-3dB
heterogeneous	halo	$\leq$-3dB
	core	-
homogeneous hyper-echoic	hyper	$\geq$0dB

Table 3.1 The three metastases categories used in this chapter, categorized by using the estimated relative backscatter intercept

The features b_0, b_1 summarize the backscatter coefficient relative to the average normal parenchyma (ANP). This will be referred to as the normalized backscatter. Analogous to visual assessment, the backscatter was also calculated relative to the backscatter of the surrounding parenchyma $b_{0,\mathrm{par}}, b_{1,\mathrm{par}}$. This is referred to as relative backscatter, $(b_0 - b_{0,\mathrm{par}}), (b_1 - b_{1,\mathrm{par}})$. In small lesions, the high variance resulted in large fluctuations (especially of b_1), therefore, the backscatter was calculated only in regions with an area larger than 0.5cm^2. Table 3.1 summarizes the three types of metastases that were categorized using the relative backscatter intercept. Note that the core type tissue was detected because of the presence of its surrounding halo.

Texture features

The texture feature SNR, e.g. (Verhoeven and Thijssen, 1991), was calculated, because it is a well-known UTC feature that *in theory* relates to scatterer density (Oosterveld et al., 1985). The feature SNR is defined as the mean divided by the standard deviation of the gray values[3] within a region. A second feature, $\langle snr \rangle$ was implemented, which was calculated as follows. The total lesion area was partitioned into small areas of equal shape and size. In each of these small areas the SNR was calculated. The ensemble average of all SNR values results in the feature value of $\langle snr \rangle$.

3.3.3 Minimum probability region

In the next section multiple scatter plots will be shown of two features to establish which features are discriminative. To help visualize the data structure, these scatterplots are also summarized in a second plot, in which each point cloud from the scatter plot (e.g. a point cloud of halo region values) is replaced by the minimum probability region of a bi-variate normal distribution. This minimum probability region is bounded by the iso-probability contour defined by:

$$(x - \overline{x})^T S^{-1} (x - \overline{x}) = 1, \tag{3.2}$$

where x is the vector of two features (e.g. (b_0, b_1)), $\overline{x}$ is the average vector, and S is the covariance. The latter two are estimated from the points in the cloud.

---

[3] The gray values are obtained from the envelope of the transducer dependency and attenuation corrected rf signal.

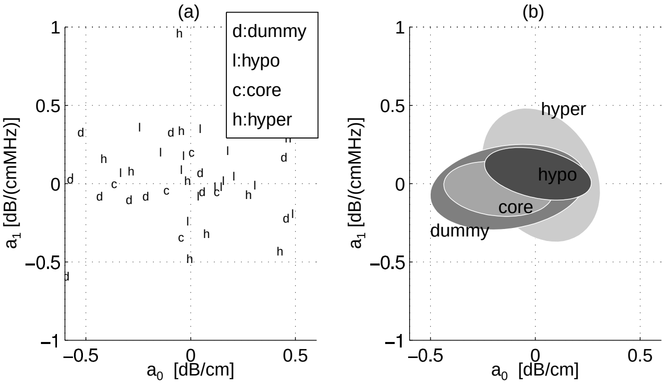

Figure 3.2 Scatter plot of attenuation features (a) and accompanying bi-variate minimum probability plots (b).

3.4 Results

3.4.1 Attenuation

A reliable estimate of the attenuation features a_0 and a_1 was obtained in 32 out of 218 metastases (15%). The halo region was too small in all cases. Fig. 3.2a shows a scatter plot of the estimated attenuation feature values. The attenuation features in all metastasis tissue types were not different from zero (recall that acousto-spectrographic features were estimated relative to ANP) which means that they were not different from attenuation in normal liver parenchyma, which was confirmed by the attenuation feature values in the dummy metastases (Fig. 3.2b).

3.4.2 Backscatter

The backscatter features could be estimated in all types of metastases. Figs. 3.3a and c show scatter plots of (b_0, b_1)-pairs. Looking at the relative backscatter, the dashed vertical lines in Fig. 3.3c indicate the metastases category boundaries (see Table 3.1). Although $(b_0 - b_{0,\mathrm{par}})$ is an established discriminative feature, this cannot be concluded from this figure, because the variable was used to categorize the metastases. The figure does show that the core tissue appeared to be hypo-echoic, which is not obvious as the core was only detected because of the presence of a darker halo (Eq. 3.1, r>1.1). More interestingly, the $(b_1 - b_{1,\mathrm{par}})$-values were clearly increased (>0) in the halo and hypo-echoic metastases. This was also true when comparing halo and core tissue. Thus b_1 is an additional UTC feature that helps to discriminate the halo and hypo type metastases from the parenchyma, but also the halo from the core. Relative estimation requires a preprocessing step that first estimates the parenchyma backscatter. It would be more convenient if the features b_0 and b_1 can be used directly, because they do not require an estimate of the surrounding parenchymal backscatter. Figs. 3.3a and b show the results: the clouds become larger.

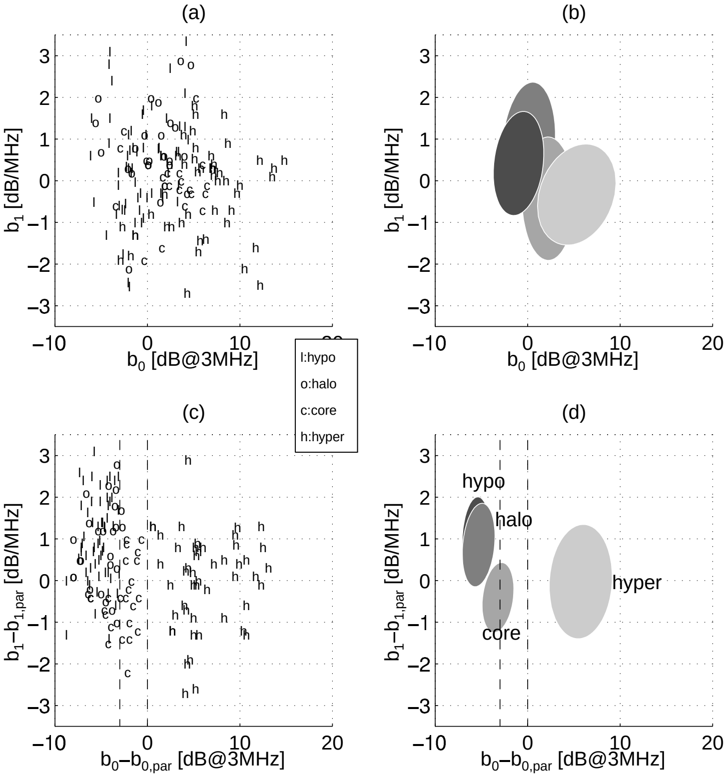

Figure 3.3 Scatter plots of backscatter features. Subplots a) and b) show the normalized backscatter, whereas c) and d) show the relative backscatter. The vertical dashed lines indicate the boundaries (see Table 3.1) used to categorize halo, hypo, and hyper type metastases.

The normalized backscatter features were far less discriminative than the relative backscatter features.

The normalized and relative measurements are compared in Figs. 3.4a and c. In hyper type (symbol 'x') metastases, $(b_0 - b_{0,\mathrm{par}})$ correlated very well with b_0. However, hypo type metastases and halos (symbol: 'o') appeared not to be specifically hypo-echoic for the normalized backscatter. To understand this the surrounding parenchyma need to be considered. In Fig. 3.4b $(b_0 - b_{0,\mathrm{par}})$ is plotted versus $b_{0,\mathrm{par}}$ and it shows that in the dataset the hypo-echoic metastases were mainly found in hyper-echoic parenchyma. Thus, the metastases in these livers were actually visible because of the increased echogenicity of the surrounding parenchyma. On the other hand, the relative and normalized backscatter slope, $(b_1 - b_{1,\mathrm{par}})$ and b_1, correlated well (Fig. 3.4c). The backscatter slope in the parenchyma, $b_{1,\mathrm{par}}$, did not correlate with the backscatter slope in metastases (Fig. 3.4d), which means that the increased backscatter slope is a phenomenon not only relative to the surrounding parenchyma, but also relative to normal liver parenchyma.

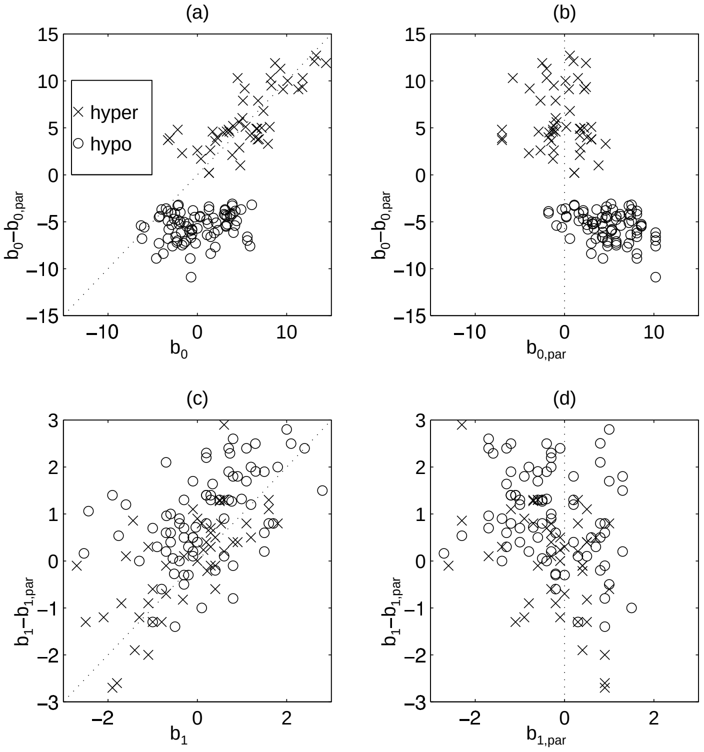

Figure 3.4 Relative versus normalized backscatter intercept (a) and slope (c) in metastases. Relative metastasis versus parenchyma backscatter intercept (b) and slope (d). The oblique dotted line in (a) and (c) pertains to $b_{.,\mathrm{abs,meta}} = b_{.,\mathrm{rel,meta}}$. The vertical dotted line in (b) and (d) pertains to $b_{.,\mathrm{par}} = 0$

3.4.3 Signal-to-noise ratio

The signal-to-noise ratio features SNR and $\langle snr \rangle$ could be estimated in all regions. Fig. 3.5 shows a scatter plot of the features SNR and $\langle snr \rangle$ in the patient data (a,b) and the normal subject data (c,d). The metastatic area was generally smaller than the parenchyma, thus the spread in metastases values is larger than in the parenchyma. The feature SNR was markedly increased in hypo, core, and halo type metastasis tissue, however, the same was true for the dummy type metastases. Thus the feature SNR is a spurious discriminator. The feature $\langle snr \rangle$ discriminated real nor dummy metastases from parenchyma.

The features SNR and $\langle snr \rangle$ were correlated (ellipsoids main axis is parallel to the line $snr = \langle snr \rangle$), but the feature SNR had lower values than $\langle snr \rangle$. There are indications that this is due to the window size. The feature $\langle snr \rangle$ is the average SNR estimated in the smallest windows and had the highest values. Metastases regions were larger than these small windows and had

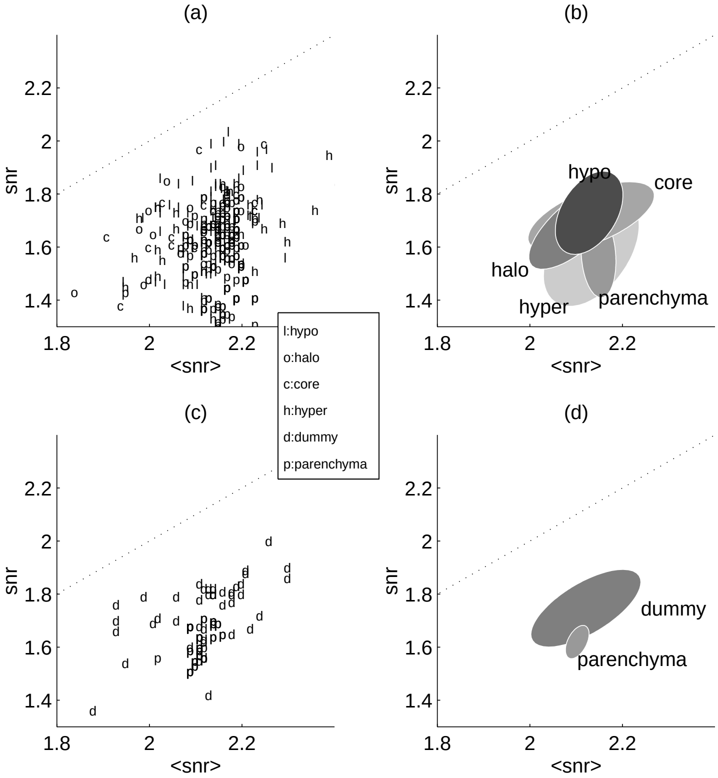

Figure 3.5 Scatter plots of snr features. The dotted line pertains to SNR=$\langle snr \rangle$. Subplots a) and b) pertain to real metastases, c) and d) pertain to dummy metastases.

lower SNR values. Parenchyma regions were the largest regions and had the lowest SNR values. This window size dependence may explain the false discriminative behavior. The low SNR of the hyper type metastasis can be attributed to the inhomogeneous nature of this type of metastasis, which results in an increased variance of the grey values.

3.5 Discussion

Metastasis model

The metastases model in Table 3.1 proved to be very helpful as it helped find typical characteristics of two common subtypes of metastases. A simple model in which all metastases are considered to be a single, homogeneous tissue group would otherwise have obscured the analysis. The assumed metastasis model is realistic as it reflects the common observation that ultrasonic appearance varies with: the type of primary tumor, and metastasis growth stage and (chemo-)therapy.

Feature selection

The small number of metastases in which attenuation could be reliably estimated (no estimation in halo regions) is an indication that the attenuation will be a feature of limited use to *in vivo* analysis of metastases. Moreover, the attenuation features were not different from values found in normal parenchyma. This is somewhat unexpected as in *in vivo* measurements on excised metastases Bamber et al. (1981) found a_0=-0.6 dB/cm and a_1=-0.2 dB/(cmMHz), and Cloostermans et al. (1986) found[4] a_0=-0.4dB/cm. The data used in this chapter is not sufficient to prove that there is no attenuation difference. However, because of the low precision, it can be concluded that the *in vivo* attenuation features cannot discriminate manually outlined metastases from parenchyma, which confirms similar *in vivo* observations by Parker et al. (1988). Attenuation remains an interesting feature, though, for analysis of diffuse liver diseases.

The relative backscatter feature ($b_0 - b_{0,\mathrm{par}}$) is an established discriminative feature which was used to categorize the metastases types. It was shown that the relative as well as normalized backscatter slope, is increased in hypo-echoic metastases and in the halo. This result was observed only because a specific metastasis model was used. The normalized backscatter (b_0, b_1) is easier to estimate and allows comparison between patients or different session of the same patient, but unfortunately the precision was too low for these features to be useful. The increased variability could have been caused by a number of phenomena:

- **Examination procedure** Overall echo-intensity variations often occur in practice, and can be related to manipulation pressure, ultrasound body entry positions (e.g. intra-costal, subcostal).
- **Skin thickness** The applied *in vivo* calibration technique implicitly corrects for average normal parenchyma and abdominal wall attenuation and diffraction. The attenuation correction extends to zero depth, i.e. including skin. A source of error arises when the attenuation in the skin is substantially different from that in the parenchyma. For example, assume a 1cm skin tissue layer and an attenuation difference (0.7 dB/cm; severe steatosis). An over-correction will occur, and the backscatter is over-estimated by $\Delta b_0 = 2 \times 0.7 = 1.4$dB.
- **Phase aberration** The fairly rough interface between the dermis and the sub-cutaneous fat may cause a degradation of the ultrasound beam resulting in decreasing lesion contrast (Berkhoff, 1996; Berkhoff and Thijssen, 1996).

It is not certain whether this item list correctly ranks each item's contribution to the deterioration. Further research will have to pinpoint relevant items and find error reduction strategies.

For varying window sizes, the feature SNR discriminated manually outlined metastases from parenchyma regions, however, it did so even in the case of dummy metastases. This phenomenon can not be explained by the homogeneous tissue model and, consequently, does not show up

---

[4] Results have been averaged and units converted to match those used in this chapter.

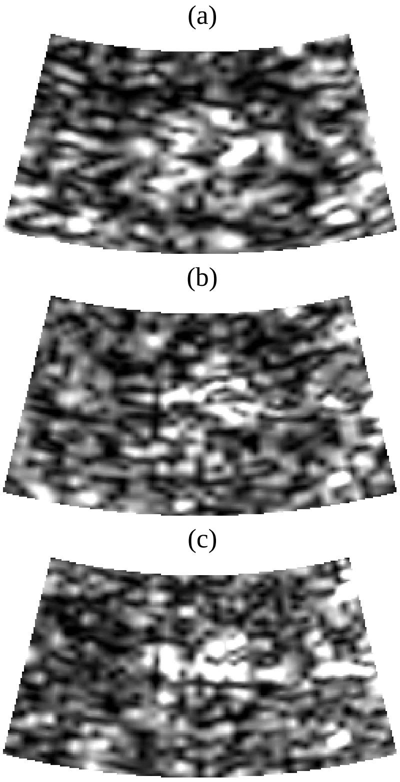

Figure 3.6 The metastasis with halo shown in Fig. 3.1a reconstructed at three new central frequencies: a) 2.5MHz, b) 3.0MHz, c) 3.5MHz. The relative bandwidth was 33%.

in simulated data. The next chapter will show that the feature SNR has a bias that depends on the window size in *in vivo* images due to additional, biological variations within the liver parenchyma. For fixed window sizes, the performance of the feature SNR is equal to that of $\langle snr \rangle$, which was shown to have no discriminative power.

On detection of metastases

The frequency dependence of the backscatter in the halo and in the hypo-echoic metastasis tissue is apparently greater than in surrounding parenchymal tissue. This leads to perhaps unfamiliar phenomena: the halo fades and the hypo-echoic metastases will become less hypo-echoic at higher frequencies. In other words, at higher frequencies the contrast decreases and the halo sign and hypo-echoic lesions become more difficult to detect. To demonstrate the effect, Fig. 3.6 shows three software filtered images obtained from the image in Fig. 3.1c at three different central frequencies. A 128-point FIR bandpass filter was used, and the image resolution (speckle) was held constant by fixing the new central frequency and bandwidth ratio: $bw_{\mathrm{new}}/f_{c,\mathrm{new}} = 0.33$. Fig. 3.6a shows that at low frequencies the hypo-echoic halo of the metastasis is well visible, while the halo starts to fade with respect to the surrounding parenchyma at higher frequencies (Figs. 3.6b and c). As it is the halo sign that made this metastasis even better visible, Fig. 3.6 shows that the detectability of metastases decreases at higher frequencies. The study of this phenomenon is part of future research.

Correlation of ultrasound with histology

The normalized echo-intensity (b_0) was shown not always to coincide with the relative echo-intensity ($b_0 - b_{0,\mathrm{par}}$) in metastases. The feature $b_0 - b_{0,\mathrm{par}}$ relates to visual assessment: a metastasis can be detected if $b_0 \neq b_{0,\mathrm{par}}$. The feature b_0 is relative to a fixed standard (i.e. ANP) and allows metastases from different patients or different sessions of the same patient to be compared; it reflects the status of the metastasis relative to healthy normal parenchyma. A number of metastases were found that were visibly hypo-echoic, but had iso-echoic b_0-values. For these metastases the hypo-echoic appearance is the result of surrounding hyper-echoic parenchyma. Yet, quite a few studies in literature correlate visible (relative) echogenicity to histology (Wernecke et al., 1992a; Marchal et al., 1985b; Sherar et al., 1987). The data in this study are too limited to conclude that hypo-echoic metastases appear only in hyper-echoic parenchyma, but it can be concluded that hypo-echoic metastases are not always hypo-echoic with respect to average normal parenchyma.

The increased backscatter level in the parenchyma tissue in the patients indicates a deviation from normal parenchyma. This could be caused by fatty infiltration that can arise during chemotherapeutic treatment (Garra et al., 1989). Furthermore, the metastases might also induce an inflammatory reaction in the liver parenchyma, which can lead to hepatic steatosis. The increased frequency dependence of the backscatter in hypo and halo type metastasis tissue was present not only relative to surrounding parenchyma, but also on an absolute scale. Thus contrary to b_0, b_1 does reflect that metastasis tissue histology is different from normal parenchyma tissue.

Follow-up

For each patient in the dataset several, serial sessions were available, yet, it appeared not to be possible to follow-up metastases by monitoring their feature values. No examples were found of a single metastasis that could be analyzed in a sufficiently large number of sessions. This is an indication that follow-up of metastases features will be difficult. Moreover, follow-up requires using the normalized backscatter, which was shown to have decreased precision.

A new follow-up strategy might be to use the semi-automatic halo-detection method, because the halo sign can predict metastases progression (Rettenmaier, 1990; Wernecke et al., 1992c). A feature of interest would be the halo thickness, and/or the relative amount of halo area within a metastasis. Another strategy would be the follow-up of the average backscatter **and** attenuation features in the liver parenchyma, because parenchyma features might also correlate with the presence and/or the development of tumors.

Bibliography

Bamber JC, Hill CR. Acoustic properties of normal and cancerous human liver – I dependence on pathological condition. Ultrasound Med Biol 1981;7:121–133.

Berkhoff AP. Ultrasonic imaging in aberating media. PhD thesis, Nijmegen University, 1996.

Berkhoff AP, Huisman HJ, Thijssen JM, Jacobs EMPG, Homan RJF. Fast scan conversion algorithms for displaying ultrasound sector images. Ultrason Imag 1994;16:87–108.

Berkhoff AP, Thijssen JM. Correction of concentrated and distributed aberrations in medical ultrasound imaging. In: IEEE Ultrasonics symposium. 1996: 1405–1410.

Brick SH, Hill MC, Lande IM. The mistaken or indeterminate CT diagnosis of hepatic metastases: The value of sonography. AJR 1987;148:723–726.

Cloostermans MJTM, Mol H, Verhoef WA, Thijssen JM, Kubát K. In vitro estimation of acoustic parameters of the liver and correlations with histology. Ultrasound Med Biol 1986;12:39–51.

Coleman DJ, Lizzi FL, Silverman RH, et al. Regression of uveal malignant melanomas following cobalt-60 plaque. Retina 1985;5:73–78.

Ferrucci JT. Liver tumor imaging: current concepts. AJR 1990;155:473–484.

Garra BS, Insana MF, Shawker TH, Russell MA. Quantitative estimation of liver attenuation and echogenicity: normal state versus diffuse liver disease. Radiology 1987;162:61–67.

Garra BS, Insana MF, Shawker TH, et al. Quantitative ultrasonic detection and classification of diffuse liver disease – comparison with human observer performance. Inv Radiology 1989;24:196–203.

Gonzalez RC, Wintz I. Digital image processing. Reading, Massachusetts: Addison-Wesley, 1987.

Hartman PC, Oosterveld BJ, Thijssen JM, Rosenbusch GJE. Variability and quantitative echographic parameters of the liver: intra- and interindividual spread, temporal- and age-related effects. Ultrasound Med Biol 1991;17:857–867.

King DL, Lizzi FL, Feleppa EJ, et al. Focal and diffuse liver disease studied by quantitative microstructural sonography. Radiology 1985;155:457–462.

Marchal G, Tshibwabwa-Tumba E, Oyen R, Pylyser K, Goddeeris R. Correlation of sonographic patterns in liver metastases with histology and microangiography. Inv Radiology 1985a;20:79–84.

Marchal GJ, Pylyser K, Tshibwabwa-Tumba E, et al. Anechoic halo in solid liver tumors: sonographic, microangiographic, and histologic correlation. Radiology 1985b;156:479–483.

O'Donnell M, Reilly, Jr. HF. Clinical evaluation of the B'-scan. IEEE Trans Sonics Ultras 1985;32:450–457.

Oosterveld BJ, Thijssen JM, Hartman PC, Romijn RL, Rosenbusch GJE. Ultrasound attenuation and texture analysis of diffuse liver disease: methods and preliminary results. Physics Med Biol 1991;36:1039–1064.

Oosterveld BJ, Thijssen JM, Verhoef WA. Texture of B-mode echograms: 3D simulations and experiments of the effect of diffraction and scatterer density. Ultrason Imag 1985;7:142–160.

Oppenheim AV, Schafer RW. Digital signal processing. Englewood Cliffs, NJ, USA: Prentice-Hall, 1975.

Parker KJ, Asztely MS, Lerner RM, Schenk EA, Waag RC. *In vivo* measurements of ultrasound attenuation in normal or diseased liver. Ultrasound Med Biol 1988;14:127–136.

Raeth U, Schlaps D, Limberg B, et al. Diagnostic accuracy of computerized B-scan texture analysis and conventional ultrasonography in diffuse parenchymal and malignant liver disease. J Clin Ultrasound 1985;13:87–99.

Rettenmaier G. Fokale leberveränderung. Chapter 3 in: Rettenmaier G and Seitz K, eds. Sonographische differentialdiagnostik. Weinheim, Germany: VCH Publishers, 1990.

Scheible W, Gossink BB, Leopold G. Gray scale echographic patterns of hepatic metastatic disease. AJR 1977;129:983–987.

Sherar MD, Noss MB, Foster FS. Ultrasound backscatter microscopy images the internal structure of living tumor spheriods. Nature 1987;330:493–495.

Verhoeven JTM. Improvement of echographic image quality by data analysis and processing. PhD thesis, Nijmegen University, 1994.

Verhoeven JTM, Thijssen JM. Improvement of lesion detection by echographic image processing: signal-to-noise-ratio imaging. Ultrason Imag 1991;13:238–251.

Wagner RF, Smith SW, Sandrik JM, Lopez H. Statistics of speckle in ultrasound B-scans. IEEE Trans Sonics Ultras 1983;30:156–163.

Wernecke K, Henke L, Vassallo P, et al. Pathologic explanation for hypoechoic halo seen on sonograms of malignant liver tumors: an in vitro correlative study. AJR 1992a;159:1011–1006.

Wernecke K, Rummeny E, Bongartz G, et al. Detection of hepatic masses in patients with carcinoma: comparative sensitivities of sonography, ct, and mr imaging. AJR 1991;157:731–739.

Wernecke K, Vassallo P, Bick U, Diederich S, Peters PE. The distinction between benign and malignant liver tumors on sonography: value of a hypoechoic halo. AJR 1992b;159:1005–1009.

Wernecke K, Vassallo P, Blick U, Diederich S, Peters PE. The distinction between benign and malignant liver tumors on sonography: value of a hypo-echoic halo. AJR 1992c;159:1005–1009.

Chapter 4

An *in vivo* ultrasonic model of liver parenchyma

4.1 Introduction

Quantitative[1] ultrasonic tissue characterization (UTC) methods can be used successfully to analyze diffuse liver diseases (Raeth et al., 1985; Garra et al., 1987; Parker et al., 1988; Garra et al., 1989; Oosterveld et al., 1991) and focal lesions in the liver (King et al., 1985; O'Donnell and Reilly, 1985) and chapter 3 *in vivo*. The number of features that are discriminative in the analysis of focal lesions is smaller than in the analysis of diffuse liver disease. This is partly due to the limited size of the estimation area, which results in a decreased precision of a feature. Knowledge of the relationship between precision and estimation area is important, because that knowledge may help to select discriminative features. Furthermore, a good prediction of the precision is required to assess the outcome of a measurement.

Previously, the relationship between precision and estimation area has been analyzed for four acousto-spectrographic features (intercept at central frequency and slope of the frequency dependent attenuation and backscatter coefficient) (see chapter 2), involving an explicit, ultrasonic model (tissue + scanner), that has been commonly assumed in the design of UTC methods. Simple, approximate expressions for the expected standard deviation (sd) of the four features were derived that extended existing literature on the subject and gave good insight into the effect of the window size on the precision. The predicted and estimated sd coincided well in simulated ultrasonic images of liver parenchyma. However, in *in vivo* liver images the estimated sd's were on average larger than predicted. This could partly be accounted for by the inter- and intra-variability of the liver, but the estimated sd of the intercept features remained unexpectedly high. In another study it was observed that the average value of the feature ”signal-to-noise ratio”(SNR) showed an unexpected dependence on window size in large windows (see chapter 3). Again, this did not occur when using images simulated according to the assumed ultrasonic model. These

---

[1] This chapter is based on the publication: Huisman H.J., Thijssen J.M., *Precision and accuracy of acousto-spectrographic parameters* submitted to IEEE Trans. UFFC

observations are a strong indication that the basic ultrasonic model lacks an essential, *in vivo* element. The objective of this chapter is to develop an extended ultrasonic model that can better predict the behavior of the features in *in vivo* liver parenchyma.
This chapter starts by describing the basic ultrasonic model of liver parenchyma. The experimental material comprised: images simulated according to the basic model, acquisitions of two tissue mimicking phantoms, and *in vivo* ultrasonic images of liver parenchyma. The parenchyma area in each image was manually outlined, as well as (large) structures within the parenchyma. To improve the segmentation a small blood-vessel detection method is developed. A simple, robust method results when incorporating large scale parenchyma background amplitude variations, or inhomogeneous parenchyma background (IPB). The IPB phenomenon is then described in statistical terms to enable extension of the basic ultrasonic model with new parameters. To test the extended model, the equations predicting the sd of the attenuation and backscatter features are extended with additional parameters, and expressions are derived that predict the relation of the bias of the feature SNR with the estimation window size in *in vivo* images. Finally, the sd and bias are estimated while using various window sizes for all four data sets and the results compared with the predictions.

4.2 The basic ultrasonic model

This section describes the basic ultrasonic model as it is often assumed in the design of UTC methods. To start with, ultrasonic images of liver parenchyma have a distinct granular appearance, called ”speckle”(see Fig. 4.1), which is the result of a multiplicative, correlated noise component. To describe the image statistics, the parenchyma is usually modeled as a medium containing many (more than 10 per sample volume), small (compared to the wavelength) and randomly distributed scatterers. Under these conditions, the *amplitude* spectrum, $\boldsymbol{E}(f)$, of the radio-frequency (rf) signal received in conventional pulse-echo mode, $\boldsymbol{e}(t)$, is a random variable (indicated by a bold symbol) with Rayleigh-distributed amplitude (Burckhardt, 1978):

$$Pr\left\{\boldsymbol{E}(f)=E\right\}=\frac{\pi E}{2\mu^2(f)}\exp\left(-\frac{\pi E^2}{4\mu^2(f)}\right), \tag{4.1}$$

where $\mu(f)$ is the mean signal amplitude component with frequency f. The sd, σ_R, of a stochastic variable with a Rayleigh distribution is related to the mean μ (Burckhardt, 1978) as

$$\sigma_R=\mu\sqrt{(4-\pi)/\pi}\approx\mu/1.91. \tag{4.2}$$

An actual, ultrasonic image is constructed from a set of rf lines, $e(z,\theta_i)$, where θ_i is the steering angle (assuming a sector scanner) of rf line i, and $z(=ct/2)$ is the depth, assuming the speed of sound, c, to be constant throughout the medium. The received spectrum is also affected by depth-dependent transducer- and tissue properties. These can be incorporated into the model by assuming that at depth z the average received spectrum, $\mu(f,z)$, is the output of a linear system, e.g. (Oosterveld et al., 1991). The received spectrum can then be written as:

$$\mu(f,z)=P^2(f)D^2(f,z)T^2(f,z)S(f), \tag{4.3}$$

Figure 4.1 Ultrasonic image of a transversal section in the liver. The liver is in between the bright area at the top (abdominal wall) and bright curved band (the diaphragm). Dark areas in the liver are veins as well as some bright reflections (due to vessel walls). The gray, speckle area represents the liver parenchyma.

where $P(f)$ is the acousto-electrical transfer function of the transducer, and $D(f, z)$ is the diffraction spectrogram of the transducer; they jointly describe the transducer characteristics. $T(f, z)$ is the tissue transfer function (attenuation), and $S(f)$ is the backscatter function; together these characterize the tissue.

The video image is used to calculate texture UTC features as well as for display purposes. It is obtained by first detecting the envelope of the rf-signals, $v(z, \theta_i)$, from the attenuation and diffraction corrected rf signal, $e'(z, \theta_i)$. The detection is carried out by taking the modulus of the analytical signal (Papoulis, 1977). Applying scanconversion (Berkhoff et al., 1994) to $v(z, \theta_i)$ results in the Cartesian, rectangular video image $v(x, y)$, such as shown in Fig. 4.1.

Adjacent pixels are correlated, which is visible in Fig. 4.1 as a speckle appearance. Knowledge about the speckle size is important, because it is the number of speckles rather than the number of pixels that determines the precision of a feature. The lateral, i.e. angular (θ), speckle size, s_l, is mainly due to the beam characteristics (Wagner et al., 1983). In the video image $v(x, y)$ in Fig. 4.1 it can be seen that s_l increases with depth, but when using the envelope detected rf

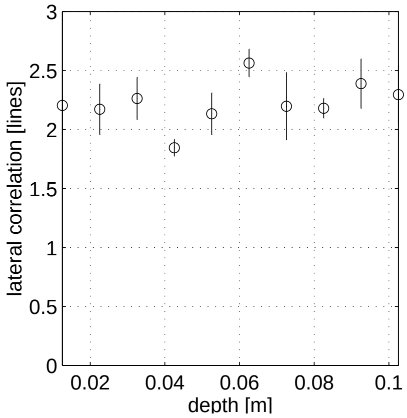

Figure 4.2 Lateral speckle size vs. depth estimated from the envelope detected rf lines in the parenchyma area in an *in vivo* acquisition showing a large parenchyma area. Correlation coefficient estimation window was 2.5 cm deep by $75°$ and was positioned at depth increments of 1 cm. Note that the lateral correlation length is expressed as a fraction of the number of rf lines (the angle between two rf lines is about $0.7°$).

lines, $v(z,\theta_i)$, of a sector scanner (i.e. before scan conversion) s_l can be assumed to be constant. Fig. 4.2 shows that indeed for the sector scanner used in this research (see Material section) s_l (in $v(z,\theta_i)$) can be taken to be constant within the depth-range involved in the analysis. The axial speckle size, s_k, is directly related to the pulse spectrum bandwidth, which can be assumed constant, because a frequency-dependent attenuation correction is applied, c.f. (Oosterveld et al., 1985). Effects due to beamwidth and bandwidth are assumed to be uncorrelated (Wagner et al., 1983), which allows the two-dimensional correlation coefficient $r(k,l)$ (for a definition see Appendix 4.8) to be written as the product of an axial and a lateral correlation coefficient:

$$r(k,l) = r_{\text{ax}}(k) r_{\text{lat}}(l). \tag{4.4}$$

The axial, s_k, and lateral, s_l, speckle size are defined as (Wagner et al., 1983):

$$\begin{aligned} s_k &= \int_{-\infty}^{\infty} r_{\text{ax}}(k)dk, \\ s_l &= \int_{-\infty}^{\infty} r_{\text{lat}}(l)dl. \end{aligned} \tag{4.5}$$

This definition assumes that the correlation coefficient can be adequately described by two speckle size parameters. It is this assumption that will be discussed in this chapter.

4.3 Experimental material

To demonstrate the discrepancies between theory and *in vivo* conditions and develop an extension to the model, four sets of ultrasonic images are used throughout this chapter: simulated images, acquisitions from two types of phantoms, and *in vivo* human liver. All acquisitions had the same file format to enable the same feature estimation methods to be applied to any image, which allowed to discriminate effects due to: the estimation methods, the acquisition system, and the tissue itself.

4.3.1 Simulation

A set of images was simulated (Romijn et al., 1989) according to the basic ultrasonic model described in sec. 4.2. The simulated tissue comprised homogeneously distributed point scatterers with on average 10 scatterers within the pulse sampling volume. The simulated scanner had a Gaussian shaped transducer pulse spectrum with a central frequency of 3 MHz and a -6 dB bandwidth of 1.88 MHz (mimicking the acquisition system). Each acquisition contained 100 independent rf lines with 2500 samples sampled at 15 MHz. The set was divided into 10 sets of 10 acquisitions representing a database of 10 patients.

4.3.2 Phantoms

Acquisitions were obtained from a rubber and from a foam phantom. The rubber phantom contained structures such as cysts, lesions, and hard wire reflectors (ATS Laboratories, Bridgeport, CT, USA), and was scanned at 19 positions (14 acquisitions from the top and 5 from the side). The foam phantom was made of a 90ppi (3.54 pores/mm) reticulated polyurethane network (Bulpren S90, Recticel, Kesteren, The Netherlands). The 20x20x20cm foam cube was immersed into water and thoroughly degassed (1 mBar end-pressure) and subsequently scanned at 16 positions at various orientations.

4.3.3 Liver

A set of 128 acquisitions of the liver was recorded from 12 healthy, human subjects (6 male, 6 female) with an empty stomach before breakfast. At the department of Radiology an experienced sonographer acquired from each liver at least 5 transversal and 5 longitudinal sections using routine scanning procedures.

4.3.4 Acquisition and preprocessing

A Toshiba Sonolayer SSA270A scanner with a PSF37-CT 3.75 MHz phased array transducer (F=7.5cm) was used in single focus mode to scan the phantoms as well as *in vivo* livers. Connected via a custom-built interface in the scanner, the data acquisition system acquired full-frame rf-data at a sampling frequency of 15 MHz (see chapter 2). Each acquisition contained 110 rf lines with 2950 samples ($\approx 75^\circ \times$ 15cm).

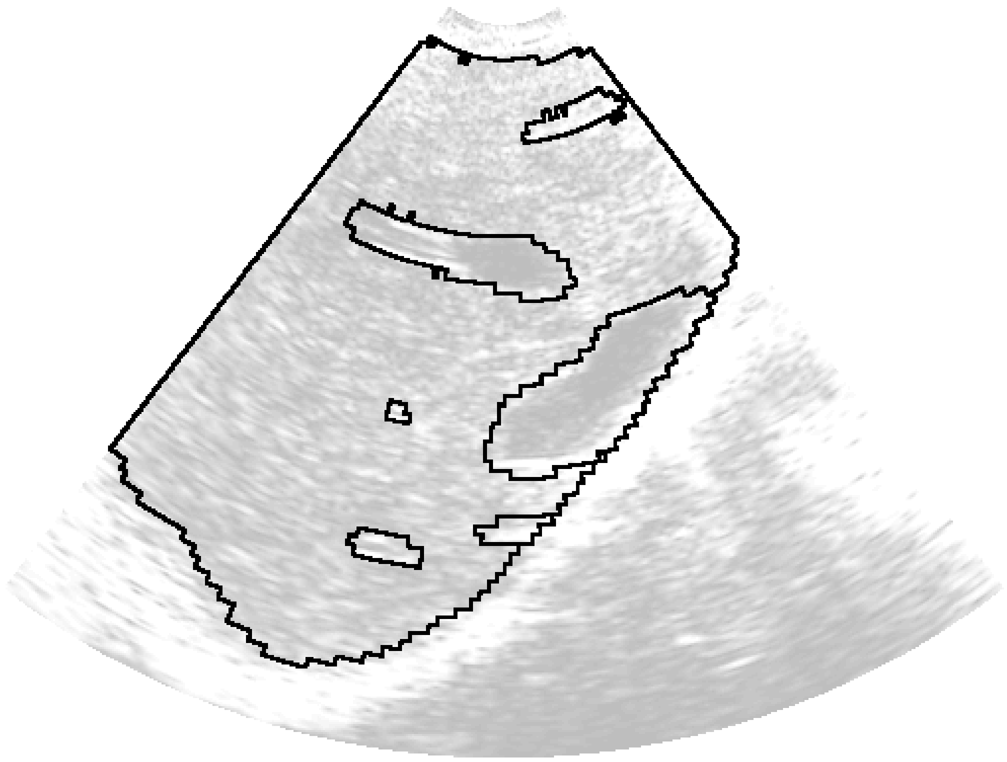

Figure 4.3 Outlines of regions in the manual mask matrix that are projected as thick black lines on the example ultrasonic image (Fig.4.1).

Estimation of features should be restricted to the parenchyma region, and to that end a mask matrix, $m(z, \theta_i)$ was used. The mask matrix had the same dimensions as the rf-matrix, $e(z, \theta_i)$. Each mask element designated the label of the corresponding sample in the rf matrix. Software was developed that enabled manual outlining of structures within an ultrasonic image. Outlines were drawn in an overlay, $m(x, y)$, on the scan-converted image $v(x, y)$ (see Fig. 4.3). Each outline in the overlay was filled-in with a specific label that indicated the type of tissue. Identified types were: large blood-vessels, ligaments, hyper-echoic region beneath a low attenuating region (e.g. gall-bladder), regions behind highly reflective or attenuating obstacles (e.g. rib), or hypo-echoic regions due to bad transducer-skin contact regions. The labels in the mask matrix, $m(z, \theta_i)$, were obtained by resampling the nearest neighbor interpolated, filled-in overlay, $m(x, y)$.

4.4 Inhomogeneous parenchyma background (IPB)

The detailed analysis of the parenchyma properties as intended in this chapter requires a good segmentation of the parenchyma-only region. It was observed that small bloodvessels were easily missed in the manual segmentation, therefore an automatic small bloodvessel detection method (SBDM) was developed. A global threshold method will be selected in this section and its operating parameters will be derived from the basic ultrasonic model. This method can be shown to work well on simulated images, but in order to obtain good results on the liver data, the global threshold method will be extended with an IPB correction step. This extension not only makes the global method operate well on the liver data, but also leads to the visualization of IPB.

4.4.1 Small blood-vessel detection without acknowledging IPB

A simple SBDM results if a two-level, global threshold is applied to the average gray value, $\overline{v}_{\text{det}}$, of a local detection window in the envelope image, $v(z, \theta_i)$. This method will detect two types of structures within the manually delineated parenchyma: hyper-echoic (above high threshold), and hypo-echoic (below low threshold).

The SBDM detection window size was chosen to be 3x3 speckles. Firstly, the size is expressed in speckles, because the effective window size (9 independent variables) is proportional to the number of speckles (Wagner et al., 1983). Furthermore, this shape of window does not assume any orientation of the structures to be detected. Finally, this is the smallest window of which the average gray value has approximately a Gaussian distribution (Central Limit Theorem, (Papoulis, 1991)).

The low and high threshold levels are determined by the maximum amount of falsely detected area that is allowed. This amount can be predicted, because the probability density function of $\overline{v}_{\text{det}}$ is a Gaussian. The thresholds are set at $\mu - 3\sigma_{\text{det}}$ and $\mu + 3\sigma_{\text{det}}$. This results in 0.26% incorrectly detected structures. The sd of the average of 9 independent Rayleigh distributed variables is approximately:

$$\sigma_{\text{det}} \approx \sigma_R/\sqrt{9} = \mu/(1.91\sqrt{9}) = 0.17\mu, \tag{4.6}$$

where μ is the (global) mean parenchyma amplitude. The thresholds then become 0.5μ and 1.5μ.

4.4.2 Small blood-vessel detection acknowledging IPB

In the liver data, the previously described global threshold SBDM resulted in large regions in the parenchyma area incorrectly being labeled as hypo- or hyper-echoic. This phenomenon is analogous to the“background illumination problem” in image processing (Gonzalez and Wintz, 1987), and is an indicator for the presence of an inhomogeneous parenchyma background (IPB). To cope with this problem, SBDM was extended with an IPB image correction method.

The IPB image was detected by low-pass filtering the envelope image $v(z, \theta_i)$. A uniform 10x10 speckle filter window was chosen, because relevant structures that size are easily labeled manually and should already be contained in the mask matrix (see Material section); remaining large structures thus constitute the IPB. However, a large, uniform filter window has poor stop band

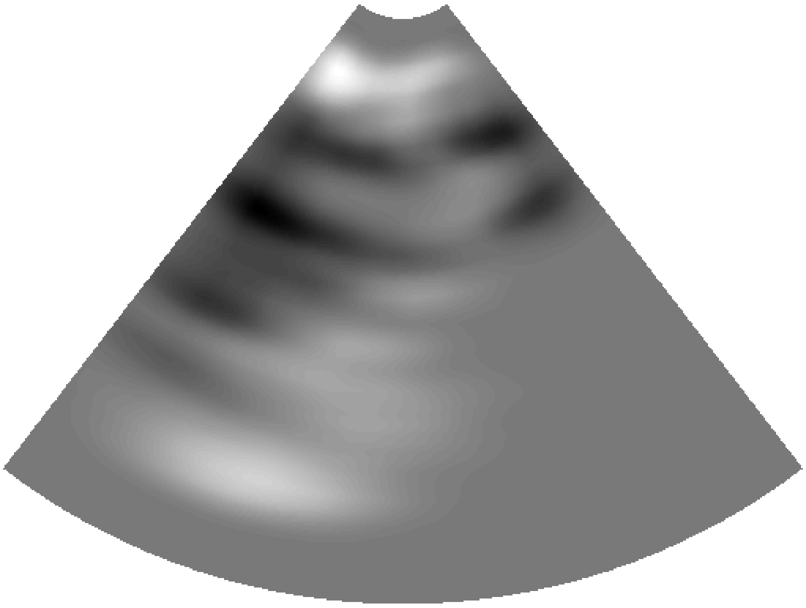

Figure 4.4 The detected IPB image from the example sonogram (Fig. 4.1). The gray values have been log transformed for paper display purposes, and the difference between darkest black and brightest white area is 5 dB.

characteristics: small, but high contrast areas will smear out into the estimated IPB image. The solution used is to fill in non-parenchyma area with the estimated average value of the parenchyma area.

The IPB effect is removed by dividing the envelope image by the detected IPB image, because of the multiplicative nature of the Rayleigh distribution. This additionally normalizes the original ultrasonic image (i.e. resulting in $\mu = 1$), which then simplifies the segmentation thresholds to: 0.5 and 1.5. A further improvement was obtained by leaving out newly detected non-parenchyma area before smoothing, which is accomplished by making the SBDM algorithm iterative. In each iteration, the mask is updated with newly detected blood-vessels, and the background IPB image is re-estimated. Iteration stops when the newly detected area comprises fewer than 9 speckles. In practice, SBDM was found to require 4–8 iterations.

The resulting SBDM was applied to the set of liver images. Fig. 4.4 shows the detected IPB image from the example liver image (Fig. 4.1). The amplitude range is approximately 5 dB, which is

Figure 4.5 Outlines of manual and SBDM mask are projected as thick black lines on the example ultrasonic image 4.1.

about the same as the upper and lower thresholds ($\approx +/-6$ dB). This explains the unexpected large regions previously detected. After dividing by the IPB image, no unexpected large regions were segmented in any images of the liver set. Detected small structures were in good agreement with visible structures. The mask resulting after manual detection and SBDM on the example image is shown in Fig. 4.5. An additional effect of the SBDM algorithm was seen, it improved imperfections in boundaries of manually detected structures (c.f. Fig. 4.3).

The SBDM developed in this section was used to enhance the manual segmentation in all data sets. This section also introduced IPB, and Fig. 4.4 shows that IPB is a low amplitude, long-range correlation noise component. The effect of IPB on the estimated features has to be estimated, because it is not possible to detect the IPB in pathological images. Faintly visible tumors will be filtered out and a subsequent detection method then would fail to operate.

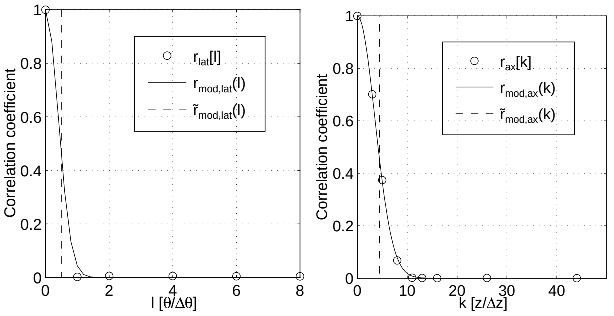

(a) Lateral correlation coefficient

(b) Axial correlation coefficient

Figure 4.6 The circles indicate the average values as estimated in the simulations. The solid line shows the fitted Gaussian model correlation coefficient including IPB (Eq. 4.10) , the dashed line is the zero order approximation of the Gaussian model (Eq. 4.13).

4.5 Extension of the basic ultrasonic model with IPB

To enable a prediction of the effect of IPB on the estimated features, first IPB is included in the ultrasonic model. It can be expected that if IPB is present, then it will show up in the correlation coefficient (Eq. 4.4). In this section, first the effect of IPB upon the correlation coefficient is studied. Next, the ultrasonic model is extended with an extra noise term and a parameterized correlation coefficient with parameters that describe speckle as well as IPB.

4.5.1 The effect of IPB on the correlation coefficient

The correlation coefficient was estimated in the parenchyma area of the ultrasonic images by:

$$\begin{aligned} r[k,l] &= \frac{1}{MN}\sum_m\sum_n v'[z_m,\theta_n]v'[z_m+k,\theta_n+l] \\ v'[z_m,\theta_n] &= (v[z_m,\theta_n]-\overline{v})/s, \end{aligned} \tag{4.7}$$

where $\overline{v}$ is the average value, s is the estimated sd, and MN is the image size (Oppenheim and Schafer, 1975; Gonzalez and Wintz, 1987). The estimation was restricted to samples in the segmented parenchyma by estimating $\overline{v}$ and s from parenchyma samples (i.e. the non-parenchyma samples were set to zero in the double summation, and the product MN was set to the number of parenchyma samples in the image).

The correlation coefficient was estimated in the simulated and liver images from the diffraction and attenuation corrected, and envelope detected rf lines before scanconversion $v(z,\theta_i)$. In the liver, a full width, but shallow depth (4.5cm) window centered at the focus of the transducer was

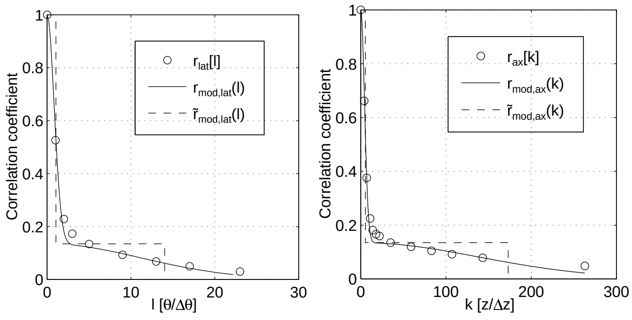

(a) Lateral correlation coefficient

(b) Axial correlation coefficient

Figure 4.7 The circles indicate the average values as estimated in the liver dataset. The solid line shows the fitted Gaussian model correlation coefficient including IPB (Eq. 4.10) , the dashed line is the zero order approximation of the Gaussian model (Eq. 4.13). In the focus $\theta/\Delta\theta$ ≈1 mm and $z/\Delta z$ ≈0.05mm.

used, because the lateral IPB cell size, being a physical property of the liver, is not constant in the polar domain. The coefficient was decomposed into a lateral and an axial component (see Eq. 4.4).
The circles in Fig. 4.6 show the results when using the simulations. These images had independent rf lines, which is clearly visible in Fig. 4.6a. The axial correlation coefficient (Fig. 4.6b) is non-zero over a short distance (corresponding to the speckle size). The results when using liver images (Fig. 4.7) are clearly different. The axial (Fig. 4.7a) and lateral (Fig. 4.7b) coefficients show significant correlation far beyond the speckle size. The low levels of correlation and the long range trend are both indicative of IPB.

4.5.2 Correlation coefficient including IPB

The IPB component will result in an increase of the sd in the images (Eq. 4.2). Assuming that IPB is an additive process independent of speckle (e.g. large scale fluctuations of scatterer concentrations), and if the ratio of the IPB and speckle variances, $\sigma^2_{\mathrm{IPB}}/\sigma^2_R$, is denoted as α, then the sd, σ_v, of the echo amplitude v becomes:

$$\sigma_v = \sigma_R\sqrt{1+\alpha}. \tag{4.8}$$

For additive processes, the correlation coefficient can be separated into a speck component:

$$r(k,l) = \frac{r_{\mathrm{speckle}}(k,l) + \alpha * r_{\mathrm{IPB}}(k,l)}{1+\alpha}. \tag{4.9}$$

This equation is not sufficient to estimate $r_{\mathrm{speckle}}(k,l)$ and $r_{\mathrm{IPB}}(k,l)$ from an estimated $r[k,l]$. To assess the characteristics of speckle as well as IPB it is further assumed that $r_{\mathrm{speckle}}(k,l)$

	simulation	foam	rubber	*in vivo*	units
s_l	1.00	1.71	1.76	2.09	$\theta/\Delta\theta$
s_k	8.9	9.2	10.3	11.0	$z/\Delta z$
α	0.000	0.033	0.042	0.156	
β_l in focus	-	14.5	20.0	28.1	$\theta/\Delta\theta$
β_k	-	100	100	345	$z/\Delta z$

Table 4.1 Speckle (s_l, s_k) and IPB $(\alpha, \beta_l, \beta_k)$ parameters estimated in four media.

and $r_{\mathrm{IPB}}(k,l)$ can each be modeled by a bivariate Gaussian function. The ultrasonic model correlation coefficient then becomes:

$$r_{\mathrm{mod}}(k,l;X) = \frac{\exp(-\frac{\pi l^2}{s_l^2} - \frac{\pi k^2}{s_k^2}) + \alpha \exp(-\frac{\pi l^2}{\beta_l^2} - \frac{\pi k^2}{\beta_k^2})}{1+\alpha}, \tag{4.10}$$

where β_l and β_k determine the IPB correlation cell size defined in the same manner as the speckle cell size $(s_l, s_k$ in Eq. 4.5).

The ultrasonic model correlation coefficient indicated in Eq. 4.10 is a five parameter function: $X = \{s_l, s_k, \alpha, \beta_l, \beta_k\}$. The parameters can be estimated by fitting $r_{\mathrm{mod}}(k,l;X)$ to the estimated correlation coefficient, $r[k,l]$, using a minimization procedure:

$$X_{\mathrm{opt}} = \arg\min_X \left\{ \sum_k \sum_l [r[k,l] - r_{\mathrm{mod}}(k,l;X)]^2 \right\}. \tag{4.11}$$

The minimization was carried out by the *constr()* function from the Matlab optimization toolbox (Grace, 1992), that can handle constraints to efficiently search a restricted, realistic solution space. The constraints were taken as:

$$\begin{aligned} 1 &< s_l < 2s_{l,\mathrm{init}} \\ 1 &< s_k < 2s_{k,\mathrm{init}} \\ 0.0001 &< \alpha < 0.5 \\ 2s_{l,\mathrm{init}} &< \beta_l < 0.5L \\ 2s_{k,\mathrm{init}} &< \beta_k < 0.5K, \end{aligned} \tag{4.12}$$

where $s_{l,\mathrm{init}}$ and $s_{k,\mathrm{init}}$ are the initial speckle size, and L, K are the size of the correlation coefficient matrix.

The ultrasonic model correlation coefficient was fitted to the average correlation coefficient estimated in each of the four data sets. Figs. 4.6 and 4.7 show that the estimated correlation in simulations as well as the *in vivo* acquisitions are fitted equally well, which is an indication that a Gaussian correlation coefficient was a plausible assumption. Table 4.1 summarizes the values of the five speckle and IPB parameters estimated on the four different media. The simulations had independent rf lines, which is correctly estimated ($s_l = 1.00$). The estimated IPB strength in

simulations ($\alpha = 0.000$) correctly shows that the simulations do not contain IPB (β_l, β_k are irrelevant). The estimated IPB level in *in vivo* images ($\alpha = 0.156$) shows that the IPB signal is rather weak, which could have been expected as it is not directly visible. The lateral IPB cell width (expressed in number of lines) was estimated in the focus of the transducer and thus pertains to windows in the focal zone. This is not a problem, because in the polar domain β_l depends in a predictable manner on the depth. The physical IPB cell size is about 4cm^2. Finally, the phantoms, which are assumed to be homogeneous, show relatively small signs of IPB.
In the next section the model correlation coefficient will be used to derive the expected statistics of the UTC features. The derivation requires integrating the correlation coefficient (see Appendix), which leads to expressions that are difficult to interpret. Manageable expressions result when using a zero-order approximation of Eq. 4.10:

$$\tilde{r}_{\mathrm{mod}}(k,l) = \frac{U(s_k/2 - |k|)U(s_l/2 - |l|) + \alpha U(\beta_k/2 - |k|)U(\beta_l/2 - |l|)}{1+\alpha}, \tag{4.13}$$

where ˜ designates the zero-order approximation, and $U(.)$ is the step function. The values of the five parameters are obtained from the fit of the Gaussian model. The dashed lines in Figs. 4.6 and 4.7 show the zero-order correlation coefficients. Although the approximation looks rather poor, it does produce good predictions. For example, the sd of the average value is predicted by Eq. 4.20 and can use either Eq. 4.10 or the approximation Eq. 4.13. With the *in vivo* parameters it can be shown that the two predicted sd's are nearly identical in the window size range used in this study.

4.6 Predicted accuracy and precision using the extended ultrasonic model

The extended noise term and the parameterized ultrasonic model correlation coefficient derived in the previous section extend the basic ultrasonic model with the notion of IPB. In this section the extended model will be used to predict the relationship between the statistics of the UTC features and the window size. The effect of IPB upon the SNR is different from the effect upon the acousto-spectrographic features, thus these will be treated separately.

4.6.1 The accuracy of the SNR

The feature SNR is calculated from an estimation window w in the video image v as:

$$\mathrm{SNR} = \frac{\overline{v}_w}{s_w}, \tag{4.14}$$

where $\overline{v}_w$ is the average value and s_w is the estimated sd in the window. Without IPB being present, the expected SNR would be on average ($\mu_R/\sigma_R =$) 1.91 for large window sizes (Burckhardt, 1978). Even without IPB there is already a window size dependence, because in windows in the order of the speckle size the correlation between pixels tends to underestimate s_w, which

Window size ($X \times Y$)	$\tilde{\sigma}_{\overline{v}}$	$\widetilde{\mathrm{SNR}}$
1. $(X < \frac{s_k}{2}) \wedge (Y < \frac{s_l}{2})$	$\sigma_R\sqrt{1+\alpha}$	∞
2. $(X = s_k < \frac{\beta_k}{2}) \wedge (Y = s_l < \frac{\beta_l}{2})$	$\sigma_R\sqrt{0.56+\alpha}$	4.8
3. $(X = 10s_k < \frac{\beta_k}{2}) \wedge (Y = 10s_l < \frac{\beta_l}{2})$	$\sigma_R\sqrt{0.01+\alpha}$	1.91
4. $(X = 10s_k = \beta_k) \wedge (Y = 10s_l = \beta_l)$	$\sigma_R\sqrt{0.01+0.56\alpha}$	$\frac{1.91}{\sqrt{1+0.44\alpha}}$
5. $(s_k \ll X = 10\beta_k) \wedge (s_l \ll Y = 10\beta_l)$	$\sigma_R\sqrt{0.01\alpha}$	$\frac{1.91}{\sqrt{1+\alpha}}$

Table 4.2 The expected sd, $\tilde{\sigma}_{\overline{v}}$, of the average value, $\overline{v}$, and the expected SNR, $\widetilde{\mathrm{SNR}}$, calculated for five window sizes using the zero-order approximation (˜) of the Gaussian correlation coefficient. Window size is: (1) smaller than one speckle; (2) equal to speckle, but smaller than IPB cell; (3) 100 speckles, but smaller than IPB cell; (4) 100 speckles and equal to IPB cell; (5) 100 IPB cells.

results in a increased SNR. This relation is well known (Verhoeven and Thijssen, 1991; Dutt and Greenleaf, 1995).
The relation between window size and expected SNR in the presence of IPB is derived in Appendix A. The relationship between SNR and the window size using the zero-order model, Eq. 4.13, is given in Eq. 4.26. For small windows, $\widetilde{\mathrm{SNR}}$ is large and it is still rather large (4.8) if the window size is equal to the speckle cell size, even without IPB being present. At increasing window sizes, but within the IPB cell size, or without IPB, the SNR approaches 1.91. However, in the presence of IPB the SNR is predicted to decrease even further for window sizes larger than the IPB cell size. In the limit the SNR is predicted to be $\frac{1.91}{\sqrt{1+\alpha}}$. Table 4.2 lists the expected $\widetilde{\mathrm{SNR}}$ for some typical window sizes.

4.6.2 The precision of acousto-spectrographic features

Four acousto-spectrographic features can be estimated from the averaged spectrogram, $\overline{E}(f,z)$, (average over θ) in a window in the rf-image, $e(z,\theta_i)$. An estimate of the tissue dependencies results after removing the calibrated transducer dependencies:

$$\begin{aligned}
\hat{T}(f,z)\hat{S}(f) &= \frac{\overline{E}(f,z)}{D(f,z)P(f)} \\
b(f) + 2za(f) &= \log\left(\hat{T}(f,z)\hat{S}(f)\right) \\
b_0 + b_1(f - f_c) &= b(f) \\
a_0 + a_1(f - f_c) &= a(f),
\end{aligned} \tag{4.15}$$

where it is assumed that the attenuation- ($a(f)$) and backscatter-coefficient ($b(f)$) can be linearized in a limited bandwidth (1.88 MHz, -6 dB bandwidth). The central frequency, f_c, and bandwidth are pre-selected for a scanner-transducer combination. The estimation methods have been described in full detail in chapter 2, as well as the equations predicting the sd assuming the basic ultrasonic model ($\sigma_{a_0}, \sigma_{a_1}, \sigma_{b_0}, \sigma_{b_1}$).
The feature b_0 is strongly correlated to $\overline{v}_w$. The expected precision of $\overline{v}_w$ using the zero order correlation model, Eq. 4.13, is given in Eq. 4.21. Table 4.2 summarizes $\tilde{\sigma}_{\overline{v}}$ for some typical

window sizes and shows that the window size dependence is determined by two terms. The first term under the square root is due to the speckle process and reduces approximately with the number of speckles. The second term is due to IPB and it decreases at a rate determined by the number of IPB cells. Due to the large cell size of IPB, the second term becomes dominant at large window sizes. The net effect of IPB on σ_{b_0} can be calculated by adopting the following notation. Let $\sigma_{\overline{v}}(\alpha)$ be the sd of a feature due to speckle and IPB. Let $\sigma_{\overline{v}}(0)$ be the sd due to speckle only (applying Eq. 4.21 with: $\alpha = 0$). Then $\sigma_{\overline{v}}(\alpha)/\sigma_{\overline{v}}(0)$ is the sd increase factor due to IPB.

A second feature sensitive to amplitude variations is a_0. It is estimated by the laterally (θ) averaged amplitude attenuation in the depth direction, z, within the window. The lateral window size dependence will be the same as for the feature b_0, however, the axial dependence of σ_{a_0} on the window size is $1/M\sqrt{M}$ instead of $1/\sqrt{M}$ (see chapter 2). The net effect of IPB can be predicted by writing $\sigma_{\overline{v}}$ as the product of the lateral and axial part: $\sigma_{\overline{v}} = \sigma_{\overline{v},l}\sigma_{\overline{v},k}$. Then using the notation of the previous paragraph: $\sigma_{\overline{v},l}(\alpha)\sigma^3_{\overline{v},k}(\alpha)/(\sigma_{\overline{v},l}(0)\sigma^3_{\overline{v},k}(0))$ is the sd increase factor due to IPB.

The predicted sd including IPB becomes:

$$\begin{aligned}
\sigma_{a_0,\mathrm{IPB}} &= \frac{\sigma_{\overline{v},l}(\alpha)\sigma^3_{\overline{v},k}(\alpha)}{\sigma_{\overline{v},l}(0)\sigma^3_{\overline{v},k}(0)}\sigma_{a_0} \\
\sigma_{b_0,\mathrm{IPB}} &= \frac{\sigma_{\overline{v}}(\alpha)}{\sigma_{\overline{v}}(0)}\sigma_{b_0},
\end{aligned} \tag{4.16}$$

The sd of the frequency dependent features a_1, and b_1 could already be predicted quite well without using the notion of IPB. The equations for these slope features are extended only with a term to express the increased variance:

$$\begin{aligned}
\sigma_{a_1,\mathrm{IPB}} &= \sigma_{a_1}\sqrt{1+\alpha} \\
\sigma_{b_1,\mathrm{IPB}} &= \sigma_{b_1}\sqrt{1+\alpha}
\end{aligned} \tag{4.17}$$

4.7 Results

In this section the results are discussed of an experiment carried out to compare the predicted sd and bias of the features with actual estimates. The predictions are based either on the basic ultrasonic model, or the ultrasonic model extended with IPB.

The features were estimated in seven windows of different size. A window was either 12 or 30 rf lines wide and 640, 912, or 1152 samples deep, or the window had the size of the full ultrasonic image. The six, smaller windows were positioned at various locations in the image with 50% overlap in the depth direction, and 67% overlap in the lateral direction. A small window was only used if at least 90% of the rectangular area was unmasked parenchyma area.

In Fig. 4.8 the average SNR estimated from the experiment is plotted versus the window size expressed in number of speckles. The smallest window size comprised about 100 speckles and, as expected, the SNR in simulations is at or about the Rayleigh limit and independent of the window size. The SNR in *in vivo* parenchyma decreases at large window sizes to a value far below the Rayleigh limit and reaches a new limit which from Tables 4.1 and 4.2 is predicted to

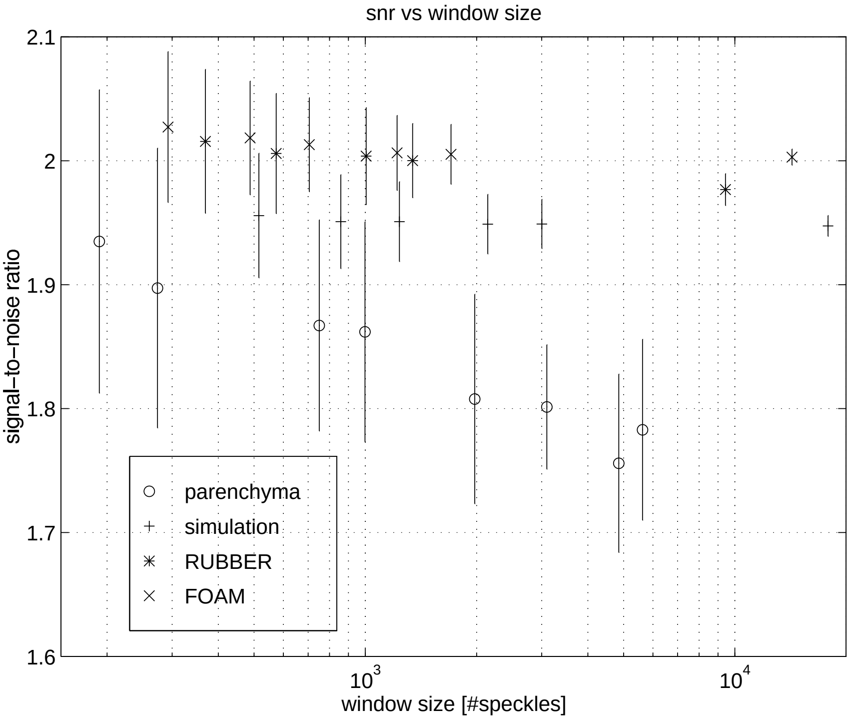

Figure 4.8 SNR versus window size in the four data sets. The vertical lines are error bars (+/- 1 s.d.)

be 1.79 ($= 1.91/\sqrt{1+0.156}$). The effect of IPB on the feature SNR in the phantoms is hardly visible.

The acousto-spectrographic features were normalized to the average value within each acquisition, thereby removing effects due to inter- and intra-organ variations. At each window size the predicted sd's (σ) were divided by the estimated sd's (s) which resulted in a ratio (σ/s). The prediction could be with or without assuming IPB, thus two ratios were calculated. The ratios at all window sizes were averaged for each data set. Table 4.3 shows the results. The predictions in simulations agree very well with the estimates for both models. The IPB effect was small in the phantoms, however, the estimated sd for the intercept features is slightly better predicted when considering IPB. The predictions in *in vivo* data increase significantly when including IPB, especially for the intercept features a_0, and b_0.

4.8 Discussion

The aim of this chapter has been to extend the ultrasonic model such that it could explain and predict the accuracy and precision of some well-known UTC features. The existence of inhomoge-

Dataset	Feature	σ/s	σ_{IPB}/s
Simulation	a_0	0.92 (0.01)	0.94 (0.01)
	a_1	1.02 (0.01)	1.02 (0.01)
	b_0	1.09 (0.01)	1.12 (0.01)
	b_1	1.11 (0.01)	1.11 (0.01)
Foam	a_0	0.81 (0.01)	1.18 (0.01)
	a_1	0.88 (0.01)	0.90 (0.01)
	b_0	0.61 (0.01)	0.88 (0.01)
	b_1	0.97 (0.01)	0.99 (0.01)
Rubber	a_0	0.67 (0.02)	1.00 (0.03)
	a_1	0.95 (0.02)	0.97 (0.02)
	b_0	0.60 (0.01)	0.92 (0.02)
	b_1	0.86 (0.01)	0.88 (0.01)
Liver	a_0	0.24 (0.01)	1.04 (0.02)
	a_1	0.78 (0.01)	0.84 (0.01)
	b_0	0.18 (0.00)	0.47 (0.01)
	b_1	0.67 (0.01)	0.72 (0.01)

Table 4.3 Average (over all window sizes) ratio of predicted over estimated standard deviation, without (σ/s) or with IPB (σ_{IPB}/s), of four acousto-spectrographic features in four datasets. Number between brackets is the standard error of the average ($N_{\mathrm{win}}\approx 50$).

neous parenchyma background in *in vivo* data has been made plausible by means of developing a small bloodvessel detection method to operate on *in vivo* images. The IPB-effect was also shown to be present in the correlation coefficient as the long-range part of the correlation coefficient. The ultrasonic model extended with IPB was able to explain: 1. the dependence of the feature SNR on the window size; 2. the increased variance of the acousto-spectrographic UTC features in *in vivo* images. It can be concluded that IPB is a realistic and relevant phenomenon which should be part of the ultrasonic model of the liver parenchyma used in UTC methods design.

The basic ultrasonic model of liver parenchyma has been used often in literature on UTC. However, the presence of background variations has been acknowledged before. Wagner et al. (Wagner et al., 1983) ascribed the long-range trends in the correlation coefficient to background variations due to the imaging system and in fact they applied a technique analogous to IPB correction. Insana et al. (Insana et al., 1986) implicitly avoided IPB in *in vivo* images, because they detected blood-vessels in a local matched-filter environment.

The extended ultrasonic model was able to accurately predict the dependence of the feature SNR on the window size using the extended ultrasonic model. It is concluded that in *in vivo* images of liver parenchyma the expected value of the feature SNR depends in a predictable manner on the window size in realistic windows, because of the presence of IPB. As a result, the estimates of the feature SNR in differently sized windows (e.g. in metastases in the liver parenchyma) can not be compared, which confirms with rhe observations in chapter 3.

The prediction of the precision of the acousto-spectrographic features was improved by the extended ultrasonic model. The IPB phenomenon explains the decrease in precision of the features attenuation and backscatter intercept at central frequency. Thus, the previously observed discrepancy between estimated and predicted precision can not be ascribed to shortcomings in the UTC feature estimation methods, but is an inherent property of the investigated medium.

The phenomenon IPB is a characteristic of liver parenchyma. Given the IPB correlation cell size (4cm^2) the phenomenon should occur on a larger scale than the hepatocyt (20-30μm), or the lobules (1mm). An appropriate scale is the segmental anatomy on the basis of the Couinaud nomenclature, where the branches of the portal vein lead to the center of individual segments (Lafortune et al., 1991). These segments may have an increase or decrease of fat content and then occur in ultrasonic images as hyper- or hypo-echoic regions (Rettenmaier, 1990). The hepatic (sub)segment-scale variations also occur in other imaging modalities. Kanematsu et al. (Kanematsu et al., 1997) observed nonpathological enhancements on spiral CT presumably due to subsegmental perfusion abnormalities. Kadoya et al. (Kadoya et al., 1994) reported MRI hypointense regions possibly caused by a disturbance in portal blood flow. These authors report strong and visible effects on the (sub)segmental scale. It is hypothesized that IPB may be due to normal, small perfusion variations on the (sub)segmental scale.

The tissue mimicking (TM) phantoms showed a small amount of IPB. The effect was hardly noticeable for the feature SNR, and only a small decrease was observed for the precision of the acousto-spectrographic features. Thus for the design of UTC methods to operate on liver parenchyma the TM-phantoms lack the *in vivo* feature: IPB. Chapter 2 revealed that the same two TM-phantoms were also not adequate for transducer calibration in *in vivo* data. Thus it is concluded that the use of presently available TM-phantoms in the development and validation of UTC methods should be construed with caution.

Appendix A: Statistics of average value, estimated variance and SNR

If $\mathbf{v}(x,y)$ is a wide-sense stationary stochastic image variable, then the autocorrelation, $R(k,l)$, autocovariance, $C(k,l)$, and the correlation coefficient, $r(k,l)$, are defined as (Papoulis, 1991):

$$\begin{aligned} R(k,l) &\triangleq E\left\{\mathbf{v}(x,y)\mathbf{v}(x+k,y+l)\right\}, \\ C(k,l) &\triangleq R(k,l) - \mu_v^2, \\ r(k,l) &\triangleq C(k,l)/\sigma_v^2, \end{aligned} \tag{4.18}$$

where $E\{\mathbf{x}\}$ is the expected value of the random variable $\mathbf{x}$. The correlation coefficient is also called coherence function in optics (Goodman, 1975).

Average value

The average value is calculated as:

$$\overline{\mathbf{v}} = \frac{1}{A_w}\int_{x=0}^{X}\int_{y=0}^{Y}\mathbf{v}(x,y)dxdy, \tag{4.19}$$

where A_w $(= XY)$ is the area of window w. The variable $\overline{\mathbf{v}}$ is an unbiased estimator of the mean: $E\{\overline{\mathbf{v}}\} = E\{\mathbf{v}(x,y)\} = \mu_v$. The expected variance of the stochastic variable $\overline{\mathbf{v}}$ is:

$$\sigma^2_{\overline{v}} = E\left\{(\overline{\mathbf{v}} - \mu_v)^2\right\} = E\left\{(\overline{\mathbf{v}})^2\right\} - \mu_v^2 =$$
$$\frac{E\left\{\int_{x_1=0}^{X}\int_{y_1=0}^{Y}\int_{x_2=0}^{X}\int_{y_2=0}^{Y}\mathbf{v}(x_1,y_1)\mathbf{v}(x_2,y_2)dx_1dy_1dx_2dy_2\right\}}{A_w^2} - \mu_v^2.$$

Shifting the expectation operator E, and using Eq. 4.18 then results in:

$$\begin{aligned} \sigma^2_{\overline{v}} &= \frac{1}{A_w^2}\int_{x=0}^{X}\int_{y=0}^{Y}\int_{k=-x}^{X-x}\int_{l=-y}^{Y-y} R(k,l)dkdldxdy - \mu_v^2, \\ &= \frac{\sigma_v^2}{A_w^2}\int_{x=0}^{X}\int_{y=0}^{Y}\int_{k=-x}^{X-x}\int_{l=-y}^{Y-y} r(k,l)dkdldxdy. \end{aligned} \tag{4.20}$$

If the correlation coefficient is equal to the zero-order approximation Eq. 4.13, then:

$$\begin{aligned} \tilde{\sigma}^2_{\overline{v}} = & \frac{\sigma_v^2}{(1+\alpha)A_w^2}[X^2 - (X^2 - Xs_k + s_k^2/4)U(X - s_k/2)] \times \\ & [Y^2 - (Y^2 - Ys_l + s_l^2/4)U(Y - s_l/2)] \\ + \quad & \frac{\alpha\sigma_v^2}{(1+\alpha)A_w^2}[X^2 - (X^2 - X\beta_k + \beta_k^2/4)U(X - \beta_k/2)] \times \\ & [Y^2 - (Y^2 - Y\beta_l + \beta_l^2/4)U(Y - \beta_l/2)]. \end{aligned} \tag{4.21}$$

Variance

The estimated variance in an image window is a stochastic variable:

$$\mathbf{s}^2 = \frac{1}{A_w}\int_{x=0}^{X}\int_{y=0}^{Y}(\mathbf{v}(x,y) - \overline{\mathbf{v}})^2\, dxdy. \tag{4.22}$$

The expected value of the stochastic variable $\mathbf{s}^2$ is:

$$\begin{aligned} \mu_{s^2} &= E\left\{\frac{1}{A_w}\int_{x=0}^{X}\int_{y=0}^{Y}\left(\mathbf{v}^2(x,y) - 2\mathbf{v}(x,y)\overline{\mathbf{v}} + (\overline{\mathbf{v}})^2\right)dxdy\right\}, \\ &= \mu_v^2 + \sigma_v^2 - 2E\left\{\frac{1}{A_w}\int_{x=0}^{X}\int_{y=0}^{Y}\mathbf{v}(x,y)\overline{\mathbf{v}}dxdy\right\} + \sigma^2_{\overline{v}} + \mu_v^2, \end{aligned}$$

where the middle part can be written as:

$$\begin{aligned} 2E\left\{\frac{1}{A_w^2}\int_{x_1=0}^{X}\int_{y_1=0}^{Y}\int_{x_2=0}^{X}\int_{y_2=0}^{Y}\mathbf{v}(x_1,y_1)\mathbf{v}(x_2,y_2)dx_1dy_1dx_2dy_2\right\} \\ = 2\sigma^2_{\overline{v}} + 2\mu_v^2. \end{aligned}$$

The expected value of the estimated variance then becomes:

$$\mu_{s^2} = \sigma_v^2 - \sigma^2_{\overline{v}} \tag{4.23}$$

SNR

The feature SNR is a function of two random variables:

$$\mathbf{snr} = \overline{\mathbf{v}}/\mathbf{s}. \tag{4.24}$$

If the random variable $\mathbf{v}$ has a Rayleigh distribution then $\overline{\mathbf{v}}$ and $\mathbf{s}$ are correlated. Under these conditions the expected SNR can be approximated by (Verhoeven and Thijssen, 1991):

$$E\{\mathbf{snr}\} \approx 1.91(1 + 0.68/N), \tag{4.25}$$

where N is the number of independent samples, or speckles, which can be replaced by $A_w/(s_l s_k)$. Eq. 4.25 can be improved, because the term 1.91 is an approximation of $\mu_v/\sqrt{\mu_{s^2}}$ and does not account for the bias in $\mathbf{s}$, which was also recognized by Dutt et al. (Dutt and Greenleaf, 1995). Using Eq. 4.23 the equation becomes:

$$E\{\mathbf{snr}\} \approx \frac{\mu_v}{\sqrt{\sigma_v^2 - \sigma_{\overline{v}}^2}}(1 + \frac{0.68 s_l s_k}{A_w}), \tag{4.26}$$

where Eqns. 4.20 or 4.21 can be used to estimate $\sigma_{\overline{v}}^2$. Eq. 4.26 assumes that the variance due to IPB is uncorrelated to the mean, which is plausible as they are the result of different processes.

Bibliography

Berkhoff AP, Huisman HJ, Thijssen JM, Jacobs EMPG, Homan RJF. Fast scan conversion algorithms for displaying ultrasound sector images. Ultrason Imag 1994;16:87–108.

Burckhardt CB. Speckle in ultrasound B-mode scans. IEEE Trans Sonics Ultras 1978;25:1–6.

Dutt V, Greenleaf JF. Speckle analysis using signal to noise ratios based on fractional order moments. Ultrason Imag 1995;17:251–268.

Garra BS, Insana MF, Shawker TH, Russell MA. Quantitative estimation of liver attenuation and echogenicity: normal state versus diffuse liver disease. Radiology 1987;162:61–67.

Garra BS, Insana MF, Shawker TH, et al. Quantitative ultrasonic detection and classification of diffuse liver disease – comparison with human observer performance. Inv Radiology 1989;24:196–203.

Gonzalez RC, Wintz I. Digital image processing. Reading, Massachusetts: Addison-Wesley, 1987.

Goodman JW. Statistical properties of laser speckle patterns. Berlin: Springer-Verlag, 1975: 9–75.

Grace A. Optimization toolbox user's guide for use with MATLAB. Natick, MA, USA: The Mathworks, 1992.

Insana MF, Wagner RF, Garra BS, Brown DG, Shawker TH. Analysis of ultrasound image texture via generalized Rician statistics. Optical Engineering 1986;25:743–748.

Kadoya M, Matsui O, Kitagawa K, et al. Segmental iron deposition in the liver due to decreased intrahepatic portal perfusion: findings at MR imaging. Radiology 1994;193:671–676.

Kanematsu M, Hoshi H, Imaeda T, et al. Nonpathological focal enhancements on spiral CT hepatic angiography. Abdominal Imag 1997;22:55–59.

King DL, Lizzi FL, Feleppa EJ, et al. Focal and diffuse liver disease studied by quantitative microstructural sonography. Radiology 1985;155:457–462.

Lafortune M, Madore F, Patriquin H, Breton G. Segmental anatomy of the liver: a sonographic approach to the Couinaud nomenclature. Radiology 1991;181:443–448.

O'Donnell M, Reilly, Jr. HF. Clinical evaluation of the B'-scan. IEEE Trans Sonics Ultras 1985;32:450–457.

Oosterveld BJ, Thijssen JM, Hartman PC, Romijn RL, Rosenbusch GJE. Ultrasound attenuation and texture analysis of diffuse liver disease: methods and preliminary results. Physics Med Biol 1991;36:1039–1064.

Oosterveld BJ, Thijssen JM, Verhoef WA. Texture of B-mode echograms: 3D simulations and experiments of the effect of diffraction and scatterer density. Ultrason Imag 1985;7:142–160.

Oppenheim AV, Schafer RW. Digital signal processing. Englewood Cliffs, NJ, USA: Prentice-Hall, 1975.

Papoulis A. Signal analysis. Singapore: McGraw-Hill, 1977.

Papoulis A. Probability, random variables, and stochastic processes. Singapore: McGraw-Hill, 1991.

Parker KJ, Asztely MS, Lerner RM, Schenk EA, Waag RC. *In vivo* measurements of ultrasound attenuation in normal or diseased liver. Ultrasound Med Biol 1988;14:127–136.

Raeth U, Schlaps D, Limberg B, et al. Diagnostic accuracy of computerized B-scan texture analysis and conventional ultrasonography in diffuse parenchymal and malignant liver disease. J Clin Ultrasound 1985;13:87–99.

Rettenmaier G. Fokale leberveränderung. Chapter 3 in: Rettenmaier G and Seitz K, eds. Sonographische differentialdiagnostik. Weinheim, Germany: VCH Publishers, 1990.

Romijn RL, Thijssen JM, Beuningen GWJ. Estimation of scatterer size from backscattered ultrasound: a simulation study. IEEE Trans Ultrason Ferroelectr Freq Control 1989;36:593–606.

Verhoeven JTM, Thijssen JM. Improvement of lesion detection by echographic image processing: signal-to-noise-ratio imaging. Ultrason Imag 1991;13:238–251.

Wagner RF, Smith SW, Sandrik JM, Lopez H. Statistics of speckle in ultrasound B-scans. IEEE Trans Sonics Ultras 1983;30:156–163.

Chapter 5

Adaptive texture feature extraction with application to ultrasonic image analysis

5.1 Introduction

Texture[1] analysis has many applications in image processing where single pixel statistics are inadequate. For example, evaluating medical ultrasonic images for diagnostic reasons requires good texture discrimination. A skilled ultrasound-technician uses grey-level as well as texture in an ultrasonic image to identify a lesion (see Fig. 5.1). The human visual system is very well capable of discriminating between different natural textures, although there is evidence that some higher order textures cannot be discriminated (Julesz et al., 1973). A computer vision system using adequate texture feature extractors could be capable to improve on human performance. The intended role of this system is to assist the ultrasound-technician by highlighting those areas that have non-normal tissue texture.

The selection of texture features affects the performance of the system, and it is often difficult to chose an adequate set of features, especially in limited data environments such as medical imaging (Oosterveld et al., 1993). A strategy is required to get a limited set of discriminative texture features, because it is well known that if the number of features is increased beyond a certain limit the test set performance will decrease (Foley, 1972; Fukunaga, 1989), also called peaking phenomenon (McLachlan, 1992). This limit depends on the dataset size, the complexity of the classification rule (Raudys and Jain, 1991), and the correlation between the training samples (Fu, 1990). In limited datasets the number of features should be below this limit. However, reducing the number of features may decrease performance, if there is not a small feature set that captures all information. Therefore, a limited number of features is required, that contain as

---

[1] This chapter is based on the publication: H.J.Huisman, J.M.Thijssen *Adaptive texture feature extraction with application to ultrasonic image analysis* to be submitted

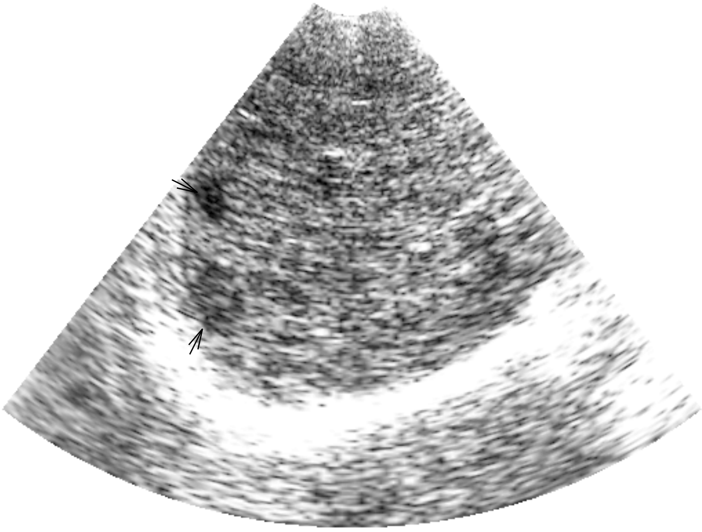

Figure 5.1 Echographic image showing one transverse section through the liver. The parenchyma is bounded by the skin at the top and the bright diaphragm at the bottom. Two small hypo-echoic metastases are visible (arrows) within the parenchyma at the left hand side.

much discriminative information as possible.
Two strategies will be distinguished to get a limited set of discriminative features (see Fig. 5.2):

- feature selection from a large set of predefined texture features,
- a limited set of adaptive texture features extractors (ATFE) that are directly tuned to the underlying problem.

Traditional feature selection strategies use a training set of images to select a subset from the predefined features (Kittler, 1986; McLachlan, 1992). For this strategy to perform well, the initial feature set should already contain a small set of discriminative texture features, each extracting distinct discriminatory information. Many predefined texture feature extractors are available (Ohanian and Dubes, 1992; Oosterveld et al., 1991). Although such features can discriminate various textures, they are often not specifically designed for the underlying problem or they assume a very simple (e.g. linear) model. As a result the discriminatory power of each feature can be low, necessitating the number of selected features to increase. Furthermore, these fixed features can be highly correlated (Thijssen et al., 1993), which requires even more features to

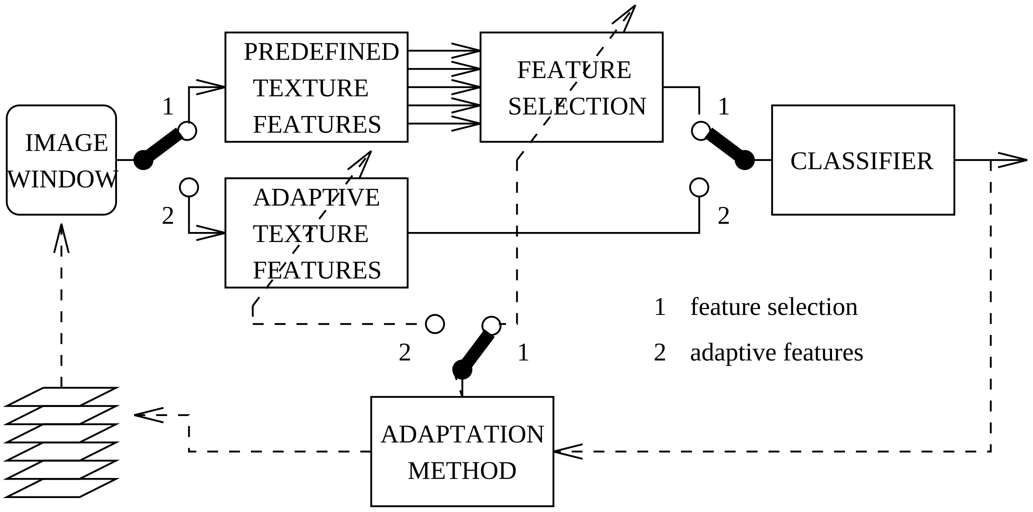

Figure 5.2 Texture analysis system showing two possible feature extraction strategies. 1. Calculate predefined features and select a reduced set. 2. Directly train an adaptive texture feature extraction method. The dashed lines are active during training: windows from a training set are presented to the system and the performance is estimated from the classifier output. The adaptation method tries to optimize classifier performance.

increase discriminatory power. The feature selection strategy has been applied by numerous researchers within the ultrasonic tissue characterization field and an operational set of features has not yet emerged.

Adaptive texture features extractors (ATFEs) have an adaptive extraction method (see Fig. 5.2) that allows for the features to be tuned to the problem at hand. If the ATFE's adaptable calculation method is general enough (i.e. including non-linear transformations), then it can be trained to produce features each representing one image texture (or tissue type). Consequently, a limited number of discriminative features results.

Adaptive texture features already exist. A technique incorporating linear filter masks with adjustable coefficients has been shown to discriminate textures (Unser, 1986) and can also be trained to correlate with perceptual judgment (Benke et al., 1988). This technique, which is analogous to template matching, is limited to linearly separable textures. An adaptive method that is capable of performing a wide range of non-linear transformations is the artificial neural network (ANN). This chapter reviews the application of the ANN in this field and work out a general strategy by which ANNs may be used as ATFE. An operational description of the ATFE method is presented and its performance on synthetic ultrasonic images will be compared with existing methods.

5.2 ANN-ATFE Theory

An artificial neural network operates as an ATFE if its input neurons are directly connected to the pixels in an image window. Repeated presentation of windows with known tissue type and an adequate learning scheme should adapt the weights in the ANN such that the output of the network will be one or more features that discriminate between windows of different types. This strategy, which will be referred to in this chapter as “brute force”, has two disadvantages that make it less applicable to texture discrimination. First, the number of input neurons is large even for rather small window sizes (e.g. 25 neurons in a 5x5 window). Secondly, the transformation to be learned by the network may be highly non-linear. This will result in a complex ANN with two hidden layers (Hertz et al., 1991, p.142) (Bishop, 1995, p.128). Thus, the “brute force” approach results in large networks with many weights, and requires many training windows. A rule of thumb is to have at least $N_{weights}/\epsilon$ training windows for a generalization error smaller than ϵ (Hertz et al., 1991, p.156) (Bishop, 1995, p.380). Thus for a 10% generalization error, a 5x5 window, and a 25-50-50-2 network, the number of training windows should be at least 38500. In other words, about 100 images of 100x100 pixels are required, which need to be fully segmented. Even worse, the number of images will be substantially higher as the rule of thumb was developed for a 2-layer network. An operational method would require a smaller neural network.

To reduce the ANN size, Jain et al. (Jain and Karu, 1996) used a reduction strategy whereby not all pixels in the image window are input to the network. They did not show how their selection affects performance. Another strategy is to use higher-order neural networks (HONN) (Lee et al., 1986). In a HONN the layer of input neurons is extended with higher order product terms. The hidden neurons thus have the ability to directly learn higher-order relations, the advantage being a decrease in the number of hidden layers (Giles and Maxwell, 1987). As the number of layers decreases, the complexity of the network decreases, making it easier to train on lesser data. However, due to a combinatoric explosion of the number of higher order product terms, this HONN approach is not feasible. The HONN strategy can be made feasible by taking into account the spatially invariant image properties. For example, if translation invariance holds, then the set of second order terms can be reduced to an autocorrelation function (Giles and Maxwell, 1987). This idea will be generalized even further by using invariant higher order functions (IHOF). It was already shown for ultrasonic tissue characterization that the autocorrelation function in this application can be useful to discriminate between different tissue types (Huisman and Thijssen, 1995). A wide variety of IHOFs, such as the grey-value histogram, autocorrelation function, and power spectrum, seem applicable to the ultrasonic tissue characterization field.

A few other ANN-ATFEs appeared in literature that follow parts of the previously described approach. Schmidt et al. (Schmidt and Davis, 1993) used the HONN paradigm and recognized a “preprocessing step” as a front-end to the network, but they did not generalize to IHOF. Stathaki et al. (Stathaki, 1995), Lu et al. (Lu and Xu, 1995) calculated a set of auto regressive coefficients and used them as the input to a neural network. More specific to ultrasound, the frequency-dependent attenuation and backscatter coefficients (both known to carry information in ultrasound tissue characterization) have been fed into a neural network (Botros, 1992; Zatari et al., 1994).

Besides the general idea using an IHOF also a sampling reduction will be applied, because the

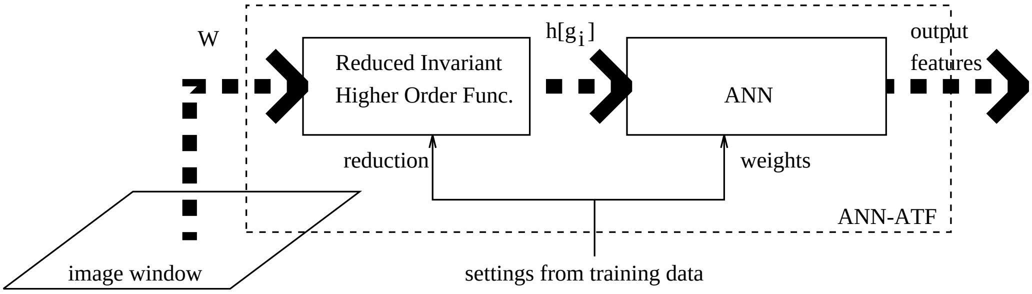

Figure 5.3 Operational ANN-ATFE scheme. The reduction settings and the weights of the neural network are obtained in a prior training phase.

IHOF can still be calculated at a high resolution. For example, a grey-value histogram IHOF in an 8-bit image can be calculated at 256 levels. However in a 5x5-window this will result in a poorly estimated histogram with many empty bins. The sampling reduction equally applies to other IHOFs. Previously cited ANN-ATFE methods used a heuristic reduction strategy (e.g. (Botros, 1992; Zatari et al., 1994) manually selecting part of a spectrum, or averaging 4 bins into 1). Selecting the number of bins and how their boundaries are located may very well affect performance. In the next section the ANN-ATFE method is described with a general IHOF reduction strategy.

5.3 Method

The ATFE is schematically shown in Fig. 5.3. It operates on a local (2m+1) x (2n+1) image window $W_{p,q}$ at position (p,q) in image $\mathcal{I}$:

$$W_{p,q} = \begin{bmatrix} \mathcal{I}(p-m,q-n) & \dots & \mathcal{I}(p-m,q+n) \\ \vdots & \mathcal{I}(p,q) & \vdots \\ \mathcal{I}(p+m,q-n) & \dots & \mathcal{I}(p+m,q+n) \end{bmatrix}, \tag{5.1}$$

where pixel $\mathcal{I}(p,q)$ is the grey-value at central position p,q. In the operational phase, the (scanning) window grey value matrix $W_{p,q}$ is used to calculate a reduced invariant higher order function (IHOF) $h[g_i]$, where g_i is the translation invariant property (e.g. correlation distance, frequency). The reduced elements are connected to the input neurons of an ANN, which has been trained to convert these inputs into discriminative features at its output neurons. One output feature is used for each tissue type. The value at one output neuron can be used as the grey-value at position (p,q) of a new, feature image. Each output neuron produces its own feature image. Fig. 5.5 shows example input images and Fig. 5.7 shows the output images after filtering with the trained ANN-ATFE using one of the output neurons.

In the training phase, the reduction strategy and the neural network training algorithm use a training set of windows S of known tissue type:

$$S = \{S_1, S_2, \dots\}, \tag{5.2}$$

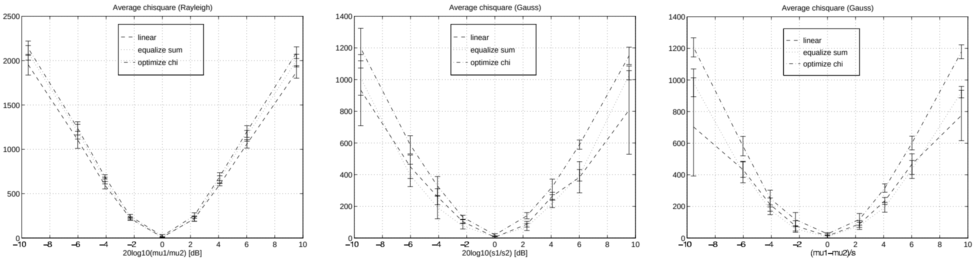

(a) Rayleigh pdf (b) Gaussian pdf $\mu_1 = \mu_2$ (c) Gaussian pdf $\sigma_1 = \sigma_2$

Figure 5.4 χ^2 values for three types of reduction strategies in three different situations. High χ^2 values indicate good discriminatory capacity of the reduced IHOFs. If the IHOFs are statistically identical (equal tissue types), then all three strategies converge to the same minimum.

where S_j is a set of windows labeled tissue type j. Training is carried out in two steps: first the reduction method, then the ANN.

As will be shown further on, the training of the reduction method is much faster when it first estimates the average IHOF for each tissue type by averaging over all available training windows.

$$\overline{h}_j(g) =< H(W_{j,k}) >_{W_{j,k} \in S_j}, \tag{5.3}$$

where $H()$ is the selected IHOF transformation.

As explained in the previous section, the variable g can be quantified into a large number of levels (bins) or even be continuous and thus requires reduction. At this point it is assumed that it will be reduced to $nbin$ bins, and first attention is given to finding the boundaries of the $nbin$ bins. The reduced IHOF $\overline{h}_j[g_i]$ is estimated from Eq. 5.3 as follows:

$$\overline{h}_j[g_i] = \int_{\kappa_i}^{\kappa_{i+1}} \overline{h}_j(g) dg, \tag{5.4}$$

where κ_i is the lower boundary of bin i. The $nbin + 1$ boundaries comprise the boundary vector $\vec{\kappa} = [\kappa_1, \ldots, \kappa_{nbin+1}]$.

Good boundaries preserve the discriminative information that is contained within the reduced IHOFs. In analogy to feature selection, a probabilistic distance can be used as an evaluation criterion (Kittler, 1986). A well known probabilistic distance is the χ^2-distance (Papoulis, 1991). In theory, the χ^2-distance is an asymmetric distance between a measured histogram and a theoretical pdf. With a slight adaptation the following symmetric version is obtained:

$$\chi^2 = \sum_{i=1}^{nbin} \frac{(\overline{h}_1[g_i] - \overline{h}_2[g_i])^2}{0.5(\overline{h}_1[g_i] + \overline{h}_2[g_i])} \tag{5.5}$$

With an evaluation criterion at hand, the search for the boundary vector $\vec{\kappa}$ is reduced to an optimization problem:

$$\vec{\kappa}_{opt} = \arg\max_{\vec{\kappa}}(\chi^2(\vec{\kappa})) \tag{5.6}$$

The κ-vector that results in the largest χ^2-value is selected. The `constr` function from the Matlab Optimization Toolbox (Grace, 1992) was used. This is a constrained optimization method, that allows for an efficient search through realistic solutions.

In the operational phase, when a single window is presented to the ANN-ATFE, the reduced IHOF is obtained as follows:

$$h_j[g_i] = \int_{\kappa_i}^{\kappa_{i+1}} H(W_{j,k})dg \tag{5.7}$$

Now it is clear why Eq. 5.4 and Eq. 5.3 were used, because for each bin-vector that is evaluated during optimization, Eq. 5.7 would need to be averaged over all windows, whereas Eq. 5.4 directly estimates the reduced average IHOF.

At this point it will be known how to obtain the optimum κ-vector, if $nbin$ is known. The optimum $nbin$ depends on the size of the dataset and the complexity of the IHOFs. Moreover, $nbin$ determines the size of the neural network. To determine $nbin$ the following procedure is used: train multiple ANN-ATFEs on the training set with a number of settings for $nbin$. The one with the best performance on an independent test set is selected.

The optimized boundary selection procedure was evaluated by comparing it with two other procedures. Linear boundaries are obtained when using equally spaced bins between minimum and maximum. The second procedure selects bins such that the sum $\sum_j \overline{h}_j[g_i]$ is a constant, it equalizes the number of occurrences within each bin for all tissue types. Thus three χ^2 values are produced: χ^2_{opt}, χ^2_{lin}, and χ^2_{equ}.

The χ^2 values were calculated in three different situations with $nbin = 5$. In each situation two IHOFs $h_1(g)$ and $h_2(g)$ are each estimated from 1000 samples drawn from a theoretical pdf with different parameter settings. In situation 1 a Rayleigh pdf ($p(x) = R(\mu)$) was used, and $h_1(g)$ had $\mu_1 = 1$, and $h_2(g)$ has its mean value (μ_2) varied (Fig. 5.4a). As expected calculated χ^2 values have a minimum at $\mu_1 = \mu_2$ (= 0 dB). In situation 2 Gaussian pdfs ($p(x) = N(\mu, \sigma)$) were used, the settings were: $\mu_1 = \mu_2 = 0$, $\sigma_1 = 1$, and σ_2 was varied (Fig. 5.4b). The third situation also used Gaussian pdfs, but μ_2 was varied, while setting: $\mu_1 = 1$, $\sigma_1 = \sigma_2 = 1$ (Fig. 5.4c). Each setting was repeated 5 times to obtain the mean and standard deviation of the χ^2 values.

Fig. 5.4 clearly shows that the χ^2 values are symmetrical. Furthermore, the optimized bin distribution results in higher χ^2 values than the other two bin selection strategies, but they all converge to the same minimum if no discriminatory information is present in the selected IHOF. The χ^2_{opt} curves are smooth and remain at or above the other curves even at very low χ^2 values. This is possible only when using the mentioned optimization procedure. Many other, simpler optimizations routines were tried, but they did not converge, or the algorithm collapsed at low χ^2 values.

The χ^2 value facilitates selection of the IHOF, because the χ^2-curve has a minimum which occurs when the IHOFs have identical probability densities. This minimum level is the same for any

Training method	Break point [epochs]	[s]	PC [%]
LM	7	1800	93
FBP	85	5000	93

Table 5.1 Comparison of neural network training methods: Levenberg-Marquardt (LM) and fast back propagation (FBP). PC=percentage correctly classified pixels, execution time on SUN-Sparcstation20

IHOF, and depends only on the number of samples and $nbin$. The minimum level is useful when evaluating an IHOF. If the IHOF results in χ^2 values close to this level, then this indicates that the IHOF has low discriminative capabilities.

Returning to Fig. 5.3, the second step in the ANN-ATFE is an artificial neural network that is fed with the reduced IHOF $h_j[g]$ estimated with Eq. 5.7 and trained to predict the tissue type:

$$\vec{\psi} = \text{ANN}(w_1, w_2, h_j[g]), \tag{5.8}$$

where w_1 and w_2 are two weight matrices in between the three layers of neurons. The ANN is a fully connected feed-forward neural network with hyperbolic tangent activation functions. The number of input neurons is $nbin$. The hidden layer size is $2.nbin$ neurons, which is common in neural network literature (in the next section different settings are evaluated). The number of output neurons is equal to the number of tissue types. So, for two tissue types and $nbin = 5$, a 5-10-2 network is used. The neural network is trained to set the output neuron j to 1 if a window from S_j is presented and all other output neurons to -1.

The selection of an adequate training algorithm appeared to be non-trivial. Many training algorithms exist (Bishop, 1995; Hertz et al., 1991), but performance differences are large. In earlier experiments on this topic it was shown that the well-known steepest descent training method did not always converge (Huisman and Thijssen, 1995), especially when training the network in low contrast situations. Two other training algorithms were compared: the first, fast backpropagation (FBP), is an extension of the steepest descent with an adaptive learning rate, and a momentum term (`trainbpx`,(Grace, 1992)) and the second is the Levenberg-Marquardt (LM) method (`trainlm`, (Nørgaard, 1995)). Table 5.1 shows the result of training with both algorithms on low-contrast, simulated ultrasound images (7-14-2 network, $nbin$=7, 7x7 image window, 10 images with tissue type 1 = 20 and type 2 = 15 scatterers/pulse volume, see Appendix). Both algorithms start training with the same sum square error (SSE) and percentage correctly classified pixels (PC). The clearly visible break point was determined from the PC training curve. Table 5.1 shows that both algorithms converge, but the LM algorithm does so in only 7 epochs! In comparison, the steepest-descent algorithm may take as many as several 1000s of epochs to train. A minor disadvantage of the LM algorithm is the time required to train 1 epoch, which is about four times as long as the FBP algorithm. LM was chosen, because it is faster, and known to be a very stable algorithm (Nørgaard, 1995).

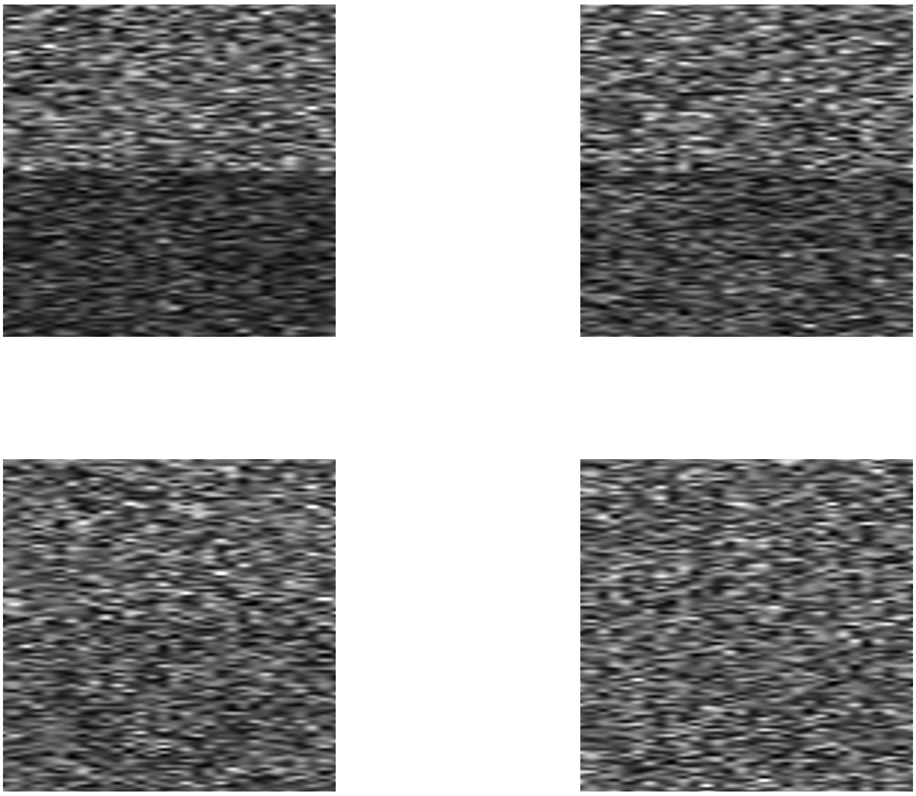

Figure 5.5 Examples of simulated ultrasonic images. In all images the top half was simulated at scatterer density 20 and the lower half at: 6 (top left), 10 (top right), 14 (bottom left), 18 (bottom right). The images have been linearly interpolated which is equivalent to the oversampled B-mode video images in ultrasound.

5.4 Experiments

The ANN-ATFE method was tested as described in the previous section in a number of experiments. Two sets of 10 images with 30 x 30 statistically independent pixels (or speckles in ultrasound) were simulated (see Appendix). An image comprises an upper (tissue type 1) and a lower (tissue type 2) half, each simulated with its own scatterer density (see Fig. 5.5). Varying the scatterer density affects the grey-value distribution and to a less extend the speckle size (Oosterveld et al., 1985) (which can be analyzed using the auto covariance function). As the pixels were independent, the speckle size is constant, and the selected IHOF is the grey-value histogram. One set of 10 images was used for training, the other set was used for testing. Training was carried out on non-overlapping, single tissue type windows. For comparison two other texture features sets were simultaneously calculated on the same windows, they are: mean, standard deviation, skewness and kurtosis (FF4) and a subset of only the mean and standard deviation (FF2).

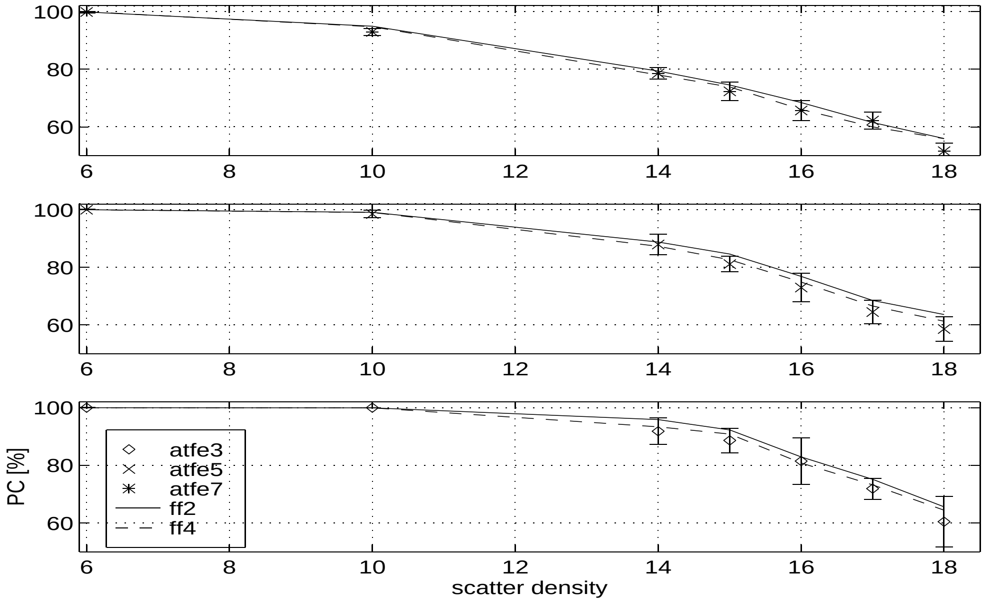

Figure 5.6 Percentage correctly classified pixels (PC) using ANN-ATFE, or fixed features (FF2, or FF4) in a high scatterer density situation. Three window sizes were used: 5x5, 7x7, and 10x10. The x-axis represents the scatterer density of tissue type 2.

The ANN-ATFEs or the fixed features (FF2 or FF4) are connected to a classifier (see Fig. 5.2), which tries to predict the underlying tissue type. The k nearest neighbor (kNN) classifier (McLachlan, 1992) was used, because it is a powerful, non-parametric classifier equally capable of classifying the output from the ANN-ATFE as well as from the fixed features. The classifier is trained on the training set, and the performance is estimated from the test set by calculating the percentage of pixels which is correctly classified (PC). The classification of each window into one of two classes could also be applied to produce a binary segmentation image (see Fig. 5.9).

A number of parameters were varied to compare the fixed features with the ANN-ATFEs under varying conditions. First, in each experiment three window sizes were used: 5x5, 7x7, and 10x10. They represented a range of feasible texture window sizes. Second, the scatterer density of tissue type 1 remained fixed during an experiment, but the other tissue type was simulated with a range of scatterer densities. Each experiment was replicated ten times to get a mean value of PC, and its standard deviation.

5.4.1 High scatterer density range

In the first experiment the scatterer density of tissue type 1 was set to 20 scatterers per pulse volume, and the other was varied between 6 and 18. Situation 20-6 represents the highest, and 20-18 the lowest contrast situation (see Fig. 5.5). First $nbin$ was determined for each window

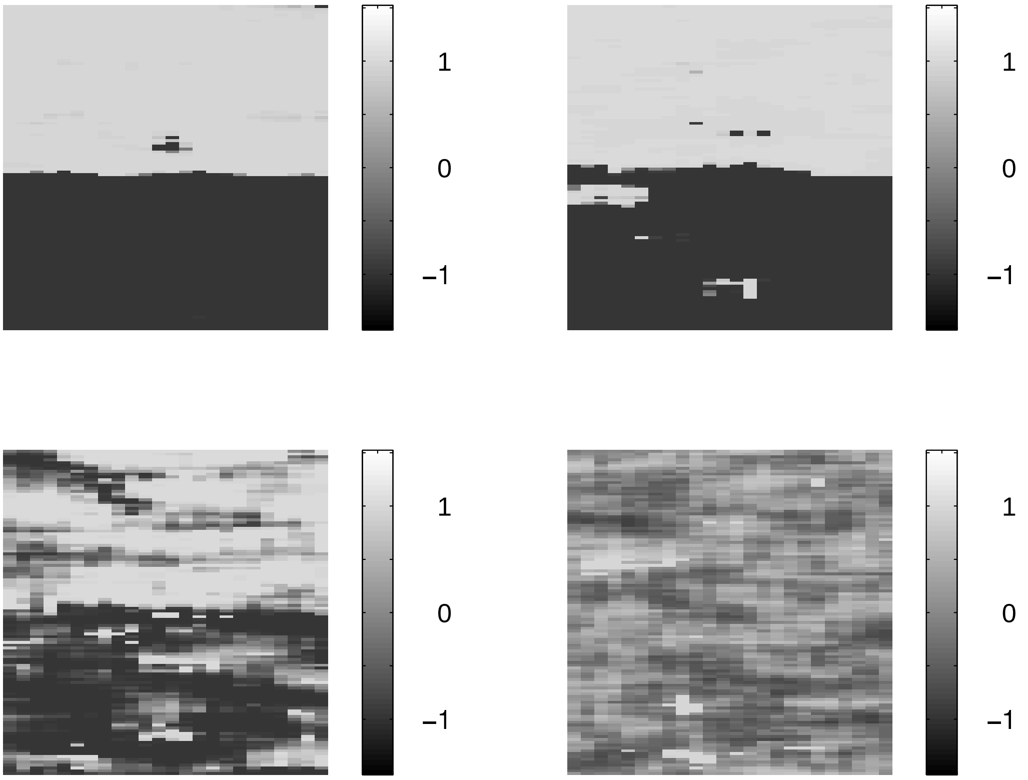

Figure 5.7 Output images after filtering the example images from Fig. 5.5 with the accompanying (trained) ATFE using 7x7 windows. Only one of output features is shown.

size. To do so, the average performance was determined at low contrast (14-18) relative to the performance of the FF2 feature set. Table 5.2 shows the results, where the notation ATFEX is used to indicate that *nbin* was set to X. The selected *nbin* values are: 7, 5 and 3, for window sizes 5x5, 7x7, and 10x10 respectively. Output images after filtering with the trained ANN-ATFEs are shown in Fig. 5.7 and the performance results are shown in Fig. 5.6. The solid line and the dashed line represent the performance of two (FF2) and four (FF4) fixed features sets, respectively. As expected, an increasing scatterer density of tissue type 2 results in a decrease of scatterer density difference, thus the performance will decrease which is also visible from Fig. 5.7. The ANN-ATFE performance is indicated by the circles, where the standard deviation is indicated by the error bars.

This experiment shows that the ANN-ATFE method is feasible and able to discriminate low contrast image regions. This is an improvement on the previous approach (Huisman and Thijssen, 1995) that used the gradient-descent ANN training algorithm and was difficult (if not impossible) to train at low contrast. The ANN-ATFE is also capable of operating at small data sets and

feature set	Window size 5x5	7x7	10x10
FF4	-1.2 (0.4)	-1.9 (0.1)	-1.8 (0.2)
ATFE3	-3.3 (0.7)	-4.3 (0.9)	-3.5 (0.6)
ATFE5	-2.3 (0.6)	-3.4 (0.7)	-4.5 (0.6)
ATFE7	-1.9 (0.9)	-3.4 (1.0)	-4.4 (1.1)
ATFE9	-1.9 (0.9)	-3.4 (1.0)	-4.4 (1.1)

Table 5.2 Average performance of the ATFE and FF4 feature sets relative to the FF2 set ($\Delta PC = PC_{FF2} - PC_{XX}$) in experiment 1. Number between brackets is the estimated standard deviation.

feature set	Window size 5x5	7x7	10x10
FF4	-1.2 (0.4)	-1.2 (0.8)	-4.1 (2.0)
ATFE3	-2.3 (0.9)	-2.1 (0.5)	-4.3 (0.8)
ATFE5	-1.2 (0.4)	-1.9 (0.9)	-4.3 (1.4)
ATFE7	-1.3 (0.1)	-0.9 (1.5)	-5.6 (1.9)
ATFE9	-2.3 (0.9)	-4.0 (1.7)	-6.3 (2.6)

Table 5.3 Average performance of the ATFE and FF4 feature sets relative to the FF2 set ($\Delta PC = PC_{FF2} - PC_{XX}$) in experiment 2. Number between brackets is the estimated standard deviation.

accompanying small image windows, which is the result of using the IHOF reduction scheme. In this experiment the ANN-ATFE does not improve upon the selected fixed features, because it is known to be very well discriminable using low order gray value moments (Oosterveld et al., 1985; Verhoeven and Thijssen, 1991). However, the small decrease in performance of the ANN-ATFE indicates that it is capable of extracting near optimal features. In practice, the underlying tissue structure changes are more complicated and the optimal features are not known in advance, thus the ANN-ATFE can then very well improve upon the fixed feature strategy.

5.4.2 Low scatterer density range

The first experiment was repeated in the low scatterer density range, which is a realistic situation. It is well known (Jakeman, 1984) that under these conditions the grey-value histogram shape analysis requires higher order moments. It requires a more detailed analysis of the selected IHOF (histogram) and hence seems appropriate for the ANN-ATFE. Again $nbin$ is selected for each window size by evaluating performance at different values of $nbin$. The results are shown in table 5.3. The selected $nbin$ for the 5x5, 7x7, and 10x10 window were respectively: 5, 7, and 3. The performance of the feature sets is shown in Fig. 5.8.

Comparing Figs. 5.6 and 5.8, and tables 5.2 and 5.3, the performance differences between FF2, FF4, and ANN-ATFE are decreased in the second experiment. It shows that discriminatory information is present in the higher order moment terms of the IHOF, and the ANN-ATFE method

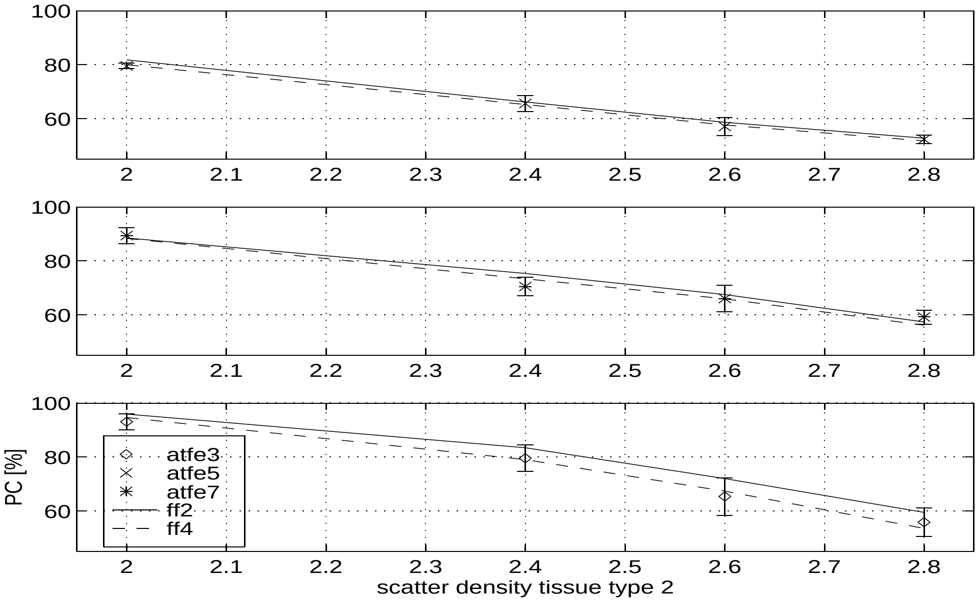

Figure 5.8 Percentage correctly classified pixels (PC) using ANN-ATFE, or fixed features (FF2, or FF4) in a low scatterer density situation. Three window sizes were used: 5x5, 7x7, and 10x10. The x-axis represents the scatterer density of tissue type 2.

is capable to extract this information. This is true if the number of windows is not too low. Although the non-overlapping 10x10 windows are bigger and individually provide more information, the low number of training windows affects ATFE as well as FF4 performance. This is not surprising, because when analyzing increasingly higher order effects the amount of training data should also increase. For the FF4 feature set the increase is required to train the increased complexity classifier. For the ANN-ATFE it is required to train a larger and more complex neural network. Thus no matter what type of feature extractor is used, the analysis of higher order moments requires more training image data.

5.4.3 Calcifications

In this third experiment a non-linear problem is created by simulating lesions containing calcifications. A small calcification results in an overflow situation at the corresponding position in the image, due to the high reflection coefficient. They appear as, so called, hard speckles, i.e. single independent pixels with high grey-value, because of the limited range of the display (high values are clipped) and the small size of a calcification. Fig. 5.9 shows an example lesion containing calcifications. In this simulated example both tissue types had scatterer density 8. The number of calcified (i.e. overflown) speckles was 10%. It is clear that any texture feature extraction algorithm capable of discriminating non-linear textures should be capable of detecting such regions.

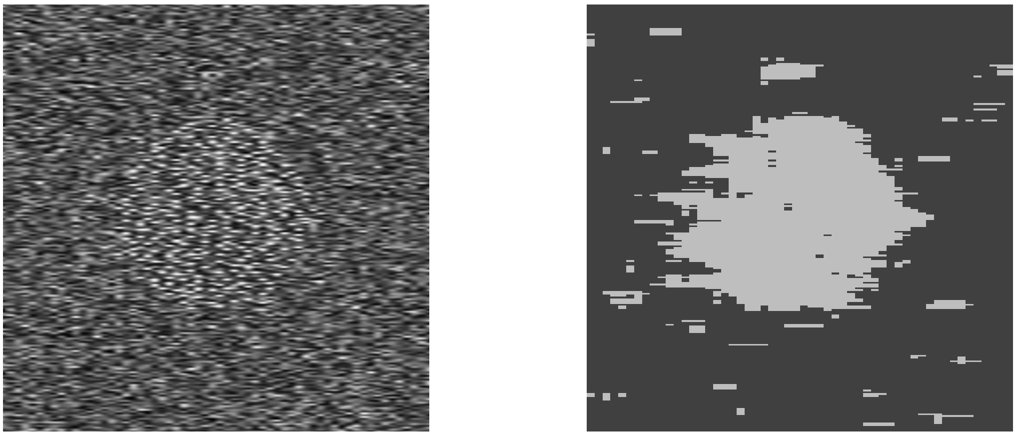

Figure 5.9 The left image shows a synthetic ultrasonic image with a circular lesion containing calcifications. The right image shows the classification of each pixel using the output of a trained ATFE.

Train and test sets were generated as in the previous examples and the ANN-ATFE was trained with $nbin = 3$ using 5x5-windows. Next the three sets of features (FF2,FF4,ATFE) were calculated in the test set. The mean classification performances of this experiment are: p_{ATFE}=85.4 (0.95), p_{FF2}=83.8 (0.8), and p_{FF4}=84.8 (1.0)%, where the number between brackets is the standard error of the mean (10 repeated experiments). The classification is also shown in Fig. 5.9. These results show that this problem is non-linear indeed, it requires higher order terms in the analysis, because the FF2 feature set performs significantly less than the other two sets. The ANN-ATFE method is capable of capturing the non-linearity in its extracted features required to successfully discriminate this problem. Furthermore, ANN-ATFE does so in only two features, whereas four higher order moment terms were required to obtain about the same performance.

5.4.4 Performance fluctuation sources

The performance of a feature extractor is estimated from the mean of several, repeated experiments. Although the data in one experiment was simulated with the same settings, repeated results may fluctuate due to different realizations of the training and data set. This is true for the fixed features as well as the ANN-ATFE. However, an ANN-ATFE may have an extra source of fluctuations because an ANN is trained from random initialized weights.

To quantify the source of the fluctuations the high scatterer density experiment (20-15) was repeated. 10 sets of 10 training and 10 test images were simulated. The percentage correctly classified pixels was estimated in the test set for three feature sets. The mean performance was 85.4, 82.5, and 82.3% for FF2, FF4, and ANN-ATFE respectively. The estimated variance on both FF2 and FF4 performance is 6.9 and for the ANN-ATFE this is 16.3. To quantify the contribution due to ANN initialization the ANN-ATFE was trained 10 times on each simulation resulting in 100 performance estimates. The average variance due to the ANN initialization was 3.1. The ANN initialization effect does not fully account for the increase in variance, the remaining difference

#hidden layers	Window size		
	5x5	7x7	10x10
nbin	77.5	83.5	91.5
2*nbin	78	84	91.5
4*nbin	77.5	83.5	91.5

Table 5.4 Effect of variations of the number of neurons in the hidden layer in the ANN on the percentage correctly classified pixels.

(16.3-6.9-3.1=6.2) should be attributed to the IHOF reduction method.

5.4.5 Hidden layer size

In the Method section the number of neurons in the hidden layer of the ANN was chosen to be $2.nbin$. The first experiment was repeated with scatterer densities 20 and 15 and the number of neurons in the hidden layer was varied. Table 5.4 shows that varying the number of neurons in the hidden layer of the ANN does not have a large effect on the percentage correctly classified pixels. This experiment shows that the general rule of using $2 * nbin$ neurons in the hidden layer in the method leads to satisfactory results.

5.5 Discussion

An adaptive texture feature extraction method using an artificial neural network (ANN-ATFE) has been developped. The method extends existing strategies by using reduced invariant higher order functions (IHOF). The IHOF selection allows the user to incorporate prior knowledge: an advantage over the often criticized “black-box” approach of neural networks. The IHOF reduction reduces the neural network size to allow the ANN-ATFE to be used on small data sets. The indicated IHOF reduction optimization method as well as the neural network training method ensure robust operation. All ANN-ATFE parameter settings are well described and need no heuristic user fine tuning.

The ANN-ATFE is capable of extracting a minimal set of nearly optimal features. In the synthetic examples the optimal features were known and the ANN-ATFE performance under various conditions was only slightly worse than this optimal feature set. In practice the optimal feature set is often unknown, and if good fixed features are not available, or the selected fixed feature set is sub-optimal, then the ANN-ATFE may very well produce better features.

The ANN-ATFE is capable of generating non-linear feature extractors. The method was tested on an example requiring non-linear analysis of the IHOF to discriminate two tissues. Discrimination clearly improved when using two extra higher order moment terms. The ANN-ATFE still produced only two features but has equal performance to the extended feature set. This confirms that using artificial neural network techniques in the ATFE method enables it to discriminate linear as well as non-linear textures.

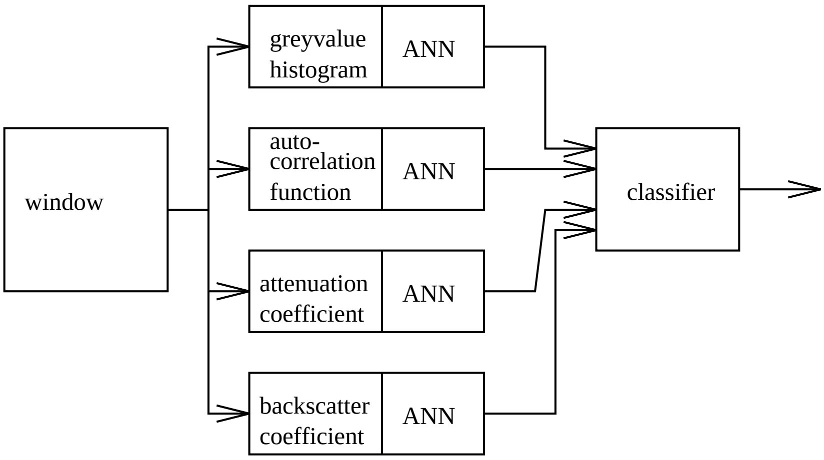

Figure 5.10 Multiple ANN-ATFEs for ultrasonic tissue characterization

The selected optimization method and the neural network training methods perform well even at low contrast conditions. This apparently trivial property could only be achieved by the use of the Levenberg-Marquardt or the fast-backpropagation training algorithms. These algorithms clearly outperformed other, simpler methods such as steepest-descent, especially in low-contrast image analysis problems.

Repeated estimation of the performance of ATFE showed an increase in fluctuations compared to using fixed feature. The main cause of increase is the IHOF reduction method. Although this method is simply expressed as Eq. 5.6, it was found that it is very important to have an optimization method capable of performing constrained search, because unconstrained search algorithms did not always come up with realistic solutions. Furthermore, the trick is to find good constraints in the search space. Fine tuning these restrictions and/or extending the cost function used in the iterative optimization may very well decrease the fluctuations. The smaller source of fluctuations due to ANN initialization may be decreased using a method with repeated training, known as *ensemble learning* (Bishop, 1995, p.432).

The ANN-ATFE strategy allows for the incorporation of prior knowledge. For ultrasound tissue characterization a scheme is proposed which is depicted in Fig. 5.10. Four well-known IHOFs are selected that cover a wide variety of diagnostically relevant phenomena described in literature (Thijssen, 1992). For a two-class problem this system would produce only 8 features, while being capable of capturing non-linear discriminatory information from all four IHOFs.

Appendix A: Simulation of ultrasonic images

A simple ultrasonic image simulator is used that produces B-mode images with statistically independent pixels (speckle size = 1 pixel). The simulator uses a fixed setup of a diffraction-less transducer (plane waves) and a 3D tissue medium without attenuation. This physically resembles imaging a focal depth slice (C-scan), where the transducer translation increments are large enough to obtain independent samples. The medium contains point scatterers that produce the backscattered echoes. The only parameter which is adjustable is the scatterer density expressed as the effective number of scatterers within the acoustic pulse volume. This physical tissue parameter is thought to be one of the parameters that is modified by pathologic changes (Oosterveld et al., 1991).

The following is the core source code (92m, 1992, Matlab) that generates a simulated image in the variable `env`.

```
nscat = round(30*nscateff);
for line=1:nline,
   x = 6*(-0.5+rand(nscat,nsamp));
   y = 6*(-0.5+rand(nscat,nsamp));
   z = 6*(-0.5+rand(nscat,nsamp));
   tmp=-0.5*(xˆ.2+yˆ.2+zˆ.2)+j*2*pi*z;
   env(line,:) = abs(sum(exp(tmp)));
end;
```

The variables `nline`,`nsamp`, `nscateff` are the input parameters. For each sample in each line `nscat` scatterers are uniformly generated in a cubic volume (6x6x6 mm^3), assuming a unit length of 1 millimeter [mm]. A 3D Gaussian pulse volume ($\sigma_{pulse} = 1[mm]$) is simulated at the center of the cubic volume. The effective (-6dB) pulse sample volume is about $1/30$ of the cubic volume, thus `nscat = 30*nscateff`. The backscattered echoes are received by a phase sensitive planar transducer. Units are normalized such that the effective pulse length is 2.4 cycles. The carrier frequency could be left out of the complex summation because only the envelope of the signal is required. If the effective scatterer density is high, then the summation is a random walk in the complex plane and the resulting echo signal amplitude has a Rayleigh distribution (Goodman, 1975). The signal to noise ratio (SNR) of such a signal is characterized by (μ/σ=1.91) (Burckhardt, 1978). As an experiment the SNR was estimated from 1000 pixels simulated with `nscateff=20`. The experiment was repeated 100 times, and the mean SNR was 1.902 (standard deviation 0.037). Example images are shown in Fig. 5.5.

Bibliography

MATLAB: Reference guide. Natick, MA; USA: The Mathworks, 1992.

Benke KK, Skinner DR, Woodruff CJ. Convolution operators as a basis for objective correlates of texture perception. IEEE Trans Syst Man Cybern 1988;18:158–162.

Bishop CM. Neural networks for pattern recognition. Oxford, UK: Clarendon press, 1995.

Botros NM. A pc-based tissue classification system using artificial neural networks. IEEE Trans Instrum Measurement 1992;41:633–638.

Burckhardt CB. Speckle in ultrasound B-mode scans. IEEE Trans Sonics Ultras 1978;25:1–6.

Foley DH. Considerations of sample and feature size. IEEE Trans Inform Theory 1972;18:618–626.

Fu LM. Analysis of the dimensionality of neural networks for pattern recognition. Patt Recog 1990;23:1131–1140.

Fukunaga K. Effect of sample size in classifier design. IEEE Trans PAMI 1989;11:873–885.

Giles CL, Maxwell T. Learning, invariance, and generalization in high-order neural networks. Appl. Opt. 1987;26:4972–4978.

Goodman JW. Statistical properties of laser speckle patterns. Berlin: Springer-Verlag, 1975: 9–75.

Grace A. Optimization toolbox user's guide for use with MATLAB. Natick, MA, USA: The Mathworks, 1992.

Hertz JA, Palmer RG, Krogh AS. Introduction to the theory of neural computation. Reading, Massachusetts: Addison-Wesley, 1991.

Huisman HJ, Thijssen JM. Application of artificial neural networks in ultrasonic tissue characterization. In: Tortoli P and Masotti L, eds. Proceedings of the 22-nd symposium on Acoustical Imaging. 1995: 355–358.

Jain AK, Karu K. Learning texture discrimination masks. IEEE Trans PAMI 1996;18:195–205.

Jakeman E. Speckle statistics with a small number of scatterers. Optical Engineering 1984;23:453–461.

Julesz B, Gilbert EN, Frish HL. Inability of humans to discriminate between visual features that agree in second order statistics – revisited. Perception 1973;2:391–405.

Kittler J. Feature selection and extraction. Chapter 3 in: Young TY and Ku KS, eds. Handbook of pattern recognition and image processing. Orlando, FL, USA: Academic Press, 1986: 59–83.

Lee YC, Doolen G, Chen HH, et al. Machine learning using a higher order correlation network. Physica D 1986;22:276–306.

Lu SW, Xu H. Textured image segmentation using autoregressive model and artificial neural network. Patt. Recog. 1995;28:1807–1817.

McLachlan GJ. Discriminant analysis and statistical pattern recognition. New York: John Wiley & Sons, Inc., 1992.

Nørgaard M. Neural network based system identification toolbox. Institute of automation. Technical University of Denmark, 95-E-7731995.

Ohanian PP, Dubes RC. Performance evaluation for four classes of textural features. Pattern Recognition 1992;25:819–833.

Oosterveld BJ, Thijssen JM, Hartman PC, Romijn RL, Rosenbusch GJE. Ultrasound attenuation and texture analysis of diffuse liver disease: methods and preliminary results. Physics Med Biol 1991;36:1039–1064.

Oosterveld BJ, Thijssen JM, Hartman PC, Rosenbusch GJE. Detection of diffuse liver disease by quantitative echography: dependence on a priori choice of parameters. Ultrasound Med Biol 1993;19:21–25.

Oosterveld BJ, Thijssen JM, Verhoef WA. Texture of B-mode echograms: 3D simulations and experiments of the effect of diffraction and scatterer density. Ultrason Imag 1985;7:142–160.

Papoulis A. Probability, random variables, and stochastic processes. Singapore: McGraw-Hill, 1991.

Raudys SJ, Jain AK. Small sample size effects in statistical pattern recognition: recommendations for practitioners. IEEE Trans PAMI 1991;13:252–264.

Schmidt WAC, Davis JP. Pattern recognition properties of various feature spaces for higher order neural networks. IEEE Trans PAMI 1993;15:795–801.

Stathaki T. Segmentation of textured surfaces using mixed order statistics and neural network classifiers. Electr. Lett. 1995;31:1990–1991.

Thijssen JM. Echographic image processing. Advances in Electronics and Electron Physics 1992;84:317–349.

Thijssen JM, Oosterveld BJ, Hartman PC, Rosenbusch GJE. Correlation between acoustic and texture parameters from rf and B-mode liver echograms. Ultrasound Med Biol 1993;19:13–20.

Unser M. Local linear transforms for texture measurements. Signal Processing 1986;11:61–79.

Verhoeven JTM, Thijssen JM. Improvement of lesion detection by echographic image processing: signal-to-noise-ratio imaging. Ultrason Imag 1991;13:238–251.

Zatari D, Botros N, Dunn F. *In-vivo* liver differentiation by ultrasound using artificial neural network. J Acoust Soc Am 1994;96:376–381.

Chapter 6

Conclusions

The main goal of the work described in this thesis was the research for and the development of methods that could assist in the analysis of ultrasonic images and of images of metastases in the liver in particular. To that end, a large amount of clinical data has been analyzed and methods developed with an emphasis on the option of operating under *in vivo* conditions. The main conclusion of medical interest is that the results indicate that the detection of metastases can be improved.

Throughout the research it also became clear that there are several factors affecting the performance of the analysis methods. As a consequence it was not possible to show how the (quantitative) follow-up of metastases might be improved, although some novel ideas have emerged that are worthwhile to investigate further.

This chapter summarizes the foundations of the previous arguments. The conclusions given in the previous chapters are rearranged and categorized according to the signal processing path also used in the Introduction of this thesis. To begin with, conclusions about the ultrasonic tissue model are presented. Next, conclusions on the scanner model, acquisition, and calibration are joined into one section. The section on feature extraction discusses the discriminability, accuracy, and precision of several features investigated in this thesis. The final section shows how artificial neural networks may or may not contribute to the analysis of ultrasonic images.

6.1 Tissue model

During the evaluation of the acquired images containing liver metastases, it became evident that a single-tissue metastasis model is not realistic, because, for example, ultrasonic appearance varied with the type of primary tumor. Therefore several metastases categories were recognized, and the main subdivision was that based on the primary tumor. The study in chapter 3 was limited to metastases from primary adenocarcinoma in the colon, and even though the analysis was restricted to a single primary tumor type, various subtypes of metastases (hyper-, iso-, hypo-echoic, and heterogeneous [halo+core]) were classified. These observations can be explained by the growth stage of a metastases and/or the effect of (chemo-)therapy. The results from chapter

3 show that acknowledging a multi-category metastases model is beneficial to the development of UTC-methods.

An interesting sub-category of metastases in chapter 3 is formed by the group of homogeneous hypo-echoic metastasis and the hypo-echoic halo tissue surrounding a core in heteregenous metastases. The tissue in this group showed an increased echogenicity with increasing ultrasonic frequency. This was shown to be true relative to the surrounding parenchyma tissue, which led to an interesting observation: at higher frequencies the contrast of the parenchyma to such a metastasis decreases, and the halo and/or the hypo-echoic lesion becomes more difficult to detect. This frequency dependence was also shown to be a phenomenon on an absolute scale (i.e. relative to a set of normal livers) and therefore it reflects real changes in tissue histology compared to normal tissue parenchyma. The conclusion is that by studying the frequency dependence of the echogenicity or by selecting the proper transducer frequency the detectability of some metastases can be improved.

The echogenicity of a metastasis is an established discriminative feature of its B-mode images appearance and is assumed to reflect changes in underlying tissue histology. Unexpectedly, the hypo-metastases in the material studied in chapter 3 appeared to be hypo-echoic only relative to the surrounding parenchyma. When this feature was plotted relative to average normal liver parenchyma values, these metastases appeared to be iso-echoic. Therfore, they were only visible because of an increased echogenicity of the surrounding parenchyma. The data in this study was too limited to firmly conclude that hypo-echoic metastases appear only in hyper-echoic parenchyma. However, if this observation can be reconfirmed then it would implicate that the hypo-echoic nature of a metastasis is not an indicator of metastasis histology. In any case, it would be beneficial to analyze the surrounding parenchyma as well.

To detect metastases, features estimated in metastases should be different from that in the surrounding parenchyma. The parenchyma is usually modeled as a homogeneous medium, and fluctuations in image grey level are due only to speckle noise. During the research it became evident that this model does not adequately describe *in vivo* liver. The results in chapter 2 indicate that two types of inhomogeneity can be recognized due to fluctuations (or inhomogeneity) of the underlying histology: local (within an organ), and global (between organs, or inter-subject). Local inhomogeneity was shown to be the major factor in the increase of the standard deviation on the estimates of four acousto-spectrographic features. The increase due to global variations was much smaller.

In chapter 4 another extension of the homogeneous model was formulated, by introducing inhomogeneous parenchyma background (IPB). The phenomenon IPB is described as a noise component with a small amplitude, but with a large correlation cell size, and it appeared to be a characteristic of liver parenchyma. Given the IPB correlation cell size (4cm^2) the phenomenon should occur on a larger scale than the hepatocyt (20-30μm), or the lobules (1mm). An appropriate scale is the segmental anatomy on the basis of the Couinaud nomenclature, where the branches of the portal vein lead to the center of individual segments. It is hypothesized that IPB may be due to normal, small variations in the vasculature on the (sub)segmental scale.

6.2 Scanner model, acquisition, and calibration

The inhomogeneity of the tissue model affects the discriminability of the UTC features. It is, therefore, important that the preprocessing steps before the actual feature extraction do not introduce additional variability. First of all, it is essential to be able to acquire the ultrasonic signals from standard clinical ultrasonic scanners as accurately as possible. The acquisition workstation used in this thesis received RF signals directly from a custom-built interface in the scanner. This avoided intermediate signal processing elements in the scanner, and also operator-dependent settings (e.g. overall gain, TGC) in the signal.

Part of the work in this thesis was concerned with the accurate estimation of parenchymal properties. Robust estimation of these features requires a strategy to account for *in vivo* measurement conditions, such as small blood-vessels in the estimation window. A mask matrix was used to store manually- and automatically detected areas such as blood-vessels, ligaments, and over- and underflow of the digitizer. A considerable amount of effort has been put into optimizing the segmentation of parenchyma-only area. It can be concluded that the effect of non-parenchymal regions upon the estimated features of liver parenchyma is minimal.

An intermediate step in the feature extraction methods is the calculation of the spectrogram from the RF signal. These calculations require that parameters such as the length, degree of overlap, and type of windowing function be chosen in advance. It was shown in chapter 2 that the sensitivity of extracted features to a variations in (a wide range of) these parameter settings was very low.

The transducer characteristics (TC), as discussed in the introduction, affect the received spectrum. To prevent the TC from interfering with feature estimates, a correction has to be performed. Commonly, in UTC research, TC is estimated using a tissue-mimicking phantom. However, the effect of TC on estimated features in *in vivo* data was not fully removed when using the corrections from the TM-phantom. The effect of TC on *in vivo* liver data was small only when the TC was estimated from average normal *in vivo* liver acquisitions and a method to do so was described in chapter 2. It is concluded that the estimated TC calibration varies with the type of medium. The use of TM-phantoms in the design of UTC methods is even more limited, because, as discussed, in chapter 4, the (TM) phantoms showed only a very small amount of IPB. TM-phantoms also lack the inter- and -intra variability, and thus it can be concluded that the use of presently available TM-phantoms in the development and validation of UTC methods should be construed with caution.

Another intermediate step is the calculation of the logarithm of the average spectrogram. This simple step can affect the variability of the estimates, as the resulting standard deviation (sd) depends on the order of the calculations. The log of the mean amplitude as shown in chapter 2 results in larger sd's than the mean of the log amplitude.

6.3 Feature extraction

Several feature extraction methods have been used throughout this thesis, the properties of these features in normal *in vivo* parenchyma have been analyzed, as well as their discriminative power for metastases. In chapter 2 equations predicting the sd of four *in vivo* measured acousto-spectrographic features were derived, which had not been described in literature. Experiments using simulated images showed that these equations predicted the sd of the features very well over large depth- and frequency- ranges. Extension of the equations with two inhomogeneity terms enabled prediction of *in vivo* sd's. The two terms are an indication of the inter- and intra-organ variability discussed previously in the model section in this chapter. The ultrasonic model extended with IPB improved the prediction of the precision of the acousto-spectrographic features even further. In chapter 4, the IPB phenomenon was shown to be capable of explaining the remarkably large standard deviation of the features attenuation and backscatter intercept at central frequency with respect to the theoretical estimates of the homogeneous model.

The backscatter coefficient quantifies the echogenicity and its frequency dependence. In chapter 3 it was estimated relative to surrounding tissue and relative to average normal liver tissue. The latter allows comparison between patients or different session of the same patient, but unfortunately the precision of the absolute estimate was too low for these features to be useful. The increased variability could have been caused by a number of phenomena: patient condition, examination procedure, skin thickness or phase aberration in the abdominal wall. It is not certain to what extend each item contributes to the decrease in discriminability. To be applicable, further research will have to pinpoint the relevant items and subsequently find variability reduction strategies.

In chapter 4 it was shown that the ultrasonic model extended with IPB was able to accurately predict the dependence of the feature SNR on the window size using the extended ultrasonic model. It is concluded that in *in vivo* images of liver parenchyma the expected value of the feature SNR depends in a predictable manner on the window size, because of the presence of IPB. As a result, the estimates of the feature SNR in differently sized windows (e.g. in metastases in the liver parenchyma) can not be compared, which confirms observations in chapter 3. For fixed window sizes, the feature SNR was shown to have no discriminative power in case of analysis of metastases.

The small number of metastases in which attenuation could be reliably estimated is an indication that the attenuation will be a feature of limited use for *in vivo* analysis of metastases. Moreover, the attenuation features were not different from values found in normal parenchyma. The amount of data is perhaps not sufficient to prove that there is no attenuation difference at all. However, it can be assumed that the difference is small relative to the magnitude of the standard deviation, and as a result, from this study it has to be concluded that the *in vivo* attenuation features cannot discriminate metastases from parenchyma. Attenuation remains an interesting feature, though, for analysis of large tissue areas, such as in the case of diffuse liver diseases.

An additional feature that might be of interest to the follow-up of metastases was mentioned in chapter 3. An automatic halo segmentation method was developed to segment the heterogeneous category of metastases into a core and a surrounding halo. It is commonly assumed that an increase of the halo area is indication of disease progression. The result of the automatic halo segmentation method might be used to quantify this growth factor.

6.4 Artificial neural networks

An additional topic of research has been the use of artificial neural networks (ANN) for the analysis of ultrasonic images.

Throughout this research attempts were made to use ANNs to the classification stage, and it became clear that the application of ANNs did not prove to be advantageous. Earlier claims in UTC literature of successful results appeared to be unrealistic, because some did not prevent the peaking phenomenon (e.g. (Goldberg et al., 1992) trained as well as tested the ANN on the same, small data set). As a result the ANN showed better performance than 'conventional' classifiers. However, when proper performance estimation was carried out, then the results were less favorable, e.g. (Silverman and Noetzel, 1990). Others claimed that ANNs were only better than the linear discriminant analysis methods (Ostrem et al., 1991). However, linear discriminant methods are the simplest classifiers available in statistical literature. Recently, thorough comparisons of various well-known classical pattern recognition methods and ANNs were published and the results confirm the previous observations. ANNs are in general not much better than statistical techniques (Ripley, 1993; Schmidt et al., 1994). It is even possible to translate many neural network models into common statistical models (Sarle, 1994). A thorough comparison of ANN performance to established pattern recognition techniques has been recognized as a difficult problem by the neural networks research field (Prechtelt, 1996). ANNs can be used as an additional type of classifier, but until good guidelines become available for selecting and using an ANN in a limited data set environment, it is concluded that the application of ANNs to the analysis stage is not advantageous.

The application of ANNs to large data volumes and with ability to learn non-linear relations is an area of interest. In UTC this situation occurs when (local) features are extracted in the generation of new feature images. In chapter 5 an adaptive texture feature extraction (ATFE) method was developed using an artificial neural network (ANN-ATFE). The ANN-ATFE was shown to be capable of extracting a minimal set of nearly optimal features.

It was confirmed in chapter 5 that the ANN-ATFE is capable of extracting non-linear features. The method was tested on an example requiring non-linear features to discriminate two tissues. Obviously, 'conventional' analysis was shown to require an extension with non-linear feature extractors. The ANN-ATFE still produced only two features but leveled the performance of the extended feature set.

The developed ANN-ATFE method in chapter 5 extends existing strategies by using reduced invariant higher order functions (IHOF). The IHOF selection allows the user to incorporate prior knowledge: an advantage over the often criticized 'black-box' approach of neural networks. The IHOF reduction reduces the neural network size to allow the ANN-ATFE to be used on realistic data sizes. The chosen IHOF reduction optimization method as well as the neural network training method ensure robust operation.

6.5 Evaluation and future research

The general objective of this thesis has been the application of UTC techniques to *in vivo* analysis of liver metastases. Features were found that differentiate normal from metastases tissue. As a result it is speculated that feature imaging methods could be devised that enhance tumor detection. Application of these features to ‘focal’ analysis is expected not to be succesfull. First, the features need to be estimated on an absolute scale to enable comparison with previous sessions and, unfortunately the precision of the absolute estimates is very low. Second, the follow-up of metastases is often not possible because it is difficult to find the same metastasis in subsequent acquisition sessions.

A interesting feature might be the estimation of the halo volume, by using the halo detection method described in chapter 3. The (relative) amount of halo tissue is well-known to be an indicator of tumor growth status. A robust assessment of the halo volume will improve the follow-up diagnosis of metastases. The detection of the halo volume can even be improved by using the different frequency dependence of the backscatter of the halo and its surrounding tissue. Further improvements may be obtained by using a protocol that acquires multiple, parallel slices.

Another interesting feature results when applying the ANN-ATFE to ultrasound images. A possible training set of images has already been constructed during this research. Actual application to these images can be a future research project, whereby the various invariant higher order functions (IHOF) need to be evaluated, as well as the size of the neural network. A first application can be the use of ANN-ATFE in feature imaging where the backscatter coefficient vs. frequency is used as IHOF. The conventional (B-mode), hypo-echoic metastases contrast can then be compared with the contrast in the feature images.

Another strategy to improve the design of utc-methods, and the analysis stage in particular, is to obtain more training data. This may be difficult to achieve in a single hospital environment. Therefore, it is important to setup multi-center studies. The collective database of acquired data can then be used to train and test the analysis stage, but also to better quantify the discriminative power of several features. Multi-center studies require that measurements can be compared between different ultrasonic scanners, which can only be achieved with good calibration techniques. The *in vivo* normal liver calibration technique described in this thesis results in accurate measurements and should be preferred over synthetic phantom calibration techniques. The extension of this technique to different scanners will need some further research. It is anticipated that multiple ’normal’ groups could be used, but the actual differences need to be quantified.

Finally, another recently emerging technology is the use of ultrasound contrast agents that enhance the amount of backscattering from blood. The increased amount of vascularization in some tumor regions will result in an increasing backscatter level after contrast injection. The onset and rate of increase of contrast, and the final amount of contrast increase are methods already in use for CT and MRI for assessing tumor regions. These methods can easily be applied to ultrasound. An additional advantage could be that the frequency dependence of backscatter will again be of use, as most definitely the frequency dependence of the contrast agent is different from any tissue.

Bibliography

Goldberg V, Manduca A, Ewert DL, Gisvold JJ, Greenleaf JF. Improvements in specificity of ultrasonography for diagnosis of breast tumors by means of artificial intelligence. Med.Phys. 1992;9.

Ostrem JS, Valdes AD, Edmonds PD. Application of neural nets to ultrasound tissue characterization. Ultrason Imag 1991;13:298–299.

Prechtelt L. A quantitative study of experimental evaluations of neural network learning algorithms: current research practice. Neural Networks 1996;9:457–462.

Ripley BD. Statistical aspects of neural networks. In: Barndorff-Nielsen OE, Jensen JL, and Kendall WS, eds. Networks and chaos: statistical and probabilistic aspects. London: Chapman & Hall, 1993: 40–123.

Sarle WS. Neural networks and statistical models. In: Proceedings of the 19th Annual SAS users group international conference. 1994: 1538–1550.

Schmidt WF, Levelt DF, Duin RPW. A experimental comparison of neural classifiers with ’traditional’ classifiers. In: Pattern recognition in Practice IV. 1994: 391–402.

Silverman RH, Noetzel AS. Image processing and pattern recognition in ultrasonograms by backpropagation. Neural Networks 1990;3:593–603.

Summary

Ultrasonic imaging is a commonly used, powerful diagnostic technique in medicine. Since the introduction of the concept of gray-scale ultrasonic imaging in the early 70's, the number of applications has increased and the image quality is still being improved. More recently, ultrasonic tissue characterization (UTC) strategies are developed to quantify existing ultrasonic information or to visualize new information in additional images. The quantification of existing visual information may help physicians to enhance the robustness and reproducibility of their assessments.

Continuing fundamental research in medical ultrasound has led to an increased understanding of the physical mechanisms that govern the image formation process. The resulting theoretical insights may enhance the amount of information that can be retrieved from ultrasonic images. Recent techniques in signal processing, image processing, and pattern recognition facilitate the extraction and quantification of this information. More specific, artificial neural networks have shown promising results in related problems. Finally, actual application of these techniques seems realistic as contemporary computer speed and- memory has reached a sufficient level.

Some of these techniques showed promising results in the analysis of diffuse liver disease. An essential problem of metastases is that they are relatively small, therefore the UTC feature estimation window size has to be small, and consequently the precision will be relatively low. Furthermore, to be applicable in a clinical setting, the UTC methods obviously have to operate under *in vivo* conditions. Therefore, the general problem is to find accurate, precise and discriminative feature estimation methods that can operate under *in vivo* conditions.

Chapter 2 is concerned with the accuracy and precision of UTC features in normal liver parenchyma with the aim of establishing normal ranges of feature values. Theoretical estimates of the standard deviation (sd) of four acousto-spectrographic features (the intercept and slope of attenuation and backscatter coefficient) are derived. The derivation expands and corrects existing derivations, and is confirmed using simulations based on the adopted theoretical ultrasonic image model. A robust feature estimation method is applied to various phantom measurements, and to *in vivo* liver scans of healthy human subjects. The measured sd is higher than the theoretically predicted value and four possible factors are investigated that may explain this discrepancy. First, it is shown that the sd and bias are rather insensitive to changes in spectrogram calculation parameters: windowing function, type, length, and overlap. Secondly, it is observed that the estimation of the transducer characteristics (TC) on a phantom medium did not remove the depth-dependencies on features estimated in the liver and results in a decrease of both precision as well as accuracy. It is concluded that the TC depends not only on the transducer, but also on the medium. A method is proposed that estimates the TC from the averaged spectrogram of a set

of normal livers. This TC is show not to affect the sd even on previously unseen acquisitions. Finaly, two inhomogeneities are introduced. Local inhomogeneity predicts excess sd due to local variations of the physical parameters within an organ (i.e. intra-subject). Global inhomogeneity predicts variations between organs (i.e. inter-subject). In *in vivo* measurements it was shown that the local inhomogeneity is the main factor in the increase of the sd of the features.

In **chapter 3** the performance of five features for ultrasonic tissue characterization (UTC) of metastases in *in vivo* liver was investigated. Serial radio-frequency acquisitions were obtained from 12 patients with metastases of adenocarcinoma in the colon. Parenchyma and metastases UTC features were estimated in semi-automatically segmented regions. Over 200 metastases were measured in patients and 43 "dummy" metastases in healthy volunteers. Two attenuation features could be estimated in only 15% of the metastases, and were not different from that in the parenchyma. The texture feature signal-to-noise ratio (SNR) could not discriminate real from dummy metastases. Average backscatter intensity is an established discriminative ultrasonic image feature. However, the metastases that were hypo-echoic relative to surrounding parenchyma appeared to be iso-echoic relative to normal liver parenchyma. They were visible because of an increased backscatter in the surrounding liver parenchyma. Finally, an increased backscatter coefficient slope vs. frequency was found in hypo-echoic metastases which may predict a deterioration of lesion contrast at higher transducer frequencies. It is concluded that the difference in backscatter coefficient slope can be used to improve detection of metastases. The backscatter intensity, when measured relative to normal liver parenchyma, correctly correlates metastasis ultrasound with histology.

The sd of the intercept features in chapter 2 was unexpectedly high and in chapter 3 the feature SNR (signal-to-noise ratio) was shown to have a significant bias related to the window size. In **chapter 4**, the model is extended with the notion of inhomogeneous parenchyma background (IPB). IPB is shown to be present in normal liver parenchyma and is statistically described by a noise term with small amplitude and large correlation cell size. A method is presented to estimate the IPB characteristics. The expressions predicting sd are extended, and an expression is derived predicting the window size bias of the feature SNR. The results demonstrate good agreement between the estimated and predicted, sd and bias in *in vivo* data. It is concluded that IPB is a realistic and relevant phenomenon and should be part of the *in vivo* ultrasonic model of liver parenchyma.

Computer texture analysis methods use texture features that are traditionally chosen from a large set of fixed features known in literature. These fixed features are often not specifically designed to the problem at hand, and as a result they may have low discriminative power, and/or they may be correlated. Increasing the number of selected fixed features is statistically not a good solution in limited data environments such as medical imaging. For that reason an adaptive texture feature extraction method (ATFE) is developed in **chapter 5** which extracts a small number of features that are tuned to the problem at hand. The use of a feed-forward neural network ensures that even non-linear relations are captured from the data. The performance of ATFE feature set was compared with that of the optimal feature set using extensive, repeated synthetic ultrasonic images. The ATFE method is shown to be capable of robust operation on small data sets with a performance close to that of the optimal feature set. Another experiment confirms that the ATFE is capable of capturing non-linear relations from the dataset. It was concluded that ATFE has potential to improve performance in practical, limited dataset situations where an optimal fixed feature set can be hard to find.

Samenvatting

Echografie wordt in de geneeskunde veelvuldig toegepast bij het stellen van een diagnose. Sinds de introductie van de grijswaarde echografie in de jaren '70 is het aantal toepassingen toegenomen, en is de beeldkwaliteit verbeterd. Een meer recente ontwikkeling is de ultrageluid weefsel typering (Ultrasonic Tissue Characterization, UTC), die de informatie zichtbaar in een beeld kan quantificeren, of die nieuwe informatie, eerst niet of niet zo duidelijk zichtbaar, kan helpen visualiseren. De quantificatie van visuele informatie kan artsen helpen bij het verbeteren van de robuustheid en reproduceerbaarheid van hun beoordelingen.

De voortgaande ontwikkelingen in het fundamentele onderzoek van medische echografie hebben geleid tot nieuwe inzichten in de fysische mechanismen die aan het beeldvormende proces ten grondslag liggen. De resulterende theoretische inzichten kunnen leiden tot een toename van de hoeveelheid informatie die uit een echogram gehaald kan worden. Recente ontwikkelingen in de signaalbewerking, beeldbewerking en patroonherkenning bieden de mogelijkheid om deze informatie uit het beeld te halen en te quantificeren. Een specifieke ontwikkeling daarin zijn de kunstmatige neurale netwerken, die veelbelovende resultaten hebben laten zien in overeenkomstige problemen. De toepassing van deze technieken is nu ook realistisch door de toegenomen snelheid en geheugencapaciteit van computers.

Een aantal van deze technieken heeft al geleid tot veelbelovende resultaten bij de analyse van diffuse leverziekten. Een essentieel, technisch probleem bij het analyseren van metastasen is de kleine oppervlakte, waardoor het weefseloppervlak waarin de UTC kenmerken geschat worden ook klein zal zijn, wat weer een relatief, lage precisie tot gevolg heeft. Daar komt nog bij dat, wil een UTC methode toegepast worden in de kliniek, dan moet deze kunnen werken onder *in vivo* condities. Het algemene probleem dat ten grondslag ligt aan het werk in dit proefschrift is het zoeken naar nauwkeurige, precieze UTC kenmerken die onderscheid maken tussen metastasen en omliggend leverweefsel en die daarbij kunnen ook nog werken onder *in vivo* condities.

Hoofdstuk 2 behandeld de nauwkeurigheid en precisie van UTC kenmerken in normaal leverparenchym met als doel het vaststellen van de normaalwaarden van de kenmerken. Theoretische schattingen worden afgeleid van de standaard deviatie (sd) van vier zogenaamde acousto-spectrografische kenmerken (het snijpunt en de helling van de gelineariseerde verzwakkings- en backscattercurve). Deze afleiding is een uitbreiding en een correctie van bestaande afleidingen, en wordt bevestigd door gebruik te maken van gesimuleerde ultrageluidsbeelden volgens het gebruikte ultrageluidsmodel. Een robuuste kenmerk schattingsmethode wordt toegepast op verscheidene fantoom metingen, en *in vivo* leveropnames van gezonde proefpersonen. De gemeten sd is groter dan de theoretisch voorspelde waarde en vier factoren worden onderzocht die mogelijk dit verschil kunnen verklaren. Ten eerste wordt aangetoond dat de sd en bias ongevoelig zijn voor de instelling van de spectrogram berekening parameters: vensterlengte, -type, en overlap. Ten tweede is vastgesteld dat het schatten van de transducer karakteristieken (TC) met een weefsel fantoom niet of niet voldoende de diepteafhankelijkheid corrigeert van de kenmerken geschat in de lever, wat resulteert in een lagere precisie als ook nauwkeurigheid. De conclusie is dat de TC niet alleen van de transducent maar ook van het weefsel afhangt. Een nieuwe methode is ontwikkeld die de TC schat uit het gemiddelde spectrogram van een set normale levers. Van deze TC kan worden aangetoond dat deze de sd niet aantoonbaar verhoogt. Ten slotte worden twee inhomogeneiteitsfactoren geintroduceerd. de locale inhomogeneiteit voospelt de toename van de sd a.g.v. variaties van de fysieke parameters binnen de lever (intra-subject). De globale inhomogeneiteit voorspelt de variaties tussen organen (inter-subject). Uit de resultaten blijkt dat de locale inhomogeneiteit het meest bijdraagt in de toename van de sd van de UTC kenmerken.

In **hoofdstuk 3** wordt onderzocht hoe goed vijf UTC kenmerken presteren in de analyse van metastasen in *in vivo* lever opnames. Opeenvolgende radiofrequente opnames zijn gemaakt van 12 patiënten met metastasen van een primair adenocarcinoma in het colon. Parenchyma en metastasen UTC kenmerken werden geschat in semi-automatische gesegmenteerde gebieden. Meer dan 200 metastasen werden gemeten bij de patiënten en 43 “nep” metastasen bij de 2 gezonde proefpersonen. Twee verwakkingskenmerken konden worden geschat in maar 15% van de metastasen, en daarbij waren deze niet verschillend van de kenmerken gemeten in het parenchym. Het textuur kenmerk SNR was niet in staat om echte van nep metastasen te onderscheiden. De gemiddelde backscatterintensiteit is een bekend, discriminerend kenmerk. Het bleek echter dat metastasen die hypo-echoisch zijn t.o.v. omliggend weefsel, ten opzichte van normaal leverweefsel iso-echoisch kunnen zijn. Deze metastasen zijn zichtbaar door de toegenomen intensiteit van het omliggende leverweefsel. Tenslotte is ook vastgesteld dat de helling van de frequentie afhankelijke backscattercurve in hypo-echoische metastases is toegenomen, wat een verslechtering van het contrast zou betekenen bij hogere transducer frequenties. De conclusie is dat deze backscatterhelling de detectie van metastasen zou kunnen verbeteren Een tweede conclusie is dat de bacskcatterintensiteit moet worden gemeten relatief ten opzichte van normaal leverweefsel om op een correcte wijze de correlatie met de histologie te kunnen vinden.

De sd van de snijpunt kenmerken in hoofdstuk 2 was onverwacht hoog en in hoofdstuk 3 was ook al aangetoond dat het kenmerk SNR een significante bias had in relatie met de venstergrootte In **hoofdstuk 4** wordt daarom het weefsel model uitgebreid met het begrip inhomogene parenchyma achtergrond (IPB). Het verschijnsel IPB blijkt aanwezig te zijn in normaal parenchym en kan statistisch worden beschreven als een ruis term met kleine amplitude, maar met een breed correlatie gebied. Een methode is ontwikkeld om de karakteristieken van IPB te schatten. De uitdrukkingen die de sd voorspellen worden uitgebreid, en een uitdrukking wordt afgeleid die de bias van de SNR in relatie tot de vensterafmetingen voorspeld. De resultaten laten een goede overeenkomst zien tussen de geschatte en voorspelde sd en bias in *in vivo* opnames. De conclusie is dan ook dat IPB een realistisch en relevant fenomeen is dat onderdeel zou moeten zijn van een *in vivo* ultrageluidsmodel van leverparenchym.

Computer textuuranalysemethoden maken gebruik van textuurkenmerken die traditioneel gekozen worden uit een grote set vaste kenmerken bekend uit de literatuur. Deze vaste kenmerken zijn meestal niet specifiek ontworpen voor het onderliggende probleem, met als gevolg dat ze niet zo discriminatief zijn en/of gecorreleerd kunnen zijn. Om dat te compenseren zou het nodig zijn om meer kenmerken te nemen, maar dat is statistisch gezien geen goede oplossing in situaties waarin de hoeveelheid leervoorbeelden vaak beperkt is, zoals vaak het geval is bij medische ultrageluidsbeelden. Om die reden is de mogelijkheid van een adaptief textuurkenmerk (ATFE) onderzocht in **hoofdstuk 5**. Zo'n adaptieve methode moet in staat zijn om een klein aantal kenmerken te genereren die specifiek zijn afgeregeld op het onderliggend probleem. Toespassing van feed-forward neurale netwerken (ANN) zorgt er daarbij voor dat zelfs niet-lineaire verbanden uit de gegevens kunnen worden meegenomen. De prestaties van deze neurale ATFE (ANN-ATFE) zijn vergeleken met de optimale kenmerken in een synthetische data set. Van de ontwikkelde ANN-ATFE methode wordt aangetoond dat deze in staat is om robuust te werken op kleine gegevens sets met een prestatie die dichtbij de optimale kenmerken ligt. In een ander experiment wordt aangetoond dat de ANN-ATFE in staat is om niet-lineaire functies te leren in een geschikte dataset. De conclusie is dat de ATFE methode de prestatie kan verbeteren in situaties waarbij de hoeveelheid leervoorbeelden beperkt is en waar de optimale kenmerken niet direct voorhanden zijn.

Glossary

Item list of abbreviations and explanations:

ANN	artificial neural network
ANN-ATFE	artificial neural network based adaptive texture feature extractor
ATFE	adaptive texture feature extractor
$\langle snr \rangle$	average SNR
IHOF	invariant higher-order function
IPB	inhomogeneous parenchyma background
ROI	region of interest
SBDM	small bloodvessel detection method
SNR	signal-to-noise ratio (mean over standard deviation)
TM	tissue mimicking
TGC	time gain control
TC	transducer characteristic
UTC	ultrasonic tissue characterization

Item list of mathematical symbols and explanations.

t	time
f	temporal frequency
z	depth
σ_v	predicted standard deviation of the stochastic variable v
s_v	estimated standard deviation of the stochastic variable v

μ_v	predicted average value of the stochastic variable v
$\overline{v}$	estimated average value of the stochastic variable v
$\mathcal{F}$	Fourier transform
Pr	Probability
θ	transducer angle
$N(.,.)$	normal distribution
$e(t)$	received echo signal at time t
$E(f,z)$	the received amplitude at temporal frequency f of the backscattered echoes of a small tissue volume at depth z
$P(f)$	the acousto-electrical transfer function
$D(f,z)$	the diffraction spectrogram of the transducer
$T(f,z)$	the tissue transfer function (attenuation)
a_0	intercept at central frequency of the attenuation coefficient
a_1	slope of the attenuation coefficient
$a(f)$	frequency dependent attenuation coefficient
$S(f)$	the backscatter function
b_0	intercept at central frequency of the backscatter intercept
b_1	slope of the backscatter coefficient
$b(f)$	frequency dependent backscatter coefficient
ξ	inhomogeneity factor
F	focus
s_l	lateral speckle size
s_k	axial speckle size
$r()$	correlation coefficient
α	IPB factor

Dankwoord

Bij het samenstellen van dit proefschrift is het eind in zicht van een periode van ploeteren, zweten, stressen, en stug doorgaan. Een klus die je duidelijk nooit in je eentje kunt klaren. Op dit moment borrelt dan ook een niet aflatende stroom goede herinneringen op aan collega's, vrienden en iedereen die je tijdens zo'n promotie een duwtje meegaven en/of je er ook aan hielpen herinneren dat er meer is dan alleen de promotie.
Bedankt:

- Han Thijssen, voor je niet aflatende bron van motivatie, stimulatie, relevante artikelen, waar haal je het vandaan?
- Professor Oosterom, voor de strenge, maar opbouwende kritiek op de manuscripten;
- Marijke Eijkemans, en al je collega's die elke keer weer gemotiveerd mee hielpen met het opnemen van gegevens met de computer, ook als het allemaal niet zo soepel verliep;
- Gert-Jan Spaargaren voor je geweldige inzet bij de speurtocht naar patiëntengegevens in duistere archieven en natuurlijk je Coq-au-Vin;
- Arthur "Perry" Berkhoff, voor het mij "besmetten" met het LaTeX en Matlab virus;
- Eric Jacobs, zonder jou programmeerinzichten zouden mijn computerprogramma's nooit goed gewerkt hebben;
- Robert Homan, als onontbeerlijke steun en toeverlaat in Unix zaken;
- Albert van Geemen en Frank Valckx, voor het samen "bakken" van fantomen;
- Rien Cuypers voor het willen aanhoren van mijn geklaag;
- Max, Patrick en Ordwin voor de vlijtige "kunstmatig neurale" inzet gedurende jullie afstudeer periodes.
- Marnix, Alexander en Raymond voor het bouwen van een werkelijk onmisbaar programma op dat onmogelijk OS9 systeem!
- Hans Verhoeven voor het bijbrengen van het paranimfengevoel, en hoe voelt dat nu?

- Frits van de Wateren (Chess Engineering) voor het in de lucht houden van de computer;
- Ton van der Steen voor je verfrissende kijk op ultrageluid;
- Guus Carbaat voor het meten van mijn depressie;
- Theo van Lith voor nakijken van de manuscripten en dat je me af en toe laat winnen bij het poolen;
- Carlo, Carola, Ellen, Natalie, en Noor voor het “beschikbaar” stellen van je lever.

Een lijst is natuurlijk nooit uitputtend en het mag duidelijk zijn dat alle bijdragen aan dit proefschrift zeer op prijs zijn gesteld. Natuurlijk wil ik hierbij ook familie en vrienden bedanken voor jullie indirecte steun en warme meelevende gevoelens. Zonder jullie prettige vertragingstactieken zou het een stuk minder goed uit te houden zijn geweest. Heel erg bedankt.

Curriculum vitae

In dutch

De auteur van dit proefschrift werd geboren op 10 augustus 1966 in Rotterdam. Midden in een huis vol techniek was het doel al gauw duidelijk, alleen de “eigenwijze” omgeving moest daarvan nog wel overtuigd worden. Geheel tegen de zin van de onderwijzer van klas 6 lagere school werd in 6 jaar het VWO doorlopen aan het Comenius College in Capelle a/d IJssel. Gedurende deze periode van 1978 tot 1984 werd, alweer op tegenadvies, maar nu van de natuurkunde leraar, een B-pakket gekozen dat toelating tot de TU Delft Elektrotechniek mogelijk maakte. Ook dit werd niet gebruikelijk geacht daar de auteur zich al te veel met electronica bezig hield. Dat laatste heeft dan ook niet lang mogen duren: na 6 jaar was het knutselen opgehouden, maar de studie voltooid.
Gedurende de afstudeerperiode bloeide de voorliefde op voor het werken met beelden. Vanzelfsprekend ga je dan afstuderen bij vakgroep Informatietheorie met als specialisatie beeldbewerking. Een eerste kennismaking met de medische beelden werd gelegd tijdens een stage bij dr.ir. Reiber van het LKEB toen nog in de Erasmus Universiteit in Rotterdam. De afstudeerperiode bij het KSEPL in Rijswijk leerde dat er nog meer dan alleen medische beelden waren, maar dat heeft uiteindelijk niet mogen helpen . . . .
Het jaar 1991 was onvergetelijk groen en vol ’leerzame’ ervaringen op kazernes in Nederland en Duitsland en tegelijkertijd de basis voor een heftige drang naar meer intellectuele uitdagingen. Zo’n uitdaging was rap gevonden in Nijmegen. Van 1 februari 1992 tot 1 februari 1997 was de auteur aangesteld als AIO bij: eerst het Biofysich Laboratorium op de afdeling Oogheelkunde, en vervolgens bij het Klinisch Fysich Laboratorium op de afdeling kindergeneeskunde. Tussendoor is 1 jaar gewerkt aan het Europees project CLAQUE.
Vanaf 1 juni werkt de auteur bij de afdeling Radiologie van het Radboudziekenhuis Nijmegen.

In english

The author was born in Rotterdam, The Netherlands on August 10, 1966. He received the MSEE degree in 1990 from the Delft University of Technology, The Netherlands. After 1 year of compulsory military service he started the Ph.D. study that led to this thesis at the University of Nijmegen, The Netherlands. During this period he cooperated in a European Comittee Project: Claque, Clinical and Quantitative Assessment of Echograohic images. Currently he is employed at the Radiology Department of the Academic Hospital Nijmegen on a project concerning the post processing of dynamic MRI images. His research interests are: medical imaging, artificial neural networks, statistical pattern recognition. He is member of the IEEE, and the Dutch Society for Pattern Recognition and Image Processing.